Universidade de Aveiro Departamento de Engenharia Cerâmica e do Vidro
2007

Luís Miguel de Almeida Amaral

Estudos de Sinterização de Cerâmicos de Titanato de Estrôncio Não Estequiométrico

Sintering Studies of Nonstoichiometric Strontium Titanate Ceramics

Universidade de Aveiro Department of Ceramic and Glass Engineering
2007

Luís Miguel de Almeida Amaral

Sintering Studies of Nonstoichiometric Strontium Titanate Ceramics

A dissertation presented to the University of Aveiro in fulfilment of the requirements for the awarding of the Masters in Materials Science and Engineering carried out under the supervision of Professor Paula M. L. S. Vilarinho, Associate Professor of the Department of Ceramics and Glass Engineering of the University of Aveiro, and Professor Ana M. O. R. Senos, Auxiliar Professor of the Department of Ceramics and Glass Engineering of the University of Aveiro.

Financial Support from POCTI under the 3rd Framework programme.

The Board of Examiners

president

Prof. Dr. Joaquim Manuel Vieira
Full professor from the University of Aveiro

Prof. Dr. Ian Michael Reaney
Full professor from the University of Sheffield, U. K.

Prof. Dr. Ana Maria de Oliveira e Rocha Senos
Auxiliar professor from the University of Aveiro

Prof. Dr. Paula Maria Lousada Silveirinha Vilarinho
Associate professor from the University of Aveiro

Acknowledgements

I want to express my deep gratitude to my supervisors, Paula Vilarinho and Ana Senos, for the opportunity for doing this research and for their priceless guidance and valuable discussions along this work. I am also very grateful to Alexander Tkach for his help and guidance in several of the tasks performed during this study.

Many thanks to all my colleagues in the department for the nice work atmosphere they proportionated and the enjoyable coffee breaks we had. I am also grateful to all the technicians of the department for all the generous help they gave me.

I am thankful to FCT (Portuguese Foundation for Science and Technology) for financial support.

Finally, I want to thank my family for the support I always received from them. I will always be grateful to the owner of my heart, Ana Ferreira, for her endless patience and support along these last months, and for being with me even when I was not there.

keywords strontium titanate, ceramics, non stoichiometry, sintering, grain growth

summary

Strontium titanate (ST) is a very interesting material for applications in microelectronics, namely tunable microwave devices, due to its tunable dielectric response and low microwave losses. The electrical properties required for this kind of applications are strongly dependent on the characteristics of the grain boundaries and directly influenced by the grain size and grain size distribution. The doping effect on the electrical properties of ST is reasonably known, but the influence of lattice defects, such as Sr/Ti ratio or oxygen deficiency, on the sintering and grain growth kinetics and the relation with the electrical properties is poorly understood. In this study, the effect of nonstoichiometry (Sr/Ti from 0.997 to 1.02) on the densification and grain growth of ST ceramics was systematically addressed. Compositions with Sr/Ti ratios from 0.997 to 1.02 were prepared. The kinetics of densification was studied by dilatometric analysis. X-ray diffraction (XRD), scanning electron microscopy (SEM) and transmission electron microscopy (TEM) were used for crystallographic and microstructure characterization. The small excess of both TiO_2 and SrO used in the several compositions seems to have been mostly incorporated into the perovskite lattice. XRD revealed no second phases for all compositions before and after sintering and solid solution effects are indicated by a variation of the lattice parameter with the Sr/Ti ratio. SEM observation of sintered samples revealed no second phases and TEM observation is coherent with prevalent solid solution effects for all compositions. Ti excess enhanced the matter transport during sintering whereas Sr excess decreased it. An increase on the shrinkage rate and average grain size was observed with the decrease of the Sr/Ti ratio. Close values of the activation energy ($534 \leq Q_d \leq 663$ kJ/mol) were determined for the initial densification of all the compositions, and the onset of densification was observed to occur at a near constant temperature. Therefore, it is suggested that the same mechanism of transport controls the densification of all the compositions. Taking the grain size distributions of sintered samples, the regimen of grain growth was found to change from abnormal grain growth (AGG) for the Ti-rich and stoichiometric compositions to a normal grain growth (NGG) for the Sr-rich one, with a significantly smaller average grain size. The role of Sr excess on the inhibition of the grain growth was also investigated. Grain growth activation energies and kinetic exponents were calculated for the stoichiometric composition and the Sr rich one. Activation energy values for the grain growth of 365 and 431 kJ/mol and kinetic exponents for the grain growth of 3 and 4 for the stoichiometric and the Sr-rich composition, respectively, were obtained, being in agreement with the inhibition of grain growth observed in the case of Sr rich composition. The results, both of densification and grain growth, suggest that the accommodation of the Ti or Sr excess in the perovskite structure of ST induces alterations in the

defect chemistry of the material and that the mass transport during sintering is controlled by Sr vacancies. A very small stoichiometric variation has a strong influence on the sintering kinetics and resulting microstructure of ST ceramics and, therefore, may be used to engineer the final properties of the material.

palavras-chave ttitanato de estrôncio, cerâmicos, não estequiometria, sinterização, crescimento de grão

resumo

O titanato de estrôncio (ST) é um material com potencial interesse para aplicações em microelectrónica, nomeadamente dispositivos sintonizáveis na gama de frequências das microondas, devido à sua resposta dieléctrica sintonizável e baixas perdas. As propriedades eléctricas requeridas para este tipo de aplicações são fortemente dependentes das características das fronteiras de grão e influenciadas directamente pelo tamanho de gão e pela sua distribuição. O efeito de dopantes nas propriedades eléctricas do ST é razoavelmente conhecido, mas a influência dos defeitos da rede, bem como da relação Sr/Ti ou da deficiência de oxigênio, na cinética de sinterização e na relação com as propriedades eléctricas, ainda não é suficientemente compreendida. Neste estudo, o efeito da não estequiometria (Sr/Ti de 0.997 a 1.02) na densificação e no crescimento de grão de cerâmicos de ST foi abordado sistematicamente. Foram preparadas composições com razões Sr/Ti de 0.997 a 1.02. A cinética de densificação foi estudada através da análise dilatométrica. Difracção de raios-X (DRX) e microscopias electrónicas de varrimento (SEM) e de transmissão (TEM) foram usadas para a caracterização cristalográfica e da microstructura. A incorporação na rede do excesso de TiO_2 ou SrO usado nas várias composições parece ter sido predominante. A DRX não detectou segundas fases em qualquer das composições antes e após a sinterização e a variação do parâmetro de rede com a razão Sr/Ti é indicativa de efeitos de solução sólida. A observação em SEM de amostras sinterizadas também não revelou a presença de segundas fases e a observação em TEM é coerente com efeitos de solução sólida predominante am todas as composições. O excesso de Ti aumentou o transporte de matéria durante a sinterização enquanto o excesso de Sr o diminuiu. Foi observado um aumento da velocidade de retracção e do tamanho médio de grão com a diminuição da razão Sr/Ti. Valores de energia de activação próximos foram determinados ($534 \leq Q_d \leq 663$ kJ/mol) para o estágio inicial, para todas as composições, e o início da densificação ocorreu a uma temperatura relativamente constante. Assim, os resultados sugerem que o mesmo mecanismo de transporte controla a densificação em todas as composições. A partir das distribuições de tamanho de grão de amostras sinterizadas, foi observada uma alteração do regime de crescimento de grão de anormal (AGG), no caso das composições ricas em Ti e da estequiométrica, para crescimento de grão normal (NGG) no caso da composição rica em Sr, com um tamanho médio de grão significativamente mais reduzido. O papel do excesso de Sr na inibição do crescimento de grão também foi investigado. Energias de activação para o crescimento de grão e expoentes cinéticos foram calculados para a composição estequiométrica e para a rica em Sr. Valores de 365 e 431 kJ/mol para as energias de activação do crescimento de grão e expoentes cinéticos 3

e 4, para as composições estequiométrica e rica em Sr, respectivamente, foram obtidos, estando de acordo com a inibição do crescimento de grão observada no caso da composição rica em Sr. Os resultados, relativamente à densificação e ao crescimento de grão, sugerem que a acomodação do excesso de Ti ou Sr na estrutura da perovsquite do ST induz alterações na química de defeitos do material e que o transporte de matéria durante a sinterização é controlado pelas lacunas de Sr. Uma pequena variação estequiométrica influencia significativamente a cinética de sinterização e a microestrutura resultante dos cerâmicos de ST e, portanto, poderá ser usada para desenhar as propriedades finais do material.

Table of Contents

List of figures

List of tables

List of symbols

A - generic acceptor

a - cubic unit cell parameter

A_{sv} – mass specific surface area

B - constant depending on the material and the mechanism

B' - constant depending on the material and the mechanism

C - constant depending on the material and the mechanism

c - heating rate

D - generic donor

D_{SEM} – equivalent diameter measured by SEM

$\overline{D}_{SEM}$ – average equivalent diameter

d - density

d_{air} - density of air

d_{liq} - density of liquid

d_t - theoretical density

E - dc bias electric field

e' - conducting electron

G - average grain size

$G_{0\,BET}$ - average particle size determined by BET

$G_{0\,Laser}$ - average particle size determined by Coulter

$G_{0\,SEM}$ - average particle size determined by SEM

$h^{\bullet}$ - conducting hole

K_0 - pre-exponential constant

l - linear dimension

m - grain size exponent

n - concentration of electrons

P - porosity

p - concentration of holes

pO_2 - oxygen partial pressure

Q - activation energy

Q_d - activation energy for densification

Q_g - activation energy for grain growth

R - gas constant

r_i - average ionic radius

s - kinetic sintering exponent

T - temperature

t - tolerance factor

$tan\delta$ - dielectric loss

V - vacancy

W_1 - weight of sample in air

W_2 - weight of sample in liquid

y - linear shrinkage

ε - dielectric constant

θ - diffraction angle

ρ - relative density

ρ_0 - relative density of the green compacts

σ - electrical conductivity

Σ - sintering stress

$'$ - negative charge

$\bullet$ - positive charge

List of abbreviations

AFM – Atomic Force Microscopy

AGG – Abnormal Grain Growth

BST - Barium Strontium Titanate

BT - Barium Titanate

CHR – Constant Heating Rate

DRAM – Dynamic Random Access Memory

DTA - Differential Thermal Analysis

EELS - Electron Energy-Loss Spectrometry

EDS - Energy Dispersive Spectroscopy

GB – Grain Boundary

GG - Grain Growth

GGIT – Grain Growth Inhibition Threshold

HRTEM - High Resolution Transmission Electron Microscopy

ICP - Inductively Coupled Plasma

MOSFET - Metal Oxide Semiconductor Field Effect Transistor

MW - Microwave

NGG – Normal Grain Growth

PTC - Positive Temperature Coefficient

PTCR - Positive Temperature Coefficient of Resistance

RP - Ruddlesden-Popper

SOFC - Solid Oxide Fuel Cell

ST - Strontium Titanate ($SrTiO_3$)

ST 0.997 - $Sr_{0.997}TiO_{2.997}$

ST 0.999 - $Sr_{0.999}TiO_{2.999}$

ST 1.02 - $Sr_{1.02}TiO_{3.02}$

SEM - Scanning Electron Microscopy

TEM - Transmission Electron Microscopy

TG - Themogravimetry

XRD - X-ray diffractometry

Introduction

Strontium titanate ($SrTiO_3$), hereafter designated ST, is a very interesting material from the scientific and technological point of view. ST and ST-based materials have a wide range of applications, namely in tunable microwave (MW) devices, and are still revealing new properties, as will be seen in section 1.1 of this text.

Previous results [1] obtained in this research group showed that small variations of the stoichiometry of ST induce a strong variation on the obtained grain size of the ceramics, although the perovskite structure is maintained. TiO_2 excess causes an increase of the grain size, whereas in the case of SrO excess, grain growth (GG) is reduced and a small grain size is obtained. Because microstructure variations have a strong influence on the electrical response of materials, it is of crucial importance to comprehend this effect. Moreover, the understanding of these phenomena may allow customizing the electrical properties of the material by tailoring the microstructure. This work reports a systematic study conducted on the sintering behavior of stoichiometric and nonstoichiometric ST.

The accommodation of excess oxide, either TiO_2 or SrO, in nonstoichiometric compositions, induces variations on the defect chemistry of the resulting material. Defect chemistry of titanates, namely barium titanate, $BaTiO_3$ (BT), one of the most important and studied ferroelectric materials, and ST is presented in section 1.3. Most of the studies of defect chemistry were performed through conductivity measurements under several temperatures and oxygen partial pressure (pO_2) conditions. The defect chemistry models derived from these studies contribute to the understanding of the mass transport during sintering and the properties of the materials. Besides the studies on the defect chemistry, also sintering studies on these materials available on the literature are presented (section 1.4).

BT and ST are similar materials from the structural point of view both crystallizing with the perovskite type structure (section 1.2). However, in terms of electrical properties, BT and ST show different behavior. ST is an incipient ferroelectric or a quantum paraelectric [2] whereas BT is a ferroelectric with a phase transition, from the paraelectric state (cubic) to the

ferroelectric (tetragonal) state, at 120 ºC [3]. Due to this property and related applications, BT is considered the prototype of ferroelectric materials and one of the most studied materials; a large amount of papers concerning BT is available in the literature. In some way, the knowledge about BT can be very useful in the analysis and understanding of ST. Several studies on defect chemistry and sintering behavior of BT are presented in this thesis and called to the discussion whenever appropriate and convenient. On the other hand, the differences between the two systems are also highlighted.

The results obtained in the course of this work are presented in section 3 and discussed in section 4. Densification and GG observed in nonstoichiometric ST are correlated with the possible defect chemistry of ST. The main conclusions are drawn in section 5.

1 Overview

1.1 Technological interest of $SrTiO_3$

The titanates, as members of the perovskite family, exhibit very interesting properties for electronic devices as well as for novel applications and have received great attention over the years [2-4]. Their wide range of properties encompasses dielectric, ferroelectric, piezoelectric, pyroelectric, electrooptical and magnetooptical properties and can be tailored with regard to the intended application by compositional, stoichiometric, structural or morphological variation.

ST-based compounds have been attracting a considerable interest from the fundamental point of view for a long time. ST is a quantum paraelectric [2, 5] in which the dielectric permittivity monotonously increases upon cooling down to near 0 K and no ferroelectric-type anomaly is observed. Besides quantum paraelectric behavior, interesting properties of ST include a structural phase transition [6], semiconductivity [7], superconductivity [8], among others.

On the other hand, ST is an important material with a wide range of applications, particularly in electronic devices, due to its relatively high dielectric constant and low loss tangent. ST potential application fields range from high-density dynamic random access memories (DRAM) [9, 10], gate dielectric in MOSFET (metal oxide semiconductor field effect transistor) devices [11], integrated capacitors [10, 12], varistors [13, 14], to sensors [15] or solid oxide fuel cells (SOFC) anodes [16].

In spite of all these applications, owing to the extensive use of microwaves in radar and communication applications, the most important of the current applications for ST-based materials are related to microwave microelectronic elements [17-19]. In addition, the dielectric constant of ST reveals a dependence on applied bias electric field, as can be seen in Figure

1-1, and therefore the dielectric permittivity can be tuned [19-22]. This property is called tunability [20] and is characteristic of ferroelectric materials being strengthened on approaching the paraelectric-ferroelectric phase transition, at which the dielectric constant has a maximum [23]. Tunable microwave devices based on ST are now of particular importance in the microelectronics industry.

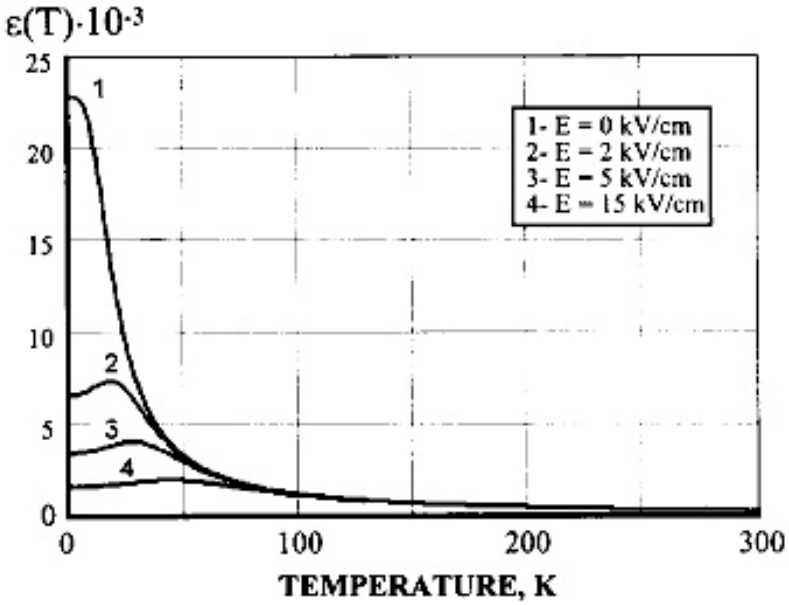

Figure 1-1: Dielectric constant of ST single crystal as a function of temperature and biasing field [19].

Cylinders or cubes of dielectric ST single crystals or ceramics can be used as dielectric resonators or filters [20]. These materials can also be used as parallel plate tunable capacitors or varactors at radio frequencies, as electroded slabs in stack of lens antennas and as small low cost microwave phase shifters for use in phased array antennas [20].

Limiting its practical application is the fact that substantial tunability is achieved in undoped ST only below ~80 K [24]. However, as depicted in Figure 1-2, the temperature range of high tunability and high dielectric constant can be shifted towards room temperature

by formation of solid solutions between incipient ferroelectric ST and classical ferroelectric BT [19, 25]. Such shift corresponds to an induced ferroelectric phase transition in $Ba_xSr_{1-x}TiO_3$ (BST) solid solutions at temperatures in the range of 0-400 K [25].

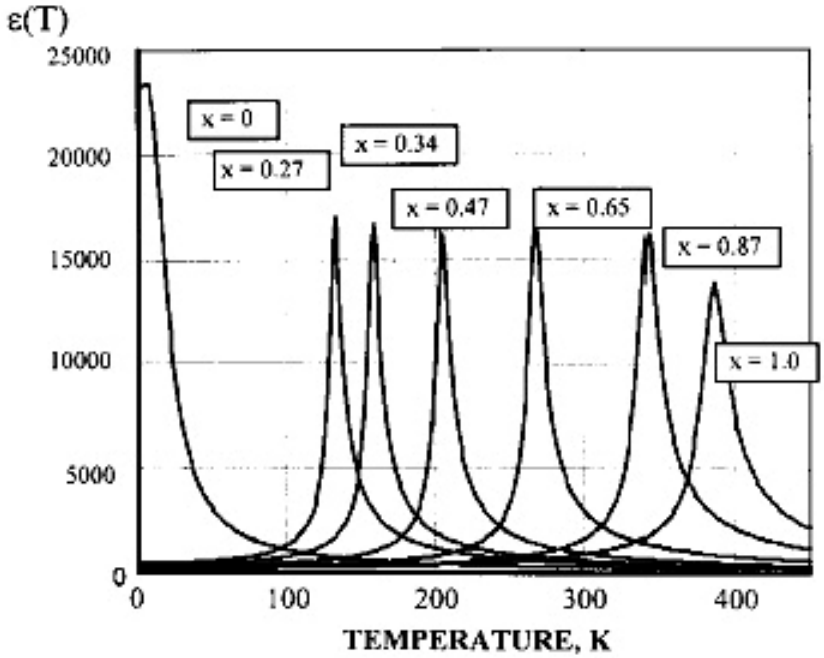

Figure 1-2: Dielectric constant of $(Ba_x,Sr_{1-x})TiO_3$ single crystal as a function of temperature for different content of barium (x) [19].

ST is still revealing interesting properties and novel applications can be envisaged for ST. Recently, blue-light emission at room temperature from Ar^+- irradiated ST was reported [26]. Also, in the last year, Szot et al. [27] reported switching of the electrical resistance of single dislocations within the oxide material ST, as illustrated in Figure 1-3. Their work demonstrates a bistable mechanism at room temperature. The resistive state of dislocations can be determined by application of a low voltage, and thus, very low power and information can be stored by applying a higher voltage that causes a transition from one resistive state to another. A high memory density, thus, appears feasible, with the storage part of the memory

element less than 10 nm in each dimension. This opens new application fields for ST, enabling the development of non-volatile memories for high-storage density applications [28].

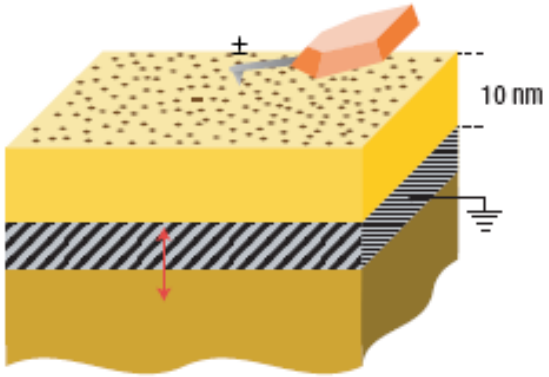

Figure 1-3: Switching of single dislocations. The dislocations (dark spots) are individually addressed by an atomic force microscope with a conductive cantilever [28].

More recently, in the current year, Lee et al. [29] reported the correlation between a grain boundary structural transition and a change in the electrical property, using a ST bicrystalline grain boundary as a model system. The electrical properties of grain boundaries in ST play a critical role in barrier-layer devices, such as capacitors and varistors [29] and so, new developments, leading to better understanding of grain boundary related phenomena, enhanced electrical properties and novel applications, are expected.

1.2 Crystal structure of $SrTiO_3$

1.2.1 The perovskite structure

Perovskite is the name of calcium titanate ($CaTiO_3$) but stands for a whole class of ternary oxides that exhibit the same or a related crystallographic structure. This family of oxides is represented by the general formula ABO_3 and has a cubic structure, where A cations are placed at the cube corners, small B cations are located at the body centre and oxygen ions (O^{2-}) at the center of the faces [30], as schematically shown in Figure 1-4. The structure can also be regarded as a three-dimensional framework of BO_6 octahedra, arranged in a simple cubic pattern. In the octahedron unit, B atom is at the centre with the oxygen atoms at the corners shared by different octahedron and A cations occupying the interstitial positions between the octahedra [30].

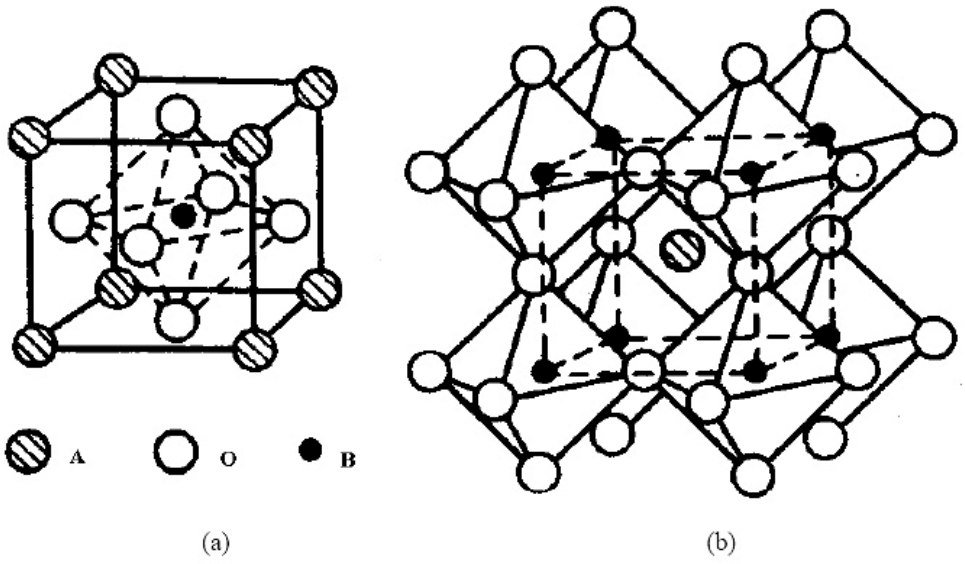

Figure 1-4: Two representations of the ideal cubic perovskite structure: (a) the cubic unit cell and (b) the oxygen octahedra arrangement [30].

A-cations are 12-coordinated and B-cations are 6-coordinated and the ideal perovskite unit cell contains one formula unit, i.e., one A-cation, one B-cation and three oxygen ions.

The perovskite structure is very tolerant to cation substitution in both A and B sites of the lattice, and hence may lead to more complex compounds, for example, quaternary solid solutions like $Ba_{1-x}Sr_xTiO_3$ (BST) [31]. The incorporation of a foreign cation into the perovskite lattice depends on the ionic size and electronic structure of both the foreign ion and the substituted one. This affects the stability of the structure and may cause distortions that modify the cubic elementary cell into tetragonal, rhombohedral or orthorhombic structures. Consequently, the dielectric response of ST may also be affected.

A measure of the perovskite structure stability is the Goldschmidt tolerance factor, t [2, 32], that relates the ionic radii of the constituents of the perovskite lattice, defined by equation (1-1):

$$t = \frac{r_A + r_O}{\sqrt{2}\left(r_B + r_O\right)} \qquad (1\text{-}1)$$

where r_i (i = A, B, O) denotes the average ionic radii of the constituents of the ABO_3 compound in the respective sites.

The tolerance factor is also a measure of the deviation from the ideal packing that the ionic sizes can move maintaining a stable perovskite structure. The value of t is correlated to the structural distortion, force constants of binding, rotation and tilt of the octahedrons, etc. [2]. Several properties, especially related to the dielectric, phase transition behavior etc., are directly correlated with this simple tolerance factor approach. For $t < 1$, the size of the unit cell is governed by the B-site ion and A-site ions are allowed to fluctuate in their sites. For $t > 1$, B-site ions have too much space to vibrate whereas A-site ions are closely packed. For $t = 1$, both A and B ions are closely packed.

1.2.2 The structure of $SrTiO_3$

Strontium titanate is considered an example of the ideal cubic perovskite structure [6]. In ST, A sites are occupied by Sr^{2+} ions and B sites by Ti^{4+} ions. At room temperature, ST has an undistorted cubic perovskite structure of the space group *Pm3m* [33] and its lattice constant is 3.905 Å [2, 34]. The tolerance factor for ST is $t \approx 1$ [32], showing the high (ideal) packing of its structure. This does not allow for interstitial site occupation.

From cubic at room temperature, ST presents a phase transition to tetragonal (space group *I4/mcm* [33]) around 110 K [6, 35]. This phase transition is related with tilting of the oxygen octahedra around one of the [100] axes [36] and the tetragonal phase is centrosymetric. Therefore, no polarization is induced in ST below 110 K and the transition is a non-ferroelectric structural phase transition with almost no influence on the dielectric response [22].

1.3 Defect chemistry of the titanates

Perfect crystals, in which all the identical sites are occupied by identical atoms or ions, does not exist at temperatures above 0 K [37, 38]. Actually, real crystals show lattice defects, deviations from the ideal crystal lattice, which concentration increases with temperature. Defect chemistry is the study of deviations from the perfect order in crystalline inorganic compounds and its effect on their properties [39].

Point defects, those that involve only a single atomic species or lattice site, are very important defects in crystalline solids. Intrinsic point defects are electrons and holes, interstitials (Frenkel disorder) [39], which are less significant here because of the high packing density of the perovskite structure, and vacancies in the Sr-, Ti- and O-sublattices (Schottky disorder) [39], in the case of ST. These defects occur for thermodynamical reasons or due to impurity accommodation. Extrinsic point defects are doping elements. Point defect models describe the correlation between the stoichiometry, the equilibrium concentrations of defects and charge carriers as well as their variation with respect to changes of thermal, chemical or electrical parameters by means of solid state thermodynamics [40].

Defects of higher dimension are also present in materials. These defects are one-dimensional defects like dislocations, two-dimensional defects, for instance, twin boundaries or stacking faults, as in layered structures of the Ruddlesden-Popper (RP) phases [41]. Interfaces, like grain boundaries and surfaces, also need to be considered because they have a significant impact on the characteristics of the material.

Defects affect markedly the final properties of materials, namely mechanical, chemical, thermal and electrical. In particular, the electrical properties of ST and other titanates are closely related to the defect structure of the material. The intrinsic generation of electrons and holes by thermal activation over the bandgap and the extrinsic generation of charge carriers due to compensation reactions for lattice defects (impurities or intentional doping) are very important to understand the electrical behavior and related properties of the material.

In addition, the type of defects present in the material and its concentrations influence the matter transport processes during sintering. Therefore, a strong impact on the resulting microstructure and, as a consequence, on the final properties of the material can be expected.

1.3.1 Background

Due to the practical importance of titanates, the defect chemistry of these materials has been considered in numerous studies since the 1970s. Some of the most relevant aspects of defect models are outlined here.

Long and Blumenthal [42] proposed a defect model for BT that incorporates electrons, holes, singly and doubly ionized oxygen vacancies and foreign acceptors (substitutional metallic species that have a lower ionic charge than the ion which they replace and are compensated by oxygen vacancies [43, 44]). In one of the most extensive works published on this matter, Seuter [37] suggested that singly ionized oxygen vacancies are not important. Seuter's model incorporates electrons, holes, doubly ionized oxygen vacancies and a constant concentration of negative charge originated from either constant difference between the barium and titanium content, from foreign acceptors or from both.

Further developments were done by Chan et al. [43]. Their model, built upon Seuter's model, attributed the constant negative charge to the foreign acceptors only, due to an unavoidable impurity presence in materials. Some degree of defect complex formation (association between the acceptor impurities and oxygen vacancies that held together by electrostatic attraction between oppositely charged defects on adjacent lattice sites) is introduced to account for the decrease in the effective net acceptor content with the decrease of temperature. Moos and Hardtl [45] studying ST, considered a model substance closely related to the industrially used barium or lead titanates, suggested that the acceptor charge is frozen-in metal vacancies and that no acceptor-type impurity level needs to be considered.

All the above mentioned models make use of the Brouwer approximation [46], which consists in considering, for each regime of oxygen partial pressure, only the predominant

defect for positive and negative charge to the charge neutrality equation. This, in combination with the law of mass action [39, 45], allows one to find the concentrations of the various point defects present in the material as a function of pO_2. This is valuable information in order to understand the properties of the material and predict the influence of the material defect state (dependent on the nonstoichiometry, dopants, temperature, pO_2, among other factors) on the mass transport during sintering.

The classical defect notation of Kröger and Vink is used in this text. As an example, $V_O^{\bullet\bullet}$ denotes a double ionized oxygen vacancy. It indicates the individual deviation from the undisturbed ideal crystal lattice, when one oxygen atom is missing. The prevailing defect is assigned by the main index, i.e., the element symbol or '*V*', which represents a vacancy. The subscript refers to the occupied lattice site, which is also marked by the element symbol or by "*i*" for an interstitial site. The superscript indicates the net excess charge of the defect with respect to the initial lattice charge, which is defined as neutral. A point ($^{\bullet}$) accounts for one positive charge and a prime ($^{'}$) for a negative one. A neutral (or isovalent) situation is indicated by an *x* (^{x}). "*nil*" represents the standard state which is taken as the perfect crystal with all electrons in the lowest available energy states. $e^{'}$ and $h^{\bullet}$ represent conducting electrons and holes, respectively.

1.3.2 Undoped and acceptor doped titanates

Most of the studies on defect chemistry of titanates were preformed trough electrical conductivity (σ) measurements under equilibrium conditions, i.e. high temperature and controlled pO_2 [42, 47]. The results from these measurements for both BT and ST, undoped or acceptor doped, are usually characterized by an oxygen deficient, *n* type region, with the conductivity decreasing with the increasing pO_2, and an oxygen excess, *p* type region, with the conductivity increasing with increasing pO_2. These regions are separated by a conductivity minimum, as exemplified in Figure 1-5, for undoped BT.

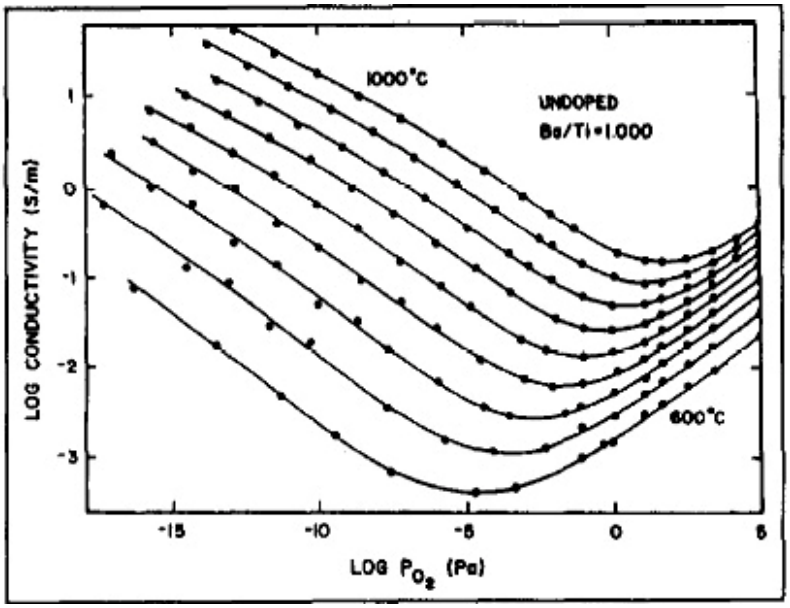

Figure 1-5: The equilibrium electrical conductivity of undoped BT measured at the equilibration temperature as a function of oxygen activity. The temperature ranges from 600 to 1000 ºC at 50 º intervals [48].

The log-log slopes appear to be *+1/4* and *-1/4* above and below the conductivity minima with a transition to *-1/6* at the lowest oxygen activities and highest temperatures [39]. These regions, with different behavior of conductivity with oxygen partial pressure, are explained in the following paragraphs. At the lowest oxygen activities, the slope *-1/6* is consistent with a reduction reaction (equation (1-2)) that produces oxygen vacancies, as expected for a compound that has Schottky disorder as its preferred intrinsic ionic disorder [39, 49, 50], and free electrons that goes into the conduction band [45]:

$$O_O^x \Leftrightarrow \frac{1}{2} O_2 + V_O^{\bullet\bullet} + 2e' \qquad (1\text{-}2)$$

Therefore, in this region, the behavior of σ is dominated by the loss of oxygen and the reduction reaction (1-2) is the major source of defects. Then, the electroneutrality condition can be approximated by equation (1-3):

$$n \approx 2\left[V_O^{\bullet\bullet}\right] \tag{1-3}$$

With the appropriate mass action expression (see [39, 45] for mass action considerations) the proportionality expressed in relation (1-4) is obtained, in agreement with the observed slope.

$$n \propto p\left(O_2\right)^{-\frac{1}{6}} \tag{1-4}$$

Because of the extreme conditions with respect to pO_2 and temperature, this regime is often not measured. The transition to this region regarding the oxygen partial pressure depends on the acceptor impurity concentration, i.e., the intrinsic concentration of oxygen vacancies, as will be explained in the following text, concerning the other mentioned pO_2 regions.

Due to inevitable impurity incorporation during processing, also a nominally undoped material shows a slight doping level. Due to their natural abundance, the elements that are commonly found as impurities in these materials, such as Fe^{3+}, Al^{3+}, Mg^{2+} or Na^{+} [48], show an acceptor-type behavior [39, 42, 43, 48]. The incorporation of a generic acceptor oxide, A_2O_3, and the accompanying formation of extrinsic oxygen vacancies during the preparation of acceptor-doped BT or ST from the binary oxides (as usual by the mixed oxide route) can be described by the following, simplified reaction in equation (1-5) [39]. Here, A_2O_3 virtually replaces $2TiO_2$, with A^{3+} substituting for Ti^{4+}.

$$2SrO + A_2O_3 \rightarrow 2A_{Ti}^{'} + 5O_O^x + V_O^{\bullet\bullet} \tag{1-5}$$

As a direct consequence of this, any undoped or acceptor-doped ST or BT sample exhibits a specific concentration of oxygen vacancies, which is independent of the reduction reaction (equation (1-2)). Only at the lowest oxygen activities, the reduction reaction dominates completely the defect chemistry of these materials. Therefore, in the regions near the conductivity minima, the charge neutrality will be dominated by the oxygen vacancy concentration that is virtually unchanged and fixed by the acceptor concentration according to equation (1-6), which constitutes a valid approximation to the equation of electroneutrality.

$$2\left[V_O^{\bullet\bullet}\right] \approx \left[A_{Ti}^{'}\right] \tag{1-6}$$

As pO_2 increases, these extrinsic oxygen vacancies begin to be filled by the oxidation reaction, according to equation (1-7):

$$\frac{1}{2}O_2 + V_O^{\bullet\bullet} \Leftrightarrow O_O^x + 2h^{\bullet} \tag{1-7}$$

This reaction consumes lattice defects rather than creating them. Combining the mass action expression for the oxidation reaction with the charge neutrality equation, equations (1-8) and (1-9) are obtained. These expressions are in agreement with the observed slopes for the conductivity dependence on oxygen activity, on both sides near the minima.

$$n \propto p\left(O_2\right)^{-\frac{1}{4}} \tag{1-8}$$

and

$$p \propto p\left(O_2\right)^{\frac{1}{4}} \tag{1-9}$$

The oxidation and reduction regimes are separated by a conductivity minimum that corresponds to a *n-p* transition, as depicted in Figure 1-6.

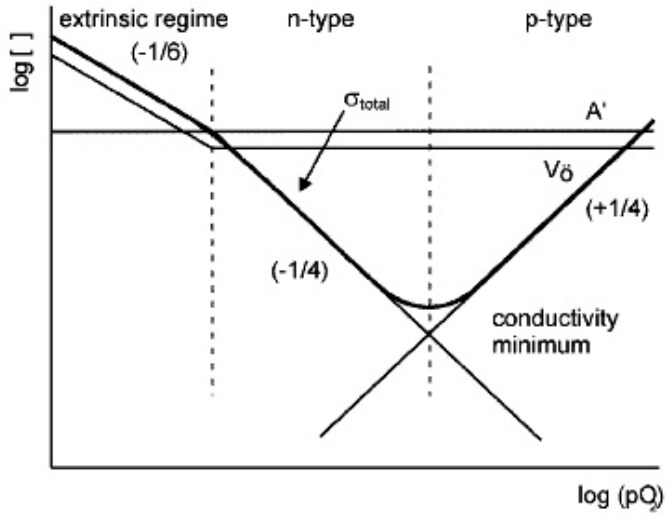

Figure 1-6: Kröger-Vink diagram illustrating the major defect concentrations in undoped and acceptor-doped titanates as a function of oxygen activity under equilibrium conditions. The total conductivity is also drawn [40].

The conductivity minimum corresponds to the perfectly compensated composition, i.e., the oxygen content is chemically equivalent to the total amount of metallic constituents. At this point the only source of electronic carriers is by direct ionization across the band gap [43], according to equation (1-10):

$$nil \Leftrightarrow e' + h^{\bullet} \qquad (1\text{-}10)$$

where "*nil*" represents the perfect crystal with all electrons in the lowest available energy states. Moving to even higher oxygen partial pressures some of the intrinsic oxygen vacancies

can be filled and the oxidation reaction described by equation (1-7) becomes effective. As a result, holes develop into the dominating charge carriers.

When the material is quenched from a high equilibration temperature down to the vicinity of room temperature, holes can be trapped due to a change of the acceptor's valence state [39, 51] given by the following equation:

$$A^x \Leftrightarrow A^{'} + h^{\bullet} \qquad (1\text{-}11)$$

In contrast to the *n*-type behavior, which is maintained by quenching to room temperature resulting in a dark colored conductive material, a *p*-type equivalent does not exist. This hole-trapping is the reason why acceptor-doped materials are light colored insulating and why no semiconducting *p*-type perovskite is known in the literature in contrast to the *n*-type semiconducting donor-doped titanates [40].

The conductivity characteristics shown in Figure 1-5 can be described satisfactorily by the model of point defect chemistry that is schematically illustrated in Figure 1-6. The model assumes that acceptor impurities are always present. Only in the most reducing conditions, the reduction reaction is the major source of defects. The acceptor centers and the corresponding compensating oxygen vacancies dominate the defect chemistry over most of the experimental range.

As the behavior of undoped BT or ST indicates that acceptor impurities are already present, the increasing acceptor content only means an extension of that behavior. An increase in the acceptor concentration shifts the curve towards lower pO_2 values, because of the shifted intercept of $\left[A^{'}\right]$ and $\left[V_O^{\bullet\bullet}\right]$. Independently of the acceptor concentration, all curves converge to the same values at very low pO_2, where the oxygen deficiency exceeds the acceptor content and the approximated charge neutrality becomes the equation (1-3) [44].

1.3.3 Donor doped titanates

The situation becomes considerably different when the material is doped by a donor-type element. This is, in fact, one of the least understood aspects of the defect chemistry of the titanates [39].

A donor dopant has a higher oxidation state than that of the host cation it replaces in the solid compound [52]. The impurity center thus bears an effective positive charge relative to the ideal lattice of the host oxide and requires charge compensation by a species having an effective negative charge, e.g., a cation vacancy, an anion interstitial, an acceptor impurity, or an electron. Typical donor impurities in BT or ST include large cations with charge >2+ substituted for the alkaline earth ion, e.g. La^{3+}, and small cations with charge >4+ substituted for Ti, e.g. Nb^{5+} or W^{6+}. Thus the impurity oxide has more oxygen per cation than the host oxide it replaces, Nb_2O_5 vs TiO_2 or La_2O_3 vs BaO or SrO, and the effect of donor impurities then depends on the loss or the retention of this extra oxygen [52].

Donors have very shallow energy levels (and so, low ionization energies) and are therefore fully ionized down to temperatures of several K [15, 40, 45], according to equation (1-12).

$$D \rightarrow D^{\bullet} + e' \qquad (1\text{-}12)$$

where D stands for a generic donor. Donor-doped titanates may exhibit semiconducting properties with a high conductivity even at room temperature, which is the case when the donors are compensated by electrons. However, the compensation mechanisms in the donor doped titanates are complex [39]. For very low levels of donor doping, the oxygen excess in the donor oxide is lost, even when the material is equilibrated in an oxidizing atmosphere, and compensation is indeed by electrons, according to equation (1-13):

$$La_2O_3 \rightarrow 2La_{Ba}^{\bullet} + 2O_O^x + \frac{1}{2}O_2 + 2e' \qquad (1\text{-}13)$$

The result is a dark colored conducting material. As the donor concentration increases, the excess oxygen is retained and the compensation appears to be primarily by cation vacancies, which are, in the case of BT, Ti vacancies [39, 45, 53], as shown in equation (1-14), in spite of the high relative charge of these vacancies.

$$2Nb_2O_5 + 5BaO \rightarrow 4Nb_{Ti}^{\bullet} + 5Ba_{Ba}^{x} + V_{Ti}^{''''} + 15O_O^x \qquad (1\text{-}14)$$

This results in a light colored insulating material. So, as the donor concentration increases, there is an abrupt transition from conducting to insulating material, and, at the same time, a significant change in the microstructure, with the grain size being similar to that of undoped BT in the first case and much smaller in the second one [39]. The relation between these two facts is not well understood and will be later revisited.

In ST, the cation vacancy compensation was found to occur by strontium vacancies [45, 49, 50, 54, 55]. An excess Sr (equal to the compensating strontium vacancy concentration) is fixed by the donor content and may remain in the crystal forming layered Ruddlesden-Popper structures [56], acting as a sink or source for the strontium or, depending on the point of view, its vacancies [45]. The computer simulations of Akhtar et al. [50] are in agreement with this belief, in spite of the lack of experimental evidence [49]. The last investigation reported the migration of excess Sr to the surface, under oxidizing conditions, where secondary SrO_x phases grew on top of the surface [49], leaving behind vacant Sr sites, according to equation (1-15):

$$Sr_{Sr} + 2e' + \frac{1}{2}O_2 \Leftrightarrow V_{Sr}'' + SrO_{\mathrm{sec}-phase} \qquad (1\text{-}15)$$

However, the process of formation of cation vacancies is not yet well understood [45].

Figure 1-7 shows a schematic Kröger-Vink diagram illustrating the defect model for donor-doped titanates and the several regions in it will be explained in the following text.

In region I, under highly reducing conditions, the defect chemistry is governed by the reduction reaction of equation (1-2), and, as in the case of acceptor doping, equation (1-3) is valid. The oxygen vacancies are the predominant ionic defects and electrons are the charge compensating species. The dependence of the electron concentration n shows again the characteristic slope of *-1/6*.

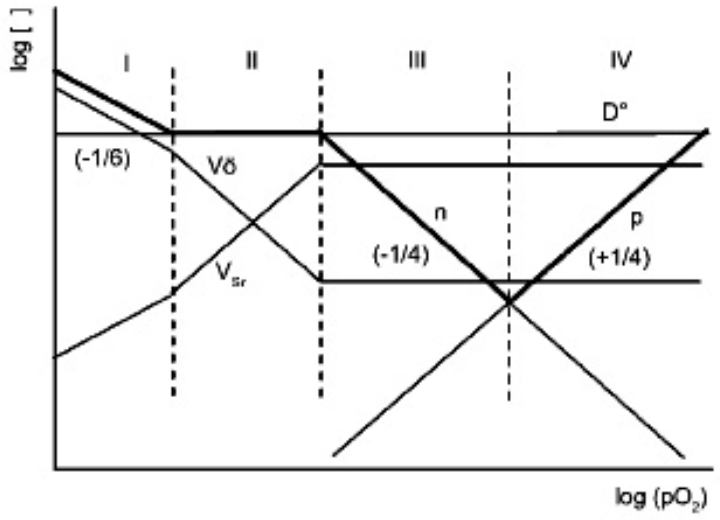

Figure 1-7: Kröger-Vink diagram illustrating the major defect concentrations in donor doped titanates as a function of oxygen activity under equilibrium conditions [40].

In the subsequent regime II, at intermediate pO_2 values, the oxygen vacancy concentration becomes small relatively to the extrinsic donor concentration $\left[D^{\bullet}\right]$. The compensation of the donors by electrons is dominant and the condition of electroneutrality can be approximated by equation (1-16):

$$n \approx \left[D^{\bullet}\right] \qquad (1\text{-}16)$$

The concentration of electrons, and thus the dominant n-type conductivity, does not change with the oxygen partial pressure. Because σ has the appearance of a plateau, this regime is also called the "plateau region" or region of electronic compensation. Moreover, a relative independence of the temperature is verified for the conductivity in this regime [52] indicating that the electron concentration is fixed by the donor concentration and that there is little temperature dependence of the electron mobility.

By a further increase of the pO_2 to oxidizing conditions (region III), the compensation for the donor impurities is attributed to a mechanism of acceptor-like strontium vacancy compensation (as mentioned above) and the approximate electroneutrality condition becomes equation (1-17):

$$2\left[V_{Sr}^{''}\right] \approx \left[D^{\bullet}\right] \qquad (1\text{-}17)$$

Combined with the appropriate mass action expressions, this condition leads to a $\sigma \propto p(O_2)^{-\frac{1}{4}}$ behavior. The conduction behavior for donor-doped titanates also shows the characteristic slope of *+1/4* in the region denoted IV in Figure 1-7. However, the plateau region shifts the *±1/4* slope regimes towards higher oxygen partial pressures so that the increasing p-type conductivity is usually not visible [40].

The conductivity characteristics for ST and BT doped with varying amounts of donors are shown in Figures 1-8 and 1-9, respectively. As can be seen, the donor-doped samples clearly show the plateau region with insignificant pO_2 dependence of σ. With increasing donor concentration, the plateau region becomes more and more pronounced. This is accompanied by an increased conductivity, as derived from equation (1-16).

The point defect model describes adequately the conduction properties of the materials as proved by the good agreement between the experimental data shown in Figures 1-5, 1-8 and 1-9 and the slopes and transitions between regimes predicted by the briefly exposed models.

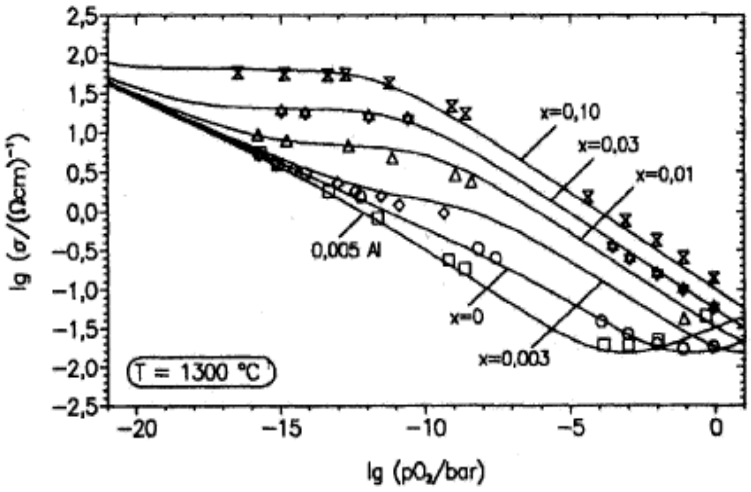

Figure 1-8: Equilibrium electrical conductivity of lanthanum donor doped (various concentrations), undoped and aluminum acceptor doped ST ceramics at 1300 ºC [45].

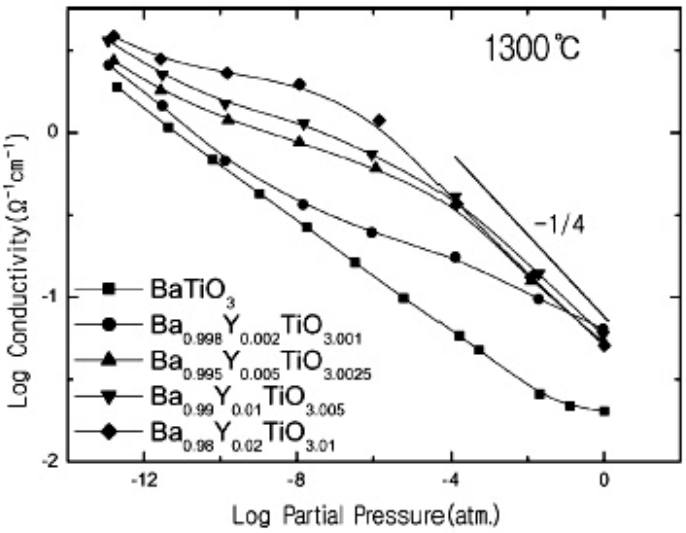

Figure 1-9: Equilibrium electrical conductivity of $(Ba_{1-x}Y_x)TiO_{3+0.5x}$ (x = 0, 0.002, 0.005, 0.01 and 0.02). In this case, Y^{3+} substitutes for Ba^{2+} and acts as a donor [57].

1.3.4 Grain boundaries

Point defects models discussed above assume that the material is an homogeneous and isotropic system with a diluted concentration of defects [40]. However, grain boundaries are present in polycrystalline ceramics and affect remarkably the overall electrical behavior of the material. In fact, some electrical properties required for particular applications, such as boundary layer capacitors, low-voltage varistors, or positive temperature coefficient (PTC) thermistors depend on the characteristics of the grain boundaries rather than on the properties of the bulk grains [58-60].

Figure 1-10 displays the different pathways for charge transport in a heterogeneous material. It can be seen that a quite complex situation arises, involving bulk pathways and transport across boundaries as well as along boundaries. The behavior of the material, therefore, turns out to depend significantly on the properties of the grain boundaries that are markedly affected by its defect chemistry. Hence, grain boundaries are of high importance. In the particular case of ST and BT perovskite compounds, the response of devices such as barrier layer capacitors and PTC thermistors is a consequence of highly engineered grain boundary electrical barriers [61]. In these cases, grain boundaries are often electronically active due to depletion effects and exhibit a highly resistive behavior [61-63] acting as barriers to the transport of charge carriers.

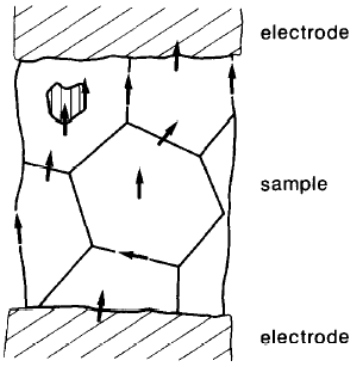

Figure 1-10: Schematic representation of perpendicular and parallel pathways for charge carriers in a heterogeneous material in contact with electrodes [64].

The basis for the formation of a charged surface or grain boundary in ionic solids is a difference in the individual defect formation energies [61]. This leads to a preferential enrichment of the interface in the ion of lower vacancy formation energy and the formation of an adjacent space charge enriched in that vacancy. When extrinsic solutes raise defect concentrations above thermally generated concentrations they determine the sign of the grain boundary and the space charge [61].

This grain boundary barrier effect is well known, for example, for n-type semiconducting ceramics, being responsible for the varistor effect in donor doped ZnO ceramics as well as for the positive temperature coefficient of resistance (PTCR) effect in donor doped BT ceramics ([65] and references therein). In these cases, a negatively charged grain boundary is compensated by the positively charged donor centers in the bulk adjacent to the grain boundaries forming a depletion space charge layer necessary for electroneutrality. From an electronic point of view, grain boundaries can be described as back-to-back double Schottky barriers [15, 62, 65, 66].

For undoped and acceptor-doped alkaline earth titanates, positively charged grain boundary interface states seem to be active even at sintering temperatures [61]. A space charge layer model was developed for grain boundaries in acceptor-doped titanate ceramics [61, 62, 65, 67]. Due to the existence of positively charged grain boundary states, the regions close to the grain boundaries are depleted of mobile charge carriers with the same charge sign as the grain boundary states (oxygen vacancies and holes are repelled from the vicinity of the grain boundary). At the same time, electrons are accumulated because the positive grain boundary charge has to be compensated by a negative space charge on both sides of the grain boundary built up by the immobile bulk acceptors.

This redistribution of charges leads to the formation of the space charge layer, as shown in Figure 1-11. The grain boundary resistivity can be explained by the fact that the major charge carriers have to overcome this positively charged barrier. The width of the grain boundary depletion layer in acceptor-doped ST has been determined to be 30-200 nm, decreasing with increasing acceptor concentration ([62] and references therein).

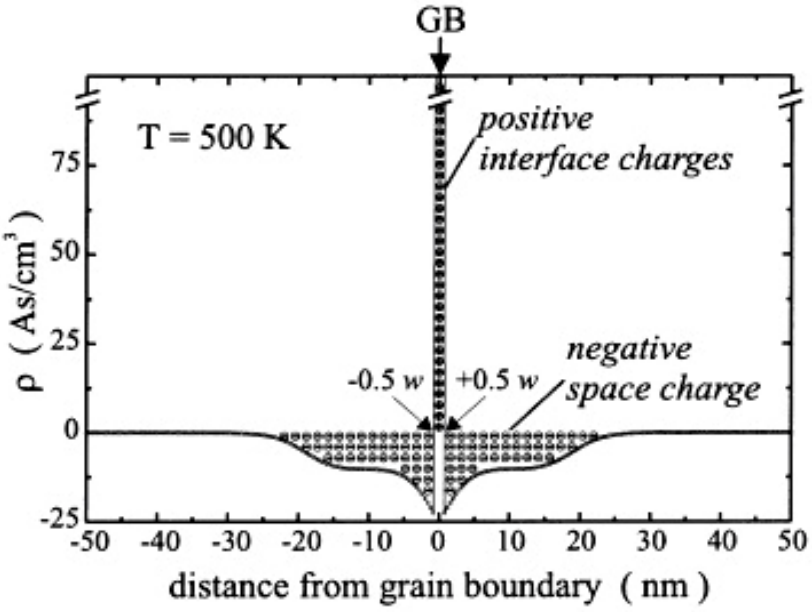

Figure 1-11: Simulated spatial profile of the space charge density ρ(x) along an axis perpendicular to the grain boundary for 0.2 at.% Ni-doped ST at a temperature T = 500 K [62].

Theoretical models concerning the spatial distribution of point defect concentrations and partial conductivities near interfaces or grain boundaries in ionic crystals were developed by Maier [68]. The electrically active interface states or defects and the depletion of identically charged defects lead to an enhancement of oppositely charged species. In the grain boundary region, depending on the concentrations of the donor-type charges, this phenomenon may lead to an inversion of the original conductivity type observed in the bulk material. The partial conductivities of the charge carriers dominating the bulk behavior are reduced by many orders of magnitude and may be exceeded by the increased contribution of electrons, originating an inversion of the conductivity in the grain boundary region (Figure 1-12).

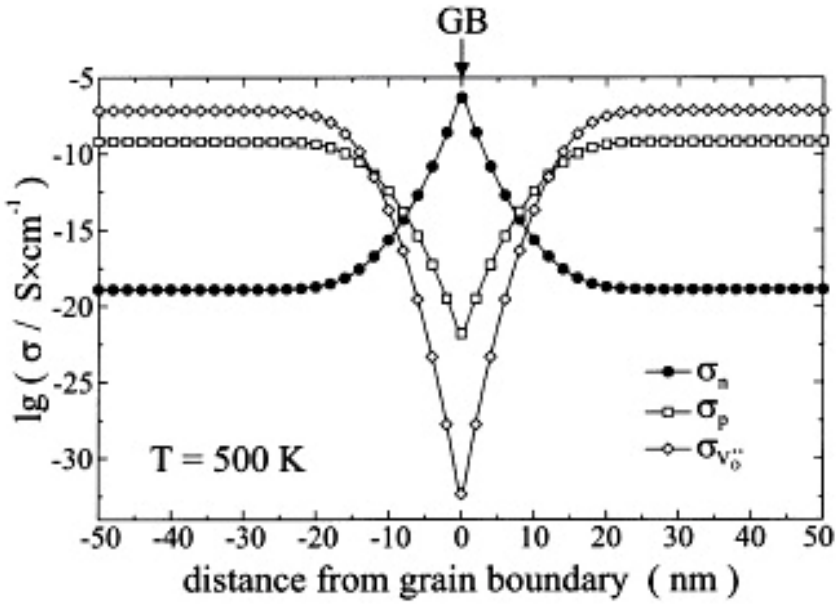

Figure 1-12: Simulation of the partial conductivities for 0.2 at.% acceptor-(Ni-)doped ST at a temperature T = 500 K. The total conductivity is the sum of the three partial conductivities (being equal to the partial conductivity of the oxygen vacancies in the bulk and to the partial conductivity of the electrons in the core of the GB originating a "W" shaped conductivity profile) [62].

The structural accommodation between two grains occurs approximately over only a few nanometers [60]. The investigations of the grain boundary region in BT and ST by Chiang and Takagi revealed a strong segregation of acceptor impurities to the grain boundary [61, 67]. In contrast, a segregation of donors was not observed. However, another investigation revealed a slight donor segregation [60] at the grain boundaries in polycrystalline ST. Chiang and Takagi also found a concentration of Ti in excess in the grain boundaries, which amounted to 20 - 80% of a monolayer and no systematic variation in the excess of Ti with the overall composition, including A site / B site cation stoichiometry [61].

Other investigations confirm the presence of Ti-rich layers at grain boundaries [69-71]. Oxygen deficiency at the interface due to unoccupied lattice sites and oxygen vacancy segregation to the boundary were also reported by the authors. These vacancies, which are

assumed to be immobile and unable to diffuse due to a lack of space, are compensated by electrons resulting from the lowering of the Ti valence, which form a n-type layer at the interface [70]. This is in good agreement with the theoretical models [71] showing that oxygen deficient structures are energetically favorable.

1.3.5 Surfaces

As the grain boundaries, surfaces are a very important factor influencing the electrical behavior of the material. The surface and the region below, sometimes called “surface layer”, strongly influence the macroscopic properties of titanates. Usually, the surface region exhibits drastically different behavior compared to the bulk of the crystal [72, 73]. However, neither the character of this region nor its dimension are well understood.

A good knowledge of the electrical behavior of the surface region and the characteristics of the surface is essential since measurements of the conductivity are the basis of defect chemistry, as seen above. For this, a detailed analysis of the properties of the surface is necessary. In addition, phenomena related with the surface region are of special relevance for technological applications in which thin layers, such as thin films of ST, are used as dielectrics in microelectronic devices [72]. For reduced thickness, the influence of the surface may become very important. For these reasons, the surface characteristics of titanates, specially ST [72, 74], have received attention in the last few years. It was found that the surface region of titanates can be restructured by exposing the sample to extreme atmospheric conditions, elevated temperatures and prolonged annealing times [72-75].

X-ray diffraction (XRD) measurements [73] showed that reactions take place in the solid phase in the surface layer of BT, ST, $PbTiO_3$ and $KNbO_3$ perovskite crystals at elevated temperatures (500 - 1000 ºC), associated with segregation in the direction to the surface of AO complexes. This leads to the formation of a whole homologous series of crystalline compounds with the general formula $AO.(ABO_3)_n$. According to the authors, a low oxygen partial pressure may inhibit the segregation processes and, in the range of temperatures for

which vaporization of the AO complexes from the surface does not yet take place, a suitable choice of oxygen pressure may lead to resynthesis of the compound [73].

Microanalysis in combination with XRD has revealed that the near-surface region of ST extending several tens of nm into the bulk of the material develops chemical inhomogeneities after standard thermal treatment for reducing as well as oxidizing conditions [76]. The authors observed for the oxidized crystals a SrO-rich RP phase on and near the surface, whereas TiO_2 and Magnelli-type (Ti_mO_{2m-1} (with m = (1,. . .,38)) [77] Ti-rich phases formed in deeper layers of the surface region. For the reduced crystals, the authors reported an inversion of the enrichment and depletion leading to Ti-rich phases on and near the surface and SrO-rich RP phase in the deeper layers of the surface region. Additional loss of oxygen from the Ti-rich phases close to the surface caused a successive reduction of the Ti-rich phases.

Szot et al. [72] observed a dramatic restructuring for both reducing and oxidizing conditions leading to the formation of non-perovskite phases on the surface, after extensive thermal treatment for temperatures in the range of 800 - 1000 °C. For oxidized crystals with (100) orientation, this caused the formation of a regular SrO-rich surface with the RP phase Sr_2TiO_4 above 900 °C. The formation of regular terraces with a step height of ≈ 11.8 Å was observed by the authors. For the reduced state, the restructuring of the surface region leads to the formation of a Ti-rich phase of type TiO and Ti_2O on the surface above 900 °C depending on the reduction level. In fact, the surface undergoes a continuous change in time, which leads in the case of oxidizing conditions to a continuous accumulation of SrO on the surface and, in the case of reducing conditions, to the ongoing loss of oxygen from the Ti-enriched surfaces [72]. This indicates the importance of the details of the preparation process, the history of the crystals in terms of the thermal treatment and their defect characteristics.

The formation of droplets and terrace-like structures on the surface of ST after annealing for 24 hours at 1100 °C under oxidizing atmospheres was also reported [74]. The results of this work showed that the surface of ST is subject to a continuous enrichment of SrO_x. This extra material in droplet-like form seems to be liquid at elevated temperatures and may agglomerate in the course of heat treatment and, after prolonged annealing, give rise to the growth of regularly shaped micro-crystals on top of the surface, as depicted in Figure 1-13.

The surface of these micro-crystals was found to consist almost exclusively of SrO. The same kind of behavior was observed for single-crystalline ST doped with either acceptors (Fe) or donors (La, Nb).

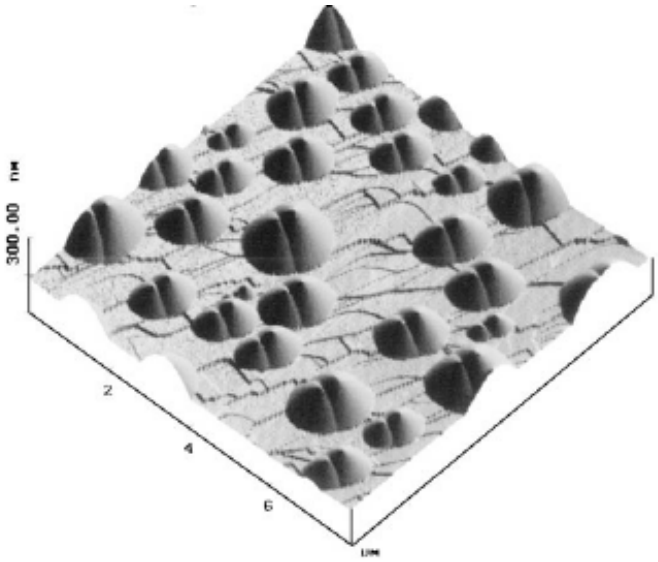

Figure 1-13: Topography of polished (100) surfaces of single crystalline ST, obtained by AFM after thermal treatment at 1100 ºC for 24h at ambient pressure [74].

Kazimirov et al. [75] studied the structural transformations at the (001) ST surface under oxidizing conditions. The formation of small droplets was also reported by the authors, but it was attributed to monoclinic TiO [75]. Another investigation [49] reported the formation of second phases consisting of strontium and oxygen on the surfaces of lanthanum (A site) as well as niobium (B site) donor doped ST single crystals with donor concentrations above 0.5 at.%, under oxidizing conditions. The second phases revealed to be of SrO_x composition. Neither lanthanum nor niobium were found in the precipitates and there was no evidence for the formation of RP phases. Dwell temperatures between 1050 ºC and 1350 ºC and annealing times between 10 h and 31 days were used in the experiment. The amount of the second phase on top of the surface increased with the amount of dopant, the annealing temperature and the

oxidation time. The authors [49] proposed an equilibration mechanism for the oxidation of the material based on the fast establishment of a local defect equilibrium at the surface and the slow in-diffusion of strontium vacancies. At temperatures below 1000 ºC, strontium vacancies and SrO complexes are formed in the first monolayer via a surface point defect reaction. At higher temperatures, the volume diffusion of strontium vacancies into the crystal causes an accumulation of SrO at the surface. The volume diffusion of strontium vacancies is regarded as the rate limiting step in the re-equilibration process.

1.4 Sintering of the titanates

1.4.1 Basics of sintering

In the fabrication of ceramics, sintering is the processing step of consolidation powder compacts by the use of thermal energy [78]. The origin of this technique dates to the prehistoric era with the firing of pottery. Nowadays, sintering encountered a wide range of application, from bulk ceramic components to powder metallurgy. However, sintering was studied fundamentally and scientifically only after the 1940s and since then remarkable progresses have been made.

Sintering processes are usually divided into three types [79]: vitrification, liquid phase sintering and solid state sintering. Solid state sintering occurs when the powder compact is densified wholly in the solid state at the sintering temperature. On the other hand, liquid phase sintering occurs when a liquid phase is present in the powder compact during sintering, but the liquid is not enough to fill the porosity after the rearrangement process. In general, liquid phase sintering allows a reduction in process cost but usually results in a degradation of some properties, for example, mechanical properties [78, 79]. Finally, vitrification occurs when the heat treatment produces enough viscous liquid to fill completely the porous spaces between particles in the starting powder compact. Solid state sintering has received the greater amount of attention because it has a great interest in the production of technical ceramics and it is easier to model. Most of the sintering models were developed considering this type of sintering [79].

Solid state sintering is usually divided into three overlapping stages: initial, intermediate and final [78]. The initial stage is characterized by the formation of necks between particles and its contribution to the compact linear shrinkage is limited to 2-3%. During the intermediate stage, considerable densification (up to ≈ 95% of the theoretical density) occurs before the closure of the pores. The final stage involves densification from the isolated pore state to the final densification.

The driving force for sintering is the reduction in the free energy of the system [79] through the reduction of its internal surface areas. This occurs via densification and coarsening [79-81], the basic phenomena of sintering [78, 79], whose combined effects determine the microstructural evolution of the compact. By densification in solid state sintering, a gas/solid interface is replaced by a lower energy solid/solid interface (grain boundary), whereas by means of coarsening a reduction in the extent of free surface and of specific grain boundary area is achieved by conversion of many small pores and grains into fewer larger ones.

1.4.2 Sintering studies on titanates

Since the electrical properties of titanate ceramics strongly depend on the microstructure it is of great importance to control its sintering behaviour [82]. Therefore, the optimization of the microstructure by control of the processing parameters is of great concern.

Sintering studies of titanates has often been inconclusive in terms of the rate-determining mechanism for densification. In sintering kinetic analysis, the diffusion species and the diffusion path still remain controversial [83]. Titanates are very sensitive to impurities in the starting powders. The impurities influence greatly the sintering behavior of these materials and its final properties and are, therefore, probably responsible for many of the contradictions found in the literature.

Various factors were found to affect microstructural evolution and resultant microstructure in titanate materials: cation non-stoichiometry [1, 84], liquid phase distribution [84, 85], dopant concentration [86, 87], sintering atmosphere [88], lattice defects including twins [89, 90] and dislocations [91, 92], among others. These factors will be briefly reviewed in the next sections regarding BT and ST ceramics.

1.4.2.1 $BaTiO_3$ sintering studies

The sintering behavior of BT has received a great deal of attention. The effect of microstructure, namely aspects regarding porosity, grain size distribution and second phases, among others, on the electrical properties of BT has been the driving force behind the sintering studies on this material.

Below the eutectic temperature, GG in BT is very slow [84]. Above the eutectic temperature, the presence of the eutectic liquid during sintering promotes densification by enhancing the diffusion of cations via the dissolution and precipitation processes [84, 93]. However, accompanying the enhanced densification, the liquid phase usually gives rise to abnormal GG (AGG) [84, 89, 94-96]. AGG, also called secondary recrystallisation, is characterized by the rapid growth of a small number of grains, which consume the small matrix grains originating a coarse-grain microstructure [84].

1.4.2.1.1 Effect of nonstoichiometry

Nonstoichiometry has a strong influence on the sintering behavior of BT. The common knowledge is that TiO_2-excess enhances the sintering behaviour of BT whereas the BaO excess hinders it and acts as grain refiner [83, 97, 98]. In fact, TiO_2 excess is often used as a sintering aid in the sintering of titanates [84, 94]. In BT, the TiO_2 excess promotes an eutectic melt at about 1312 ºC [84]. Eutectic temperatures of 1320 ºC and 1332 ºC have also been reported [96]. The liquid formation temperature can be lowered by the presence of impurities [83]. As an example, in the presence of SiO_2 impurities, liquid eutectic may form around 1250 ºC [83, 93]. Phase diagrams for the BaO-TiO_2 system are shown in Figure 1-14.

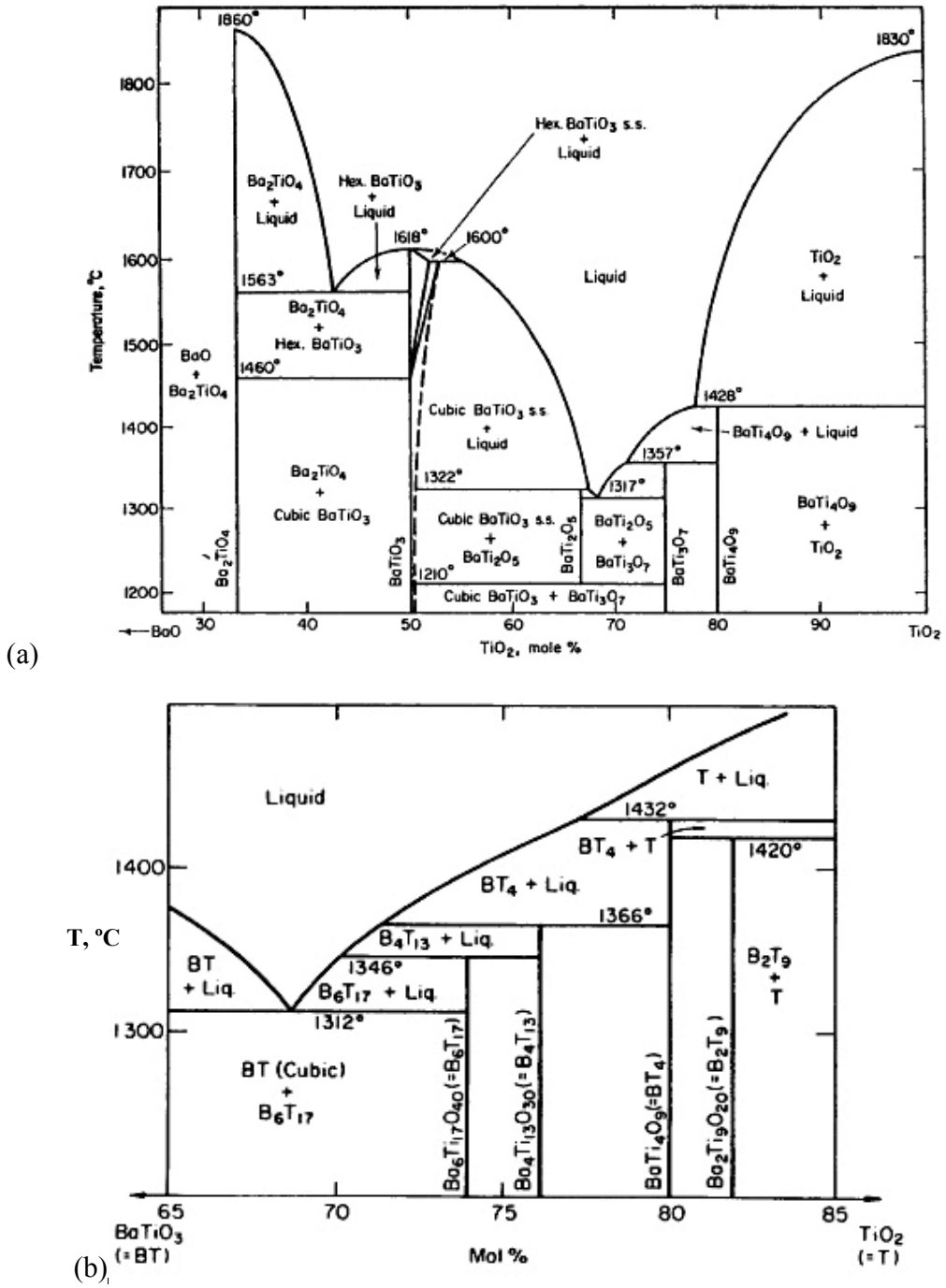

Figure 1-14: (a) Phase equilibria in the system BaO-TiO_2 [99]. (b) Later version of the diagram [100]. (Both taken from [2]).

For the optimization of several properties, AGG must be controlled. A general method of controlling AGG is the addition of seed grains to the powder. With the addition of 1 to 5 wt% seed grains of ≈ 4 μm average crystallite size to a 2 mol% TiO_2 excess BT powder of ≈ 0.4 μm average grain size, Hennings et al. [84] obtained smaller average grain sizes with increasing amount of seed grains. The seed grains acted as nuclei at the exaggerated GG and the larger number of uniformly distributed abnormal growing grains resulted in more uniform microstructures and smaller average grain sizes. As will be seen, various dopants and reducing sintering atmospheres also suppress AGG.

The abnormal GG in the Ti rich BT compositions has been related to the formation of eutectic liquid phases. Liquid phase during sintering enhances the diffusion of cations and, consequently, sintering but it does not improve the final densification of the samples. The eutectic melt inhibits rather than promotes further densification above the eutectic temperature. Many pores are trapped in grains due to the fast GG above the eutectic temperature. On the other hand, the densification of the Ba excess and stoichiometric samples has also been reported to be promoted at a lower temperature than the eutectic, as observed by several researchers [83, 93, 96]. For materials containing no liquid phase former, such as stoichiometric and Ba rich compositions, densification can proceed only by means of solid state diffusion. The GG is slow and fine grain microstructure results [93].

Lin et al. [83] observed that, below the eutectic temperature, the sintered density of the TiO_2 excess (Ba/Ti = 0.997) composition was always lower than that of the BaO excess one (Ba/Ti = 1.013) up to a sintering period of 150 h. The BaO excess powder was better sintered with a final relative density of 97 % while the TiO_2 excess composition presented a relative density of 83 %, as shown in Figure 1-15.

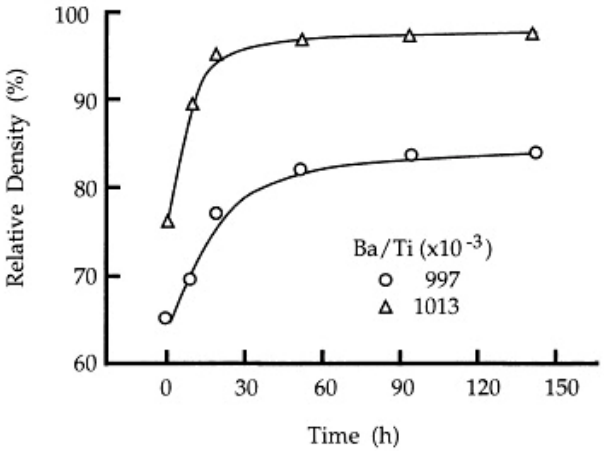

Figure 1-15: Sintering kinetic curves at 1215 ºC (below the eutectic temperature) for TiO_2 excess (Ba/Ti = 0.997) and BaO-excess (Ba/Ti = 1.013) BT compositions [83].

Similar results were obtained by Erkalfa et al. [96]. The variation of the densification in the temperature range of 1250 to 1360 ºC, for compositions with Ba/Ti ratios between 0.98 and 1.0025, observed by the authors is depicted in Figure 1-16. Below the eutectic temperature of 1332 ºC, the densification of Ba and Ti excess samples was lower than that of the stoichiometric composition, being higher for the Ba excess composition than for Ti rich one. Addition of 0.2 mol% of TiO_2 (added as $TiCl_3$) to the stoichiometric composition had a marked effect, being the densification for this composition higher than for the other compositions. Above the eutectic temperature, the densification of Ti-excess composition became higher than the densification of the Ba rich one.

In the same investigation [96], at 1335 ºC, slightly above the eutectic temperature, Ti-excess, stoichiometric and $TiCl_3$ added compositions showed 97% densification. Above 1335 ºC the Ti excess and the Ba-excess samples showed de-densification (reduction of the attained density), as shown in Figure 1-16, due to the pores trapped within the grains and at the grain boundaries. However, the stoichiometric and $TiCl_3$ added compositions did not show this effect [96]. Demartin et al. [101] reported that de-densification was due to the simultaneous effect of different processes, namely AGG, pore coalescence and closure of porosity. These effects are interrelated and are influenced by the impurity content.

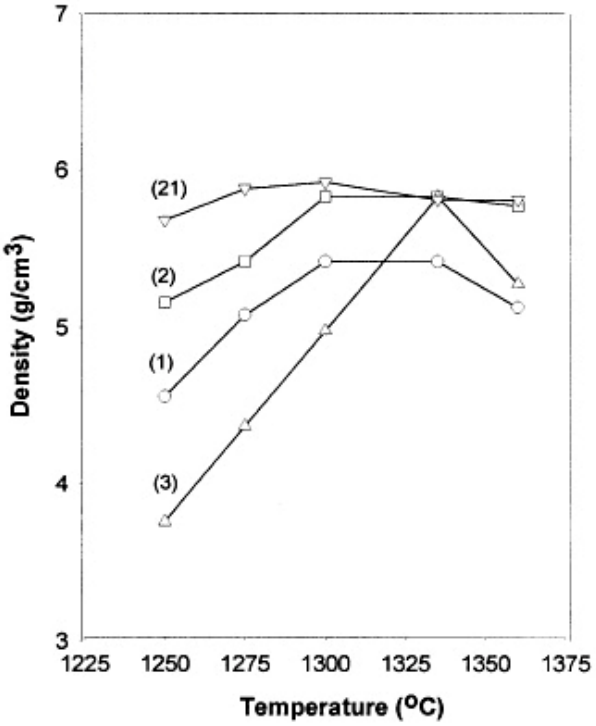

Figure 1-16: Densification of BT: (1) Ba excess (Ba/Ti ratio of 1.0025), (2) stoichiometric, (3) Ti excess (Ba/Ti ratio of 0.98), (21) stoichiometric composition with addition of 0.2 mol% TiO_2 [96].

Nonstoichiometry also affects the morphological evolution during sintering. Microstructures obtained by Lin et al. [83] are presented in Figure 1-17 (a) for TiO_2 excess BT and (b) for BaO excess BT. A platelet type microstructure was observed by several researchers in TiO_2 excess BT compositions sintered below the eutectic temperature [83, 89] but not in BaO excess ones. Erkalfa et al. [96] observed platelet like GG also in BaO excess BT.

The microstructure of a 0.997 TiO_2 excess composition sintered at 1215 ºC is shown in Figure 1-17 (a) [83]. Elongated plate-like grains exhibiting faceting and twins are characteristic of low temperature sintered TiO_2 excess samples. During sintering, the twin plate-like grains grow at the expense of the fine powder particles until they gradually impinge on another and form a rigid network, hindering further densification and retaining large residual pores.

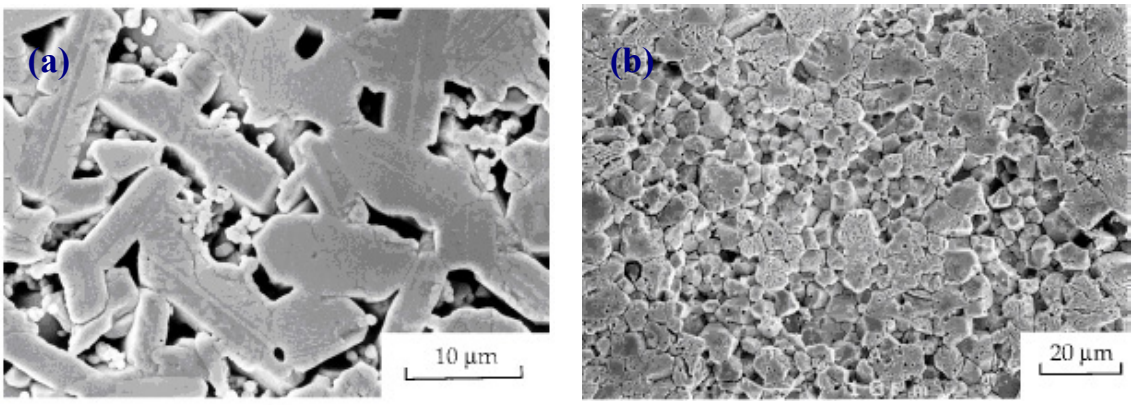

Figure 1-17: Microstructures of nonstoichiometric BT: (a) 0.997 TiO_2 excess BT sintered at 1215 ºC for 55 h [83]; (b) 1.013 BaO excess BT sintered at 1215 ºC for 100 h [83].

Plate-like faceted grains are the characteristic microstructural feature of TiO_2 excess composition sintered below the eutectic liquid temperature [83]. GG occurs trough the coalescence of grains taking place on the {111} plane. Coarsening, leading to the formation of plate-like grains, appears to be a process of lower activation enthalpy than densification for the sintering of TiO_2 excess BT [83]. Faceting is lost after annealing above the eutectic temperature, and most of the abnormally grown plate-like grains become more polygonal in shape.

Regarding BaO excess BT compositions, a microstructure is shown in Figure 1-17 (b), for 1.013 BaO excess BT sintered at 1215 ºC for 100 h [83]. The twins usually observed in the TiO_2 excess samples are normally not observed in BaO excess compositions. The GG is slow and fine grain microstructures result. AGG is rarely reported for these compositions.

From the observation that many abnormal grains in TiO_2 excess BT are elongated parallel to the twin lamellae [83, 89, 96] and that the preferential growth of the abnormal grains occurs along the twin lamellae, a twin assisted growth mechanism has been suggested [89]. The abnormal grains have the {111} habit planes, forming flat grain boundaries with neighboring small grains [89, 90]. The {111} twin lamellae having reentrant edges have been considered to provide preferential nucleation sites for rapid GG, where atoms can easily be

attached [102]. It has been suggested that such a flat shape is possible, because an eutectic liquid is formed which leads to an amorphous layer between the crystallographic surfaces of abnormal grains and neighboring matrix grains [84]. However, as have been said, AGG with plate-like faceted grains occur in BT mainly at temperatures below the eutectic temperature [83, 89, 94]. Actually, many polycrystalline materials [103] are reported to undergo AGG without any introduction of liquid phases. These results suggest that AGG with plate-like grains is correlated with the GB structure. Such a correlation between AGG and grain boundary faceting has also been observed in other polycrystals such as a Ni-base alloy [103]. The structural change at the interface, from faceted to rough, can occur by temperature increase [104], dopant addition and atmosphere change [102].

Lee, Sigle et al. [95] reported AGG behavior in BT with 0.2 mol% excess TiO_2, when sintered in air at 1250°C, below the eutectic temperature. Abnormal grains had polyhedral shape and their grain boundaries were flat and parallel to the {111} planes of the abnormal grains. Many grain boundaries between matrix grains were faceted with small steps and long segments parallel to the {111} planes of one of the grains. It was shown through High Resolution Transmission Electron Microscopy (HRTEM) (Figure 1-18) that such a polyhedral shape is correlated with an ordered grain boundary phase between the abnormal grains and neighboring matrix grains.

It was concluded that AGG in connection with polyhedral abnormal grains could lead to the formation of an ordered phase at the boundaries between the abnormal grain surfaces and neighboring small grains without the presence of a liquid phase [95]. Due to the excess of Ti the ordered grain boundary phase presented a distorted structure different from the perovskite structure. The faceting observed in the matrix grain boundaries suppressed the growth of most grains and the selective growth of a few grains occurred. During AGG the boundaries between the {111} abnormal grain surfaces and neighboring small grains appeared to rotate to the energetically favorable {111} planes, accommodating the excess Ti solutes. The ordered phase, shown in Figure 1-18 b), was attributed to the accommodation of the excess Ti at the boundaries between the abnormal grain surfaces and neighboring small grains [95].

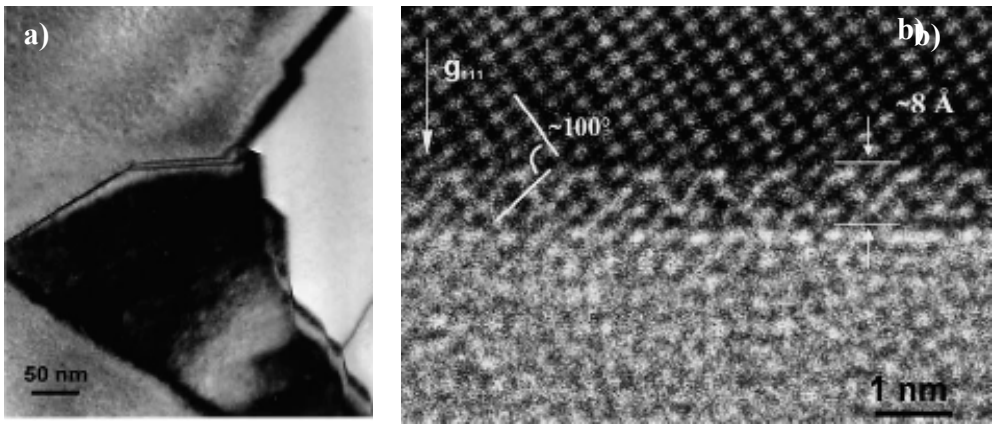

Figure 1-18: TEM microstructural images of BT with 0.2 mol% excess TiO_2 sintered in air at 1250 ºC: a) image showing three faceted grain boundaries meeting each other at a triple junction; b) High-resolution TEM image of the grain boundary between an abnormal grain (the upper one) and a small matrix grain showing an ordered intermediate phase [95].

1.4.2.1.2 Effect of the sintering atmosphere

The relation between grain boundary structure and the sintering atmosphere has been studied in the last few years [89, 102, 105]. Lee et al. [89] examined the effect of sintering atmosphere on GB faceting and concluded that the twin-assisted abnormal growth of BT grains occurs only when the grain boundaries are faceted. When 0.1 mol% excess TiO_2 BT samples were annealed in air, GB faceting occurred and concurrently AGG happened. However, when the air-annealed sample was reannealed in hydrogen the faceted GBs became defaceted (curved) and the AGG stopped.

The effect of oxygen partial pressure on the GG of 0.4 mol% TiO_2 excess BT was studied by Jung et al. [105]. Samples were sintered in air with and without a prior H_2 heat treatment at temperatures of 1250 ºC (below the eutectic temperature) and 1350 ºC (above the eutectic temperature). AGG occurred at both temperatures, for samples without a prior heat

treatment. With a 10 h H_2 heat treatment before air sintering, the average grain size increased during the heat treatment, thus decreasing the driving force for the growth of faceted grains. The interfaces of BT are faceted under a high oxygen partial pressure while those under a very low oxygen partial pressure are rough [89, 106]. AGG was observed to occur only in systems with faceted interfaces [59, 89], as stated previously, and so the AGG was suppressed above and below the eutectic temperature by the prior H_2 heat treatment. This experimental observation shows that AGG in faceted systems can be suppressed by controlling the initial size of faceted grains [105].

Further developments have been made recently. The structural transition of grain boundaries between faceted and rough and the resultant GG behavior were studied in 0.1 mol% TiO_2 excess BT sintered at 1250 ºC for 50 h by systematically changing oxygen partial pressure from ≈ 0.2 to ≈ 10^{-19} atm [102]. A gradual decrease in facet fraction with pO_2 reduction was observed. GG behavior and thus grain boundary structure were very different depending on pO_2. At high pO_2 of 0.2 atm, {111} twins formed and {111} twin-assisted AGG occurred. As pO_2 decreased, the formation of {111} twins was suppressed and a fraction of faceted boundaries became rough. The boundary roughening under a very low oxygen partial pressure was considered to be due to increased oxygen vacancy concentration at the boundary and increased entropy contribution. In these samples, GG was suppressed showing stagnant GG behavior. Further reduction of pO_2 changed the growth behavior from stagnant to abnormal in the absence of {111} twins.

1.4.2.1.3 Effect of dopants

Dopant addition also has a significant influence on the sintering behavior and morphological evolution during sintering of BT [86, 87, 107]. Figure 1-19 (a) shows isothermal sintering curves obtained by Lin et al. [86] for La_2O_3-doped TiO_2-excess BT (Ba/Ti

= 0.997) for several doping levels. The obtained sintered density increased with increasing dopant concentration, from 0.15 to 0.50 mol%.

However, the constant heating rate (CHR) sintering curves (Figure 1-19 (b)) obtained by the same authors did not exhibit the increasing trend of sintered density with La_2O_3-doping. Donor doping had in fact retarded rather than enhanced densification when samples were sintered by CHR to temperatures ≤ 1350°C. Furthermore, the decrease in density was more pronounced with higher doping levels of 0.80 mol%. The doping levels of 0.15 and 0.30 mol.% La_2O_3 resulted in dedensification, starting at ≈ 1325°C for 0.15, lower than 1425 °C of 0.30 mol.% La_2O_3 (Figure 1-19 (b)).

For doping levels higher than 0.30 mol%, however, the reduction of the density was not observed even for sintering up to 1490°C, far exceeding the eutectic point. High dopant levels have delayed the desintering until higher sintering temperature or probably stopped it all together [86]. The authors [86] attributed the densification retardation in the TiO_2-excess BT compositions doped with La_2O_3 to the slow dissolution kinetics of La^{3+} into the BT lattice.

SEM micrographs, shown in Figure 1-20, are from La_2O_3-doped samples sintered at 1215°C for 100 h after a CHR of 5 °C min^{-1} [86]. The large plate-like abnormally grown grains, characteristic of undoped TiO_2-excess samples sintered at low temperatures [83], can be observed in a reduced number in the 0.15 mol.% La_2O_3-added samples (Figure 1-20 (a)), but they were suppressed by La_2O_3-doping with dopant levels equal or higher than 0.30 mol.% (comparing Figure 1-20 (a) with Figure 1-20 (b)). In this case, homogeneous microstructures with refined grain size smaller than 1 μm was obtained (Figure 1-20 (b)) due to the formation of second-phase $La_2Ti_2O_7$ that pinned the grain boundaries and affected the surface energy anisotropy.

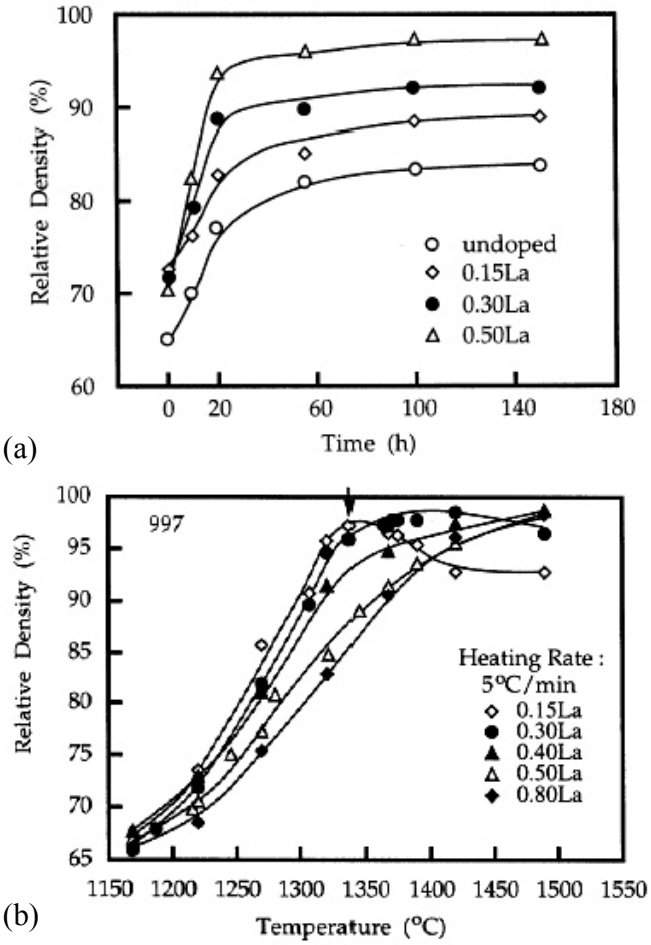

Figure 1-19: (a) Final sintered density versus dopant concentration for La_2O_3-doped TiO_2-excess 0.997 BT compositions sintered at 1215°C up to 150 h [86]; (b) CHR sintered density-temperature dependence for sintering of La_2O_3-doped TiO_2-excess 0.997 BT compositions [86].

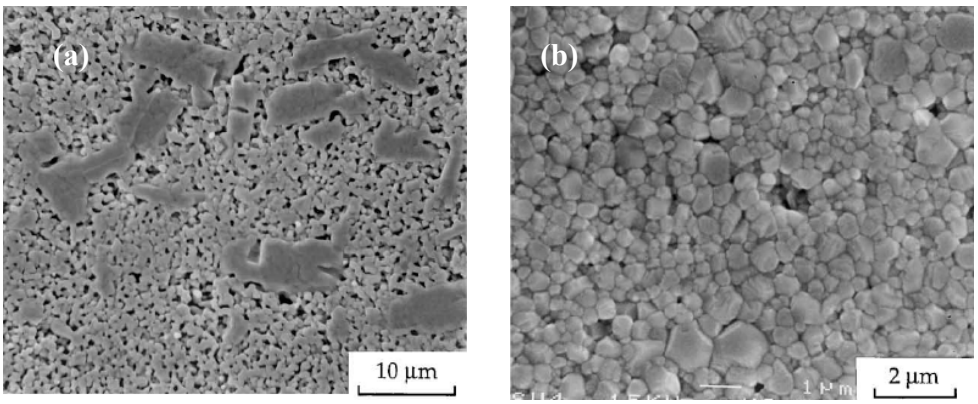

Figure 1-20: Microstructures of La_2O_3-doped TiO_2-excess 0.997 BT compositions, (a) 0.15 mol.% and (b) 0.30 mol.% sintered at 1215°C for 100 h [86].

Adding high contents of Y_2O_3 to a BaO-excess 1.013 BT powder has been reported to hinder the densification [108]. The observed effect was characterized by a significant decrease of the final sintered density from 97 to 79% on increasing the doping level from 0.15 to 0.80 mol% Y_2O_3 when samples were sintered at 1215 °C for 100 h. Grain growth inhibition was observed in samples doped with Y_2O_3 contents higher than 0.3 mol% and sintered at 1350 °C (or lower temperatures) for 50 h where the final sintered density of 95% has been reached. Exaggerated grain growth represented by intragranular spherical pores and abnormal large grains having concave boundaries was found in 0.15 mol% Y_2O_3-doped samples. No intragranular pores could be detected for samples doped with 0.30 mol% Y_2O_3 or for higher dopant contents. Intergranular second-phase particles were distinguished in BT samples with 1.0 mol% Y_2O_3 addition.

Studies with donor-doped BT ceramics exhibit a conductivity anomaly and a grain size anomaly with respect to donor concentration. The grain size anomaly is the dramatic inhibition of the anomalous grain growth in BT ceramics when the amount of donors reaches the limit of about 0.3 - 0.5 at% [86, 109]. This critical dopant concentration needed for the grain-growth inhibition to become effective has been called grain growth inhibition threshold (GGIT) [86].

Beyond the GGIT grain growth in doped BT ceramics is effectively hindered, the microstructure refined and the semiconductivity sharply reduced [110]. This coincidence indicates a definitive correlation between the defect species responsible for GG and vacancy compensation [110]. Donor dopant incorporation occurs either by electronic compensation at low concentrations or by vacancy compensation at high concentrations [111]. At low dopant concentrations, the electronic compensation explains the semiconductivity. As the concentration of dopants increases, segregation at the grain boundaries occurs and the compensation mechanism change from electrons to vacancies. The dopant segregation to the grain boundaries inhibits GG and the vacancy compensation mechanism results in decrease of the semiconductivity.

The solid-solution defect model has usually been adopted [83, 93] to qualitatively interpret the enhanced sintering kinetics and the inhibition of grain-growth in donor-doped BT [83]. It is often argued that cation vacancy generated upon donor doping enhances densification by increasing the volume diffusivity [83]. Desu et al. [111] investigated highly donor-doped BT and proposed a model of donor (Nd^{3+})-segregated grain boundaries. In fact, a model of positive-charged Ti-enriched grain boundary and negative-charged space-charge layer in the donor-doped compositions has been suggested [112] for both BT and ST, as mentioned before. The existence of second-phases along grain-boundaries in La_2O_3 [86], Er_2O_3 [113] and Y_2O_3-doped samples [107] with high doping levels also suggests that grain-boundaries were pinned by second-phase precipitates and consequently their mobility reduced, decreasing the coarsening rate. The enhanced densification is not only due to the densification assisted by increased cation diffusivity. In fact, sinterability is improved by both enhanced densification (by solid-solution defect) and suppressed coarsening (by second-phase pinning) [107].

1.4.2.2 ST sintering studies

Sintering studies in ST are very limited in number and mainly restricted to GG. Due to this limited availability of studies in the literature, no sub-sections were considered in the following part of the text, concerning the sintering studies of ST.

Figure 1-21 presents the phase diagrams for the SrO-TiO_2 system. The solubility limits for excess SrO or TiO_2 are quite low. It was reported that ST with TiO_2 excess of 0.5 mol% (Sr/Ti = 0.995) shows the presence of Ti-rich second phase [114]. Above the solubility limit, TiO_2 appears as a second phase in the form of discrete grains. The solubility of excess TiO_2 in ST is somewhat larger than in BT in which the second phase appears in triple points and grain boundaries [114]. On the other hand, SrO excess is fully accommodated in the ST perovskite lattice as a three-dimensional mosaic of single-layered rock-salt blocks, forming the so called Ruddlesden–Popper (RP) structure, allowing the SrO excess in the ST lattice in the form of interlayers [41]. This type of incorporation does not occur in BT [97].

It can be seen in Figure 1-21 that the SrO-TiO_2 system shows an eutectic at about 1440 ºC for the Ti rich compositions. The resulting liquid phase has a significant impact in the sintering behavior of this material. In the case of the Sr rich side of the diagram, the eutectic is above 1800 ºC, far above the temperature range used in this work.

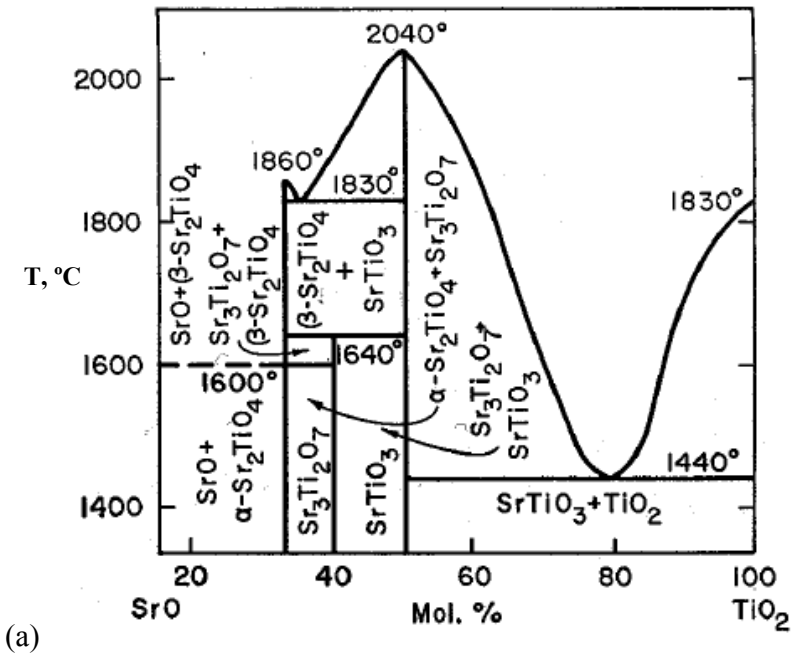

(a)

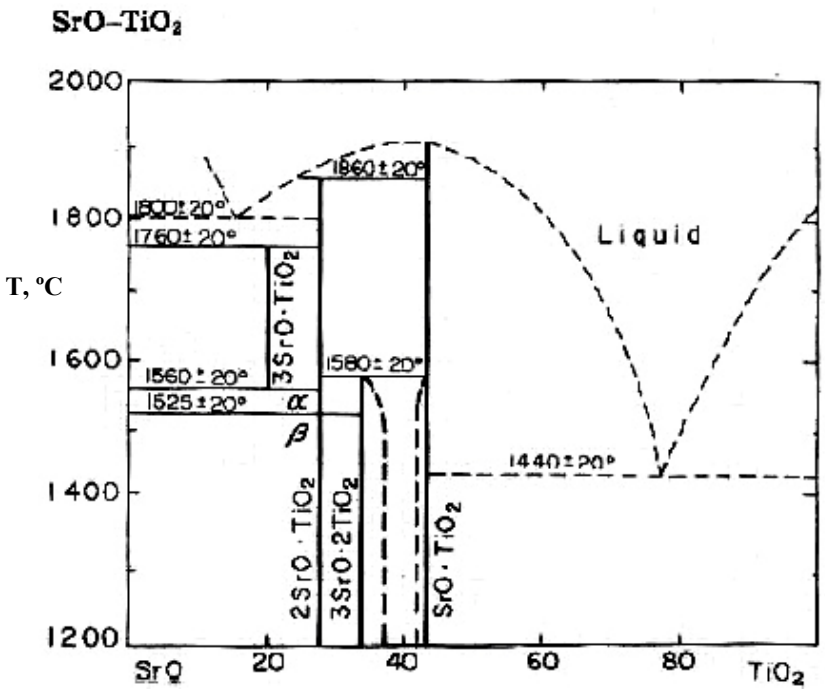

(b) wt %

Figure 1-21: Phase diagrams for the SrO-TiO_2 system ((a) [115] and (b) [116])

AGG of ST ceramics in the presence of a liquid phase is very similar to that of BT ceramics [117]. Nonstoichiometry also affects the sintering behaviour of ST ceramics. It is often found that TiO_2 excess deteriorates densification while SrO excess improves it, as observed by Chen et al. [118] when sintering ST ceramics with Sr/Ti ratios from 0.99 to 1.02 and an addition of 0.5 wt% V_2O_5 as a liquid phase sintering agent at 1250 - 1400 ºC. Rodlike TiO_2 precipitates were formed in the Ti rich composition at 1250 ºC. Above 1300 ºC, the precipitates were no longer observed and AGG occurred originating a coarse grain microstructure with grain size from 10 to 20 μm. Similar behaviour was observed for the stoichiometric composition that showed, however, better packing and no precipitates. For 1 mol% excess SrO composition the authors observed a compact microstructure and normal grain growth (NGG) over the entire sintering temperature range. Grain size was about 2 to 4 μm at 1250 ºC and 3 to 10 μm at 1350 ºC. The 2 mol% excess SrO composition presented similar behaviour but with a lower GG rate.

For 0.5 mol% NbO_5 doped ST (Ti/Sr ratio from 1 to 1.02), it was reported that, for samples sintered at 1480 ºC (above the eutectic temperature in Figure 1-21), for 30 - 240 min, and at 1500 - 1570 ºC, 0 min, the microstructures displayed typical AGG processes, in which large grains were nucleated and grew at the expense of the fine ones [82, 117]. As the Ti/Sr ratio increased from 1 to 1.02, both the time for nucleation of abnormal grains and the onset temperature of AGG increased, whereas the number of abnormal grain nuclei tended to decrease. This behaviour is similar to that observed in BT ceramics by Hennings et al. [84] who reported that the nucleation and growth rates of abnormal grains of TiO_2-excess BT ceramics increased with increasing sintering temperature and decreasing excess of TiO_2.

Preliminary results were reported by Tkach et al. [1] on the effect of nonstoichiometry on the microstructure of ST ceramics with Sr/Ti ratio between 0.997 and 1.02. The authors found a cubic symmetry and no second phases for all the compositions, for samples sintered in air at 1500 ºC for 5h. All samples revealed rather dense microstructures and a remarkable difference in the grain size for Ti-rich and Sr-rich composition was found, as depicted in Figure 1-22. The average grain size of ST ceramics with Sr/Ti = 0.997 was about 20 μm, whereas Sr/Ti = 1.02 yielded ceramics with an average grain size of 6 μm.

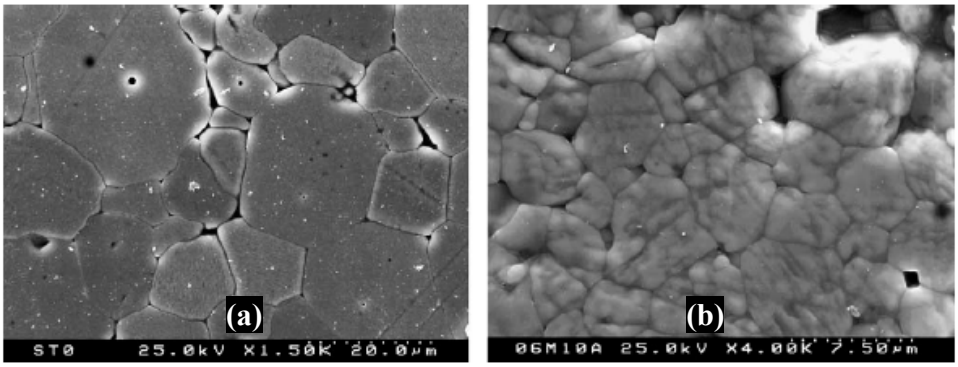

Figure 1-22: SEM micrographs of ST ceramics with Sr/Ti ratio of (a) 0.997 and (b) 1.02, sintered at 1500 ◦C for 5 h [1].

In the processing of ST-based materials for electronic components, a donor dopant is usually added [87] and sintering is carried out in a reducing atmosphere to enhance the electrical conductivity [52, 59]. The donor addition and reducing atmosphere sintering can cause the formation of ionic vacancies (strontium and oxygen, respectively) in the ST lattice, as mentioned previously. Kinetic processes like grain boundary migration and GG in titanate systems depend on the characteristics of their grain boundaries rather than their grain interior [84, 89, 91]. Segregation at the grain boundaries and its structure has an important influence on the sintering behaviour of ST, as in BT, and are greatly influenced by the sintering atmosphere [88].

Chung et al. [59] reported that ionic vacancies in ST can induce interface roughening and suppress AGG. As the concentration of strontium or oxygen vacancies increases with the addition of a donor or reduction in oxygen partial pressure, the shape of the interface changes from faceted to rough and the anisotropy in interface energy disappears [59]. In another investigation, Chung et al. [88] studied the effect of sintering atmosphere on grain boundary segregation and GG in 2.4 at % Nb-doped ST. The authors found no abnormal grains in samples sintered for 2h at 1360 ºC, below the eutectic temperature, in air and in H_2. However, the average grain size in the sample sintered in H_2, where Nb ions were segregated in the boundary regions, was much smaller than in the sample sintered in air. For a sintering temperature of 1460 ºC, above the eutectic temperature, the GG was also strongly inhibited for

the samples sintered in H_2. This suppression of the GG was attributed to the grain boundary dragging of segregated Nb and to the reduction in Ti vacancy concentration in H_2 atmosphere.

The GGIT regarding dopant concentration is also observed for ST [87, 119], with similar trends for the variation of the grain size with the dopant concentration to those seen before for La_2O_3 [86] and Y_2O_3 doped BT [107]. The results of You et al. [119] for WO_3 doped ST sintered in various atmospheres and temperatures of 1470 °C and 1435 °C are presented in Figure 1-23. At 1470 °C and 1435 °C, the grain size was observed to be not dependent on the pO_2 for the range under study**.** The variation of grain size with the amount of dopant for both the sintering temperatures follows the same trend: it increases until the level of the dopant reaches about 0.3 mol%.

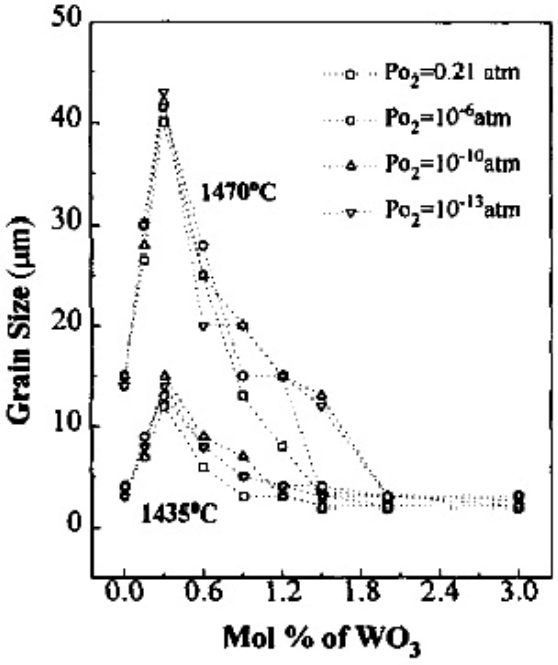

Figure 1-23: Influence of tungsten content on the grain size of ST sintered for 4 h at 1435°C and 1470 °C with variable oxygen partial pressures [119].

Sr-W-rich second phases were reported by the investigators [119] in specimens with a dopant content of 3 mol%. The Sr rich phases were ascribed to the movement of Sr ions from

the lattice to the grain boundaries leaving compensating vacancies in the lattice. The formation of Sr vacancies was considered to account for the decrease in the conductivity after 1.2 mol% dopant addition.

Inaculescu et al. [87], for samples sintered at 1400 ºC for 3 h, reported a dense microstructure for pure ST, which was not much affected by the introduction of small Sb amounts, $x < 0.0075$ in $SrTi_{1-x}Sb_xO_3$. For a Sb content $x = 0.0075$ an AGG process occurred, leading to a heterogeneous microstructure. Over this Sb proportion, the average grain size started to decrease so that for the ceramics with high Sb content a very homogeneous microstructure consisting of small grains was observed. The authors correlated this microstructure feature with the change of compensation mechanism of the supplementary charge induced by the Sb^{5+} donor dopant [87]. Below a critical Sb concentration ($x \leq 0.0075$) the compensating defects were considered to be the electrons resulted from the Ti^{4+} towards Ti^{3+} reduction, whereas over this concentration value a strontium vacancy compensation mechanism was assumed as the most probable. This is in accordance with the observed coincidence between the GGIT and loss of semiconductivity in titanates [108, 110].

Lattice defects were also reported to enhance the GG in titanates. Chung et al. [91] showed that dislocations enhance the interface mobility and thus promote the GG of ST in the presence of a thin liquid film between grains and suggested that an uneven distribution of dislocations might be a cause of AGG in polycrystalline ST. In another investigation, the authors observed that the GG promoted by dislocations in the ST system occurs only when the grain boundary is wetted with an amorphous phase [92].

2 Experimental Procedure

2.1 Powder preparation

In the present work, four compositions were used, with different Sr/Ti ratios, as shown in Table 2-1. The samples were prepared by solid state reaction.

Table 2-1: Compositions used in this work.

Sr / Ti	Designation	Composition
0.997	ST 0.997	$Sr_{0.997}TiO_{2.997}$
0.999	ST 0.999	$Sr_{0.999}TiO_{2.999}$
1	ST	$SrTiO_3$
1.02	ST 1.02	$Sr_{1.02}TiO_{3.02}$

The powders were prepared by the mixed oxide method. The raw powders of $SrCO_3$ and TiO_2 (Merck) were firstly dried and weighed according to the compositions described above. The powders were then mixed with ball milling in alcohol in a planetary mill, using Teflon pots with zirconia balls for 5 h. After that, the mixtures were dried in an oven at 100 ºC for more than 12 h.

The 5h milling time was selected after a set of experiments with several milling times, from 1 to 8h. For milling times longer than 5h there was no decrease of the powders average particle size and higher levels of agglomeration occurred, as determined by particle size distributions obtained by Coulter measurements.

After analysis of the Differential Thermal Analysis (DTA) / Themogravimetry (TG) curves obtained with a heating rate of 5 ºC/min, represented in the Figure 2-1 for the mixture

of $SrCO_3$ and TiO_2 of the stoichiometric composition, the calcination temperature of 1050 ºC was selected.

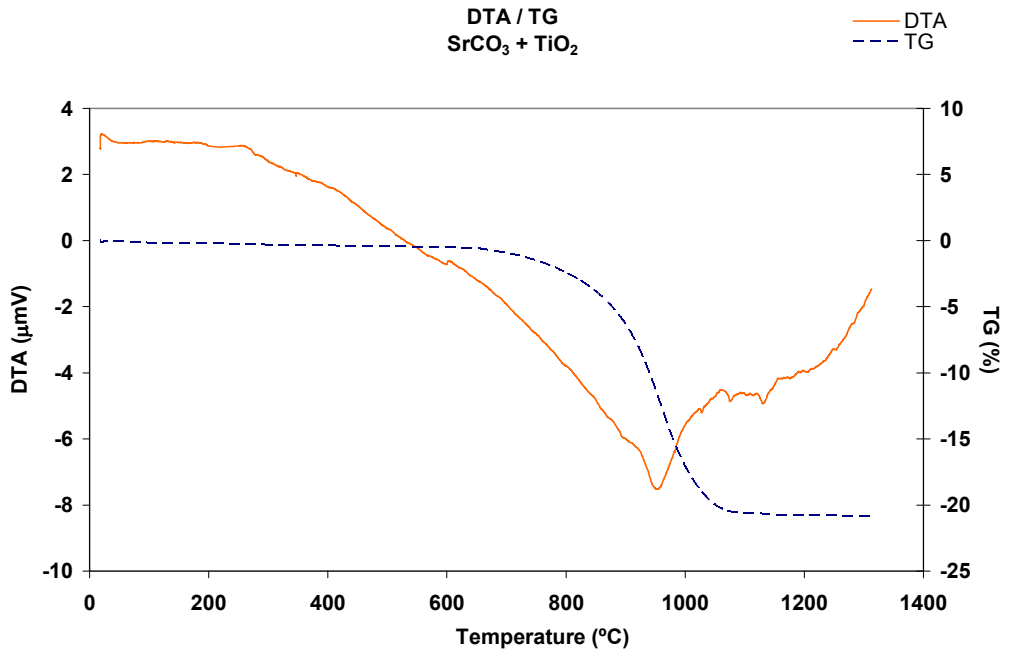

Figure 2-1: Thermal analysis of the mixture of $SrCO_3$ and TiO_2 according to the stoichiometric composition, with a heating rate of 5 ºC/min.

The DTA curve presents an endothermic peak around 950 ºC that is accompanied by a significant mass loss on the TG curve. This endothermic peak is characteristic of $SrCO_3$ and corresponds to an orthorhombic-hexagonal phase transformation [120, 121]. The mass loss comes from the decomposition of $SrCO_3$ that begins with the phase transformation [121] and the consequent release of carbon dioxide (CO_2). At the same time, the formation of ST occurs according to the reaction (2-1):

$$SrCO_3 + TiO_2 \rightarrow SrTiO_3 + CO_2 \uparrow \qquad (2\text{-}1)$$

The milled powders were packed in alumina crucibles and calcined at 1050 ºC for 6 hours. Three calcination cycles were performed, until XRD showed monophasic powders for all the compositions under study. After each calcination step, powders were milled and dried under the previously mentioned conditions. The prepared powders were kept in closed glass recipients in an oven at 100 ºC to avoid surface reactions with air that could lead to aging of the powders.

The particle size distributions after the ball milling were determined using Particle Size Analyzer (Coulter LS 230). The average particle size was also determined from mass specific surface area (A_{sv}) measurements (BET, Gemini 2370 V5.00), as:

$$G_{0BET} = \frac{6}{A_{sv} d_t} \qquad (2\text{-}2)$$

where d_t is the theoretical density. A scanning electron microscope (SEM) Hitachi, S-4000 SEM / EDS was used to observe the powders and from the obtained micrographs, the average particle size was determined.

2.2 Dilatometric characterization

The dilatometric characterization was performed in a computer assisted vertical dilatometer (Linseis, mod. 4 L70-2000) heating the samples from room temperature to 1500 ºC with heating rates of 2, 5, 10 and 20 ºC/min, in air, for all the compositions under study. For preparation of pellets for dilatometric measurements, the calcined powders were packed manually inside “rubber sleeves”, tied in both ends and rolled between two glass plates, in order to smooth the surface. Then, the pellets were isostatically pressed under 200 MPa. The resulting cylindrical pellets were cut into ~5 mm x 5 mm x 7 mm parallelepipeds according to the size of the dilatometer cell.

For the GG studies, the calcined powders were uniaxially pressed at 50 MPa (Carver Laboratory Press, Fred S. Carver Inc., USA) with a steel die into green pellets of 1 cm in diameter and about 4 mm in thickness. The pellets were then isostatically pressed at 200 MPa (Stansted Fluid Power Ltd., England / Autoclave Engineer, Inc., USA).

The time between the pressing step and the dilatometric experiments was no more than seven days to prevent the pellets from aging, even though they were closed in glass recipients in an oven at 100 ºC. As can be seen in Figure 2-2, until seven days the shrinkage curves from the dilatometric measurements of ST, heated at 5 ºC/min, are almost coincident, whereas for twenty four days after pressing a significant change in the shrinkage of the sample is observable. The differences indicated the degradation of the samples, maybe related to surface phenomena. This effect was out of the purpose of this work. The understanding of this behavior requires further studies that are now ongoing.

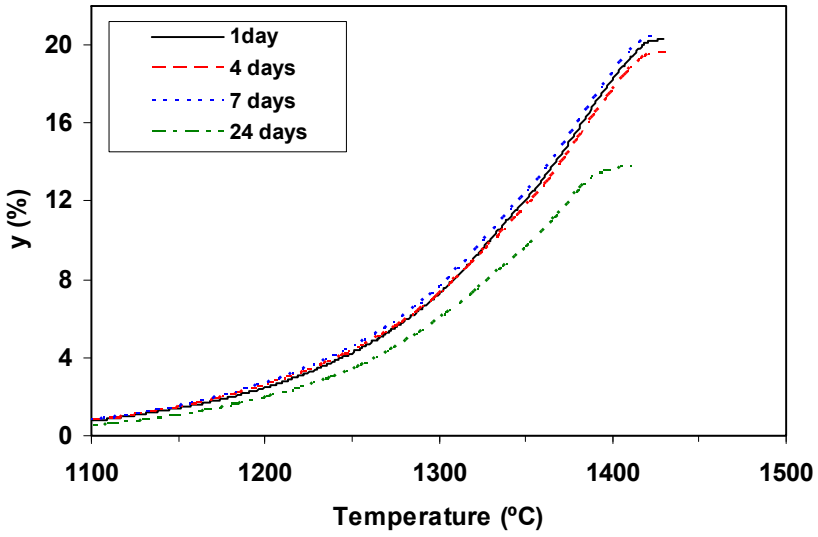

Figure 2-2: Shrinkage curves for ST, with a heating rate of 5 ºC/min, 1, 4, 7 and 24 days after the pressing of the pellets.

2.3 Sintering conditions for grain growth studies

The pressed samples were sintered in air at the sintering temperatures of 1400, 1450 and 1500 ºC with holding time variable from 1 to 8h. A horizontal tubular furnace was used and the working tube and sample holder were in alumina.

2.4 Density measurements

The densities of the sintered samples were measured by the Archimedes' method using water as the immersion liquid. The value of the measured density was calculated by the following equation [122]:

$$d = \frac{d_{liq} W_1 - d_{air} W_2}{W_1 - W_2} \ (\mathrm{g/cm^3}) \qquad (2\text{-}3)$$

where W_1 and W_2 are the weights of the sample in air and in liquid, respectively; d_{air} and d_{liq} are the densities of the air and liquid, respectively, at 1 atm and room temperature: d_{air} = 0.001185 g/cm^3 and d_{liq} = 1 g/cm^3. The densities of the green pellets were determined geometrically because the Archimedes' method proved to be inadequate once that the liquid dissolved portions of the pellets. A value of 5.12 g/cm^3 [123] was assumed for the theoretical density of ST.

2.5 X-ray measurements

The XRD analysis at room temperature was performed using a powder X-ray diffractometer (Rigaku D/Max-B, Cu Kα). The samples were first ground with an agate mortar and pestle. For the phase identification of the calcined powders, the diffraction angle (2θ) varied in the range of 4-80º with a scanning rate of 3 º/min. For the determination of the lattice

parameter, the diffraction angle (2θ) varied in the range of 20-110º and the scanning rate was 1 º/min. The lattice parameter was calculated by a least square approach fitting of the XRD data using Rietveld refinement WinPLOTR software.

2.6 Microstructure characterization

The microstructures of fracture surfaces and polished and thermally etched sections of the samples were observed with scanning electron microscopy / energy dispersive spectroscopy (SEM / EDS). For green compacts, fracture surfaces were used for observation after coating with a carbon film. For sintered samples, small pieces were mounted in an epoxy resin and then polished with 800# grinding paper and then with diamond pastes stepwise from 6 to 1 μm. Then the samples were thermally etched in a furnace at temperatures 50-100 ºC lower than the sintering temperatures. The etching depth was controlled by the holding time (from 3 to 10 min) and observations with an optical microscope (Nikon, HFX-IIA). After carbon deposition, the microstructures were obtained, and micro-chemical analysis and X-ray map profiles were performed with a scanning electron microscope (Hitachi, S-4000 SEM / EDS).

The microstructural and chemical characterization of the ceramic samples was also carried out on sintered samples by means of transmission electron microscopy / energy dispersive spectroscopy (TEM / EDS) (Hitachi 9000). For TEM analysis, the two faces of the samples were carefully polished with 800# grinding paper in order to reduce their thickness to approximately 80 μm. The samples were then glued to a copper ring and ion beam milled using a BAL-TEC Ion Mill (RES 100).

2.7 Grain size measurements

The grain size distribution of the samples was determined taking at least 300 grains in SEM micrographs, using the AnalySIS (Soft Imaging System GmbH) software. The area of the section of the grains or the particle projected area was measured and then its equivalent diameter, D_{SEM}, was calculated considering circular areas. The average grain or particle size, G, was then determined from the average equivalent diameter, $\overline{D}_{SEM}$, by the expression [101]:

$$G = 1.22\overline{D}_{SEM} \qquad (2\text{-}4)$$

3 Results

The results obtained in this work are presented in this chapter. The results comprise powder structure and morphology characterization, CHR dilatometry experiments and respective kinetic analysis, in which the activation energies for densification and sintering exponents are calculated for the initial stage. After that, the microstructure of sintered compacts is characterized. The kinetics of GG in the final sintering stage is also studied in two selected compositions and the activation energies and grain growth exponents calculated.

3.1 Powders characterization

XRD spectra of the calcined powders of all the compositions under study are shown in Figure 3-1. For all the compositions, the observed lines are consistent with the cubic crystallographic structure of ST and no second phases were detected, within the detection limits of the XRD technique.

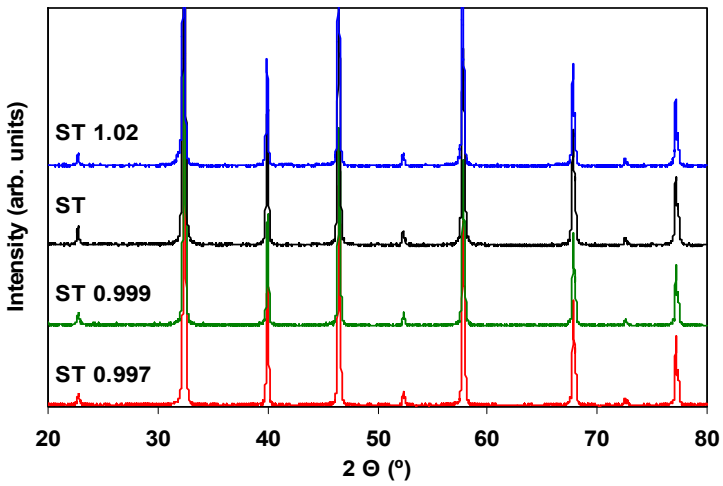

Figure 3-1: XRD spectra of the powders of all the compositions under study after calcination at 1050 ºC.

Figure 3-2 depicts the SEM micrographs of the calcined powders. Figure 3-3 shows the particle size distributions of calcined powders, obtained by laser diffraction (Coulter) for all the compositions. It can be seen in Figure 3-2 that the powders present near equaxied grains and equivalent shape. The size distributions for all the compositions in Figure 3-3 are equivalent too. SEM micrographs in Figure 3-2 and the second and third peaks of the particle size distributions, shown in Figure 3-3, evidence some degree of agglomeration of these calcined powders.

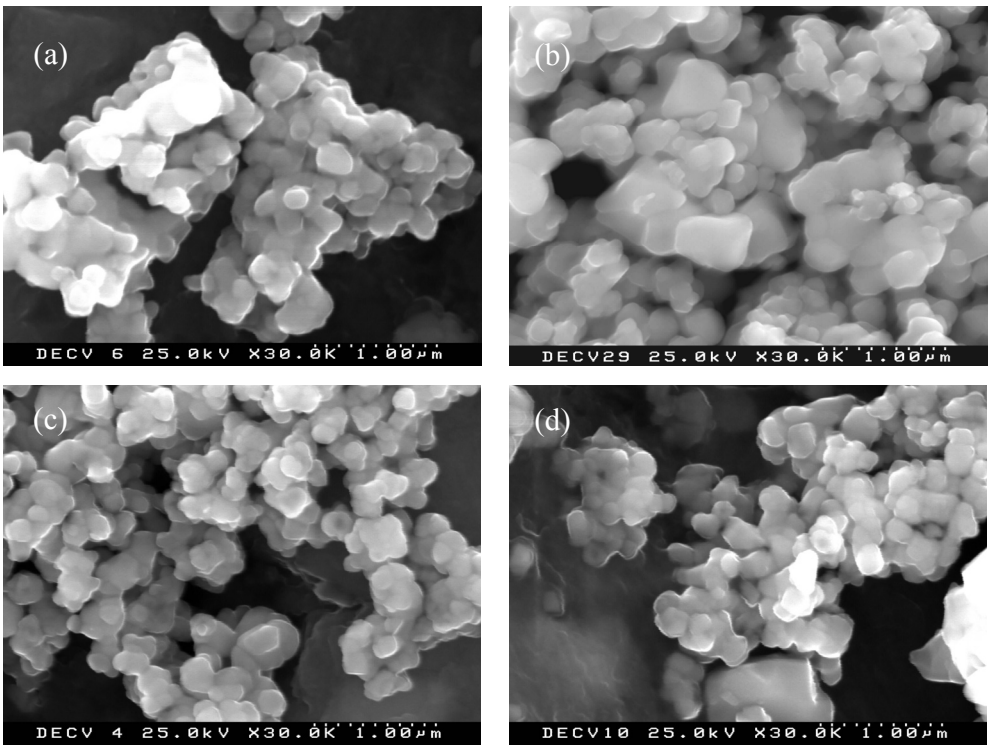

Figure 3-2: SEM micrographs of the powders (a) ST 0.997, (b) ST 0.999, (c) ST, (d) ST 1.02.

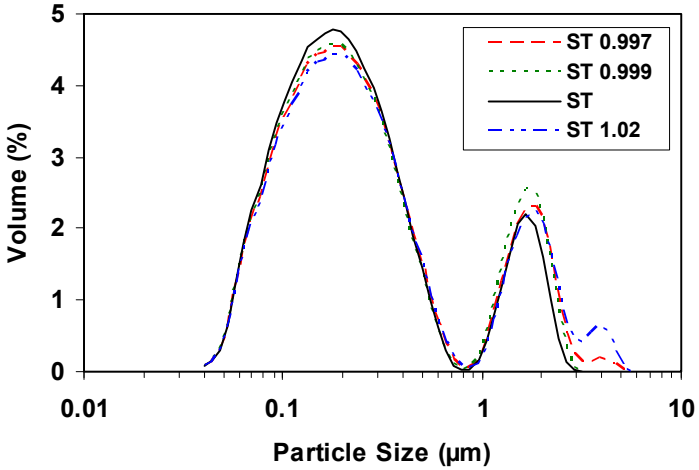

Figure 3-3: Particle size distribution of the calcined powders, obtained by Coulter.

SEM micrographs of the green pellets prepared from the calcined powders, in Figure 3-4, show that no significant particle agglomeration is observed in the pressed compacts. The particle equivalent diameter, D_{SEM}, distributions determined from the SEM micrographs, are presented in Figure 3-5. The correspondent average particle sizes ($G_{0\ SEM}$) are presented in Table 3-1, together with the average particle size determined by laser diffraction ($G_{0\ Laser}$) and BET surface area ($G_{0\ BET}$) measurements. $G_{0\ SEM}$ values are close to the $G_{0\ BET}$ ones, while $G_{0\ Laser}$ values are larger than the previously mentioned. This observation suggests again that the second and third peaks of the particle size distributions in Figure 3-3 come from particle agglomeration in the powder suspensions and that no significant agglomeration will remain in the powder compacts.

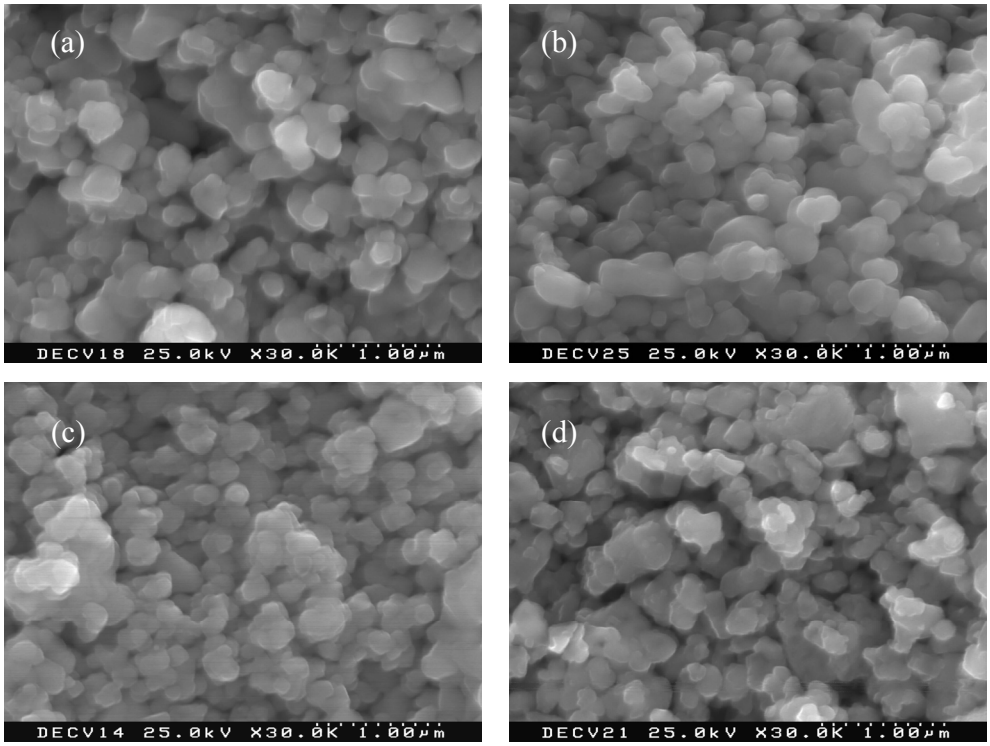

Figure 3-4: SEM microstructures of the green compacts for all compositions. (a) ST 0.997, (b) ST 0.999, (c) ST, (d) ST 1.02.

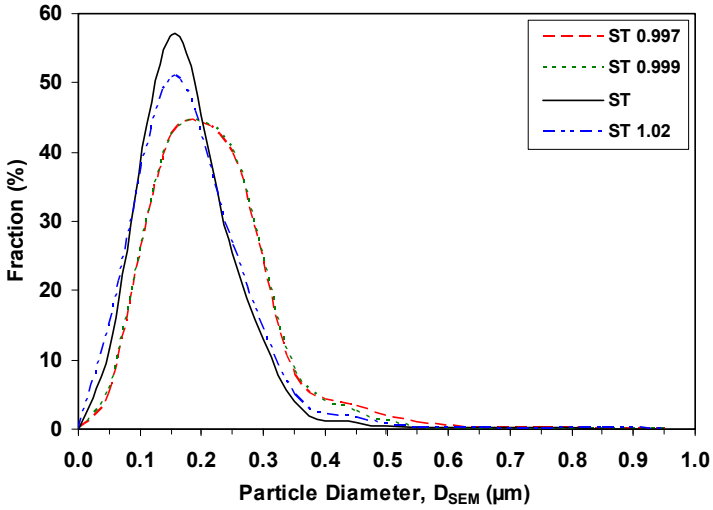

Figure 3-5: Particle equivalent diameter distribution of the green compacts for all compositions, obtained by SEM.

Table 3-1: Average particle size of calcined powders for all the compositions, measured by different techniques. The amount of Zr contamination, determined by Inductively Coupled Plasma (ICP), is also indicated.

Sr / Ti	$G_{0\ Laser}$ (µm)	$G_{0\ BET}$ (µm)	$G_{0\ SEM}$ (µm)	Zr (ppm)
0.997	0.52	0.32	0.28	150
0.999	0.49	0.43	0.27	230
1	0.43	0.27	0.25	70
1.02	0.59	0.32	0.24	270

$G_{0\ Laser}$ – average particle size measured by Coulter

As expected from the observed similarity of the compact microstructures (Figure 3-4) and the near equivalent particle size distributions (Figure 3-3 and Figure 3-5) the green density of the pressed compacts using the same pressing conditions is nearly constant for all the compositions and around $\rho_0 = 0.53 \pm 0.02$. It was also observed by SEM a relatively uniform particle packing in all the compacts. The morphological characteristics of the powders are very important factors in the sintering process. The observed morphological similarity among the powders of the several compositions and respective compacts is very convenient for an easier identification of the effects of the chemical composition on the kinetics of sintering.

The possibility of Zr contamination during the milling step was checked by ICP analysis and, effectively, all powders showed some contamination with Zr impurities. However, the detected amount of Zr contamination is under 270 ppm, as can be seen in Table 3-1.

3.2 CHR dilatometry results

3.2.1 Shrinkage curves

The following graphs, from Figure 3-6 to 3-13, regarding linear shrinkage, *y*, and shrinkage rate, *dy/dt*, were constructed from the dilatometric data acquired during CHR sintering experiments, with heating rates of 2, 5, 10 and 20 ºC/min, for all the compositions under study.

The linear shrinkage, taken as $y = \frac{l_0 - l}{l_0}$ (l_0 is the initial length of the pellet) as a function of the temperature, at the several heating rates used, is presented in Figures 3-6, 3-8, 3-10 and 3-12 for ST 0.997, ST 0.999, ST and ST 1.02, respectively. The shrinkage rate, *dy/dt*, as a function of temperature at several heating rates is depicted in Figures 3-7, 3-9, 3-11 and 3-13 for ST 0.997, ST 0.999, ST and ST 1.02, respectively. Several experimental runs were performed for different heating rates for all the compositions. Because good agreement between the several experiments was found, the presented curves are representative of the observed behavior.

It can be seen from the figures that, for all the compositions, the shrinkage evolution is dependent on the heating rate. Shrinkage curves show a sigmoidal and apparently smooth shape on its variation with the temperature. It can also be observed that there are no significant variations on the onset of shrinkage, occurring at around 1100 ºC for all the compositions and heating rates. At around 1200 ºC, the curves corresponding to different heating rates become progressively more differentiated and the higher the heating rate, the greater the shift to higher temperatures. Therefore, the same shrinkage is obtained for higher temperatures with the increase of the heating rate. An increase of the shrinkage rate is also observed for increasing heating rates. The derivative curves, shrinkage rate (*dy/dt*), show that the smoothness of the shrinkage curves is only apparent for the Ti rich and stoichiometric compositions because these compositions exhibit two peaks of shrinkage rate. On the other hand, ST 1.02 composition is characterized by a monomodal evolution of the shrinkage rate with the temperature.

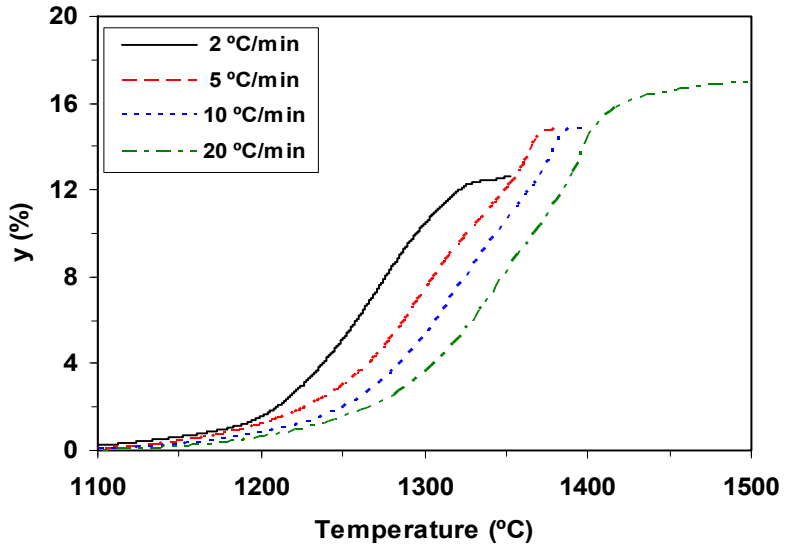

Figure 3-6: Linear shrinkage versus temperature, at several heating rates, for ST 0.997 composition.

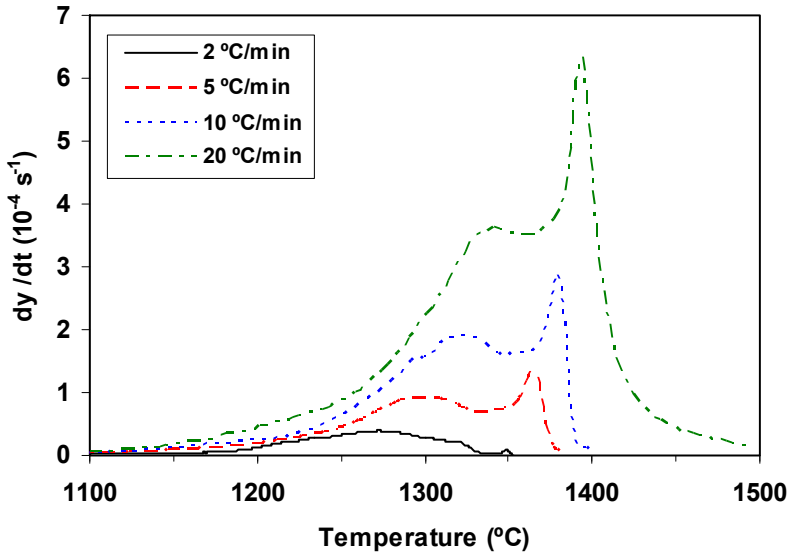

Figure 3-7: Shrinkage rate versus temperature, at several heating rates, for ST 0.997 composition.

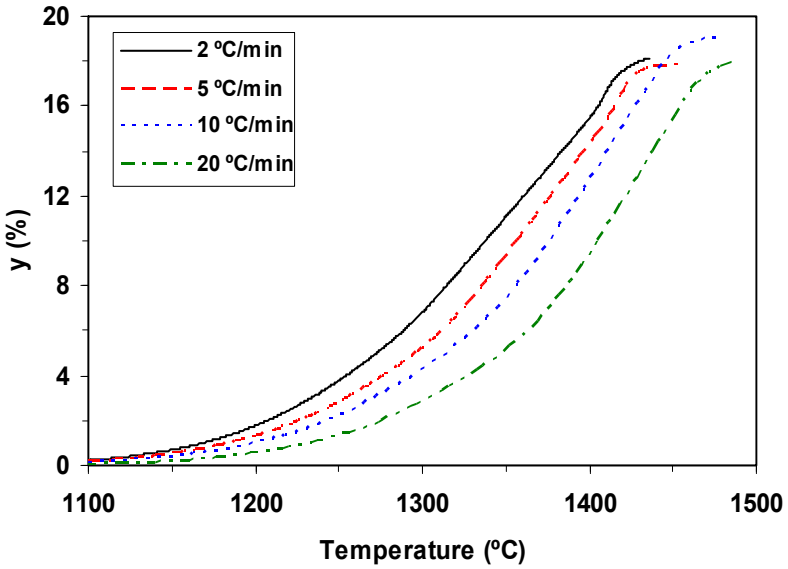

Figure 3-8: Linear shrinkage versus temperature, at several heating rates, for ST 0.999 composition.

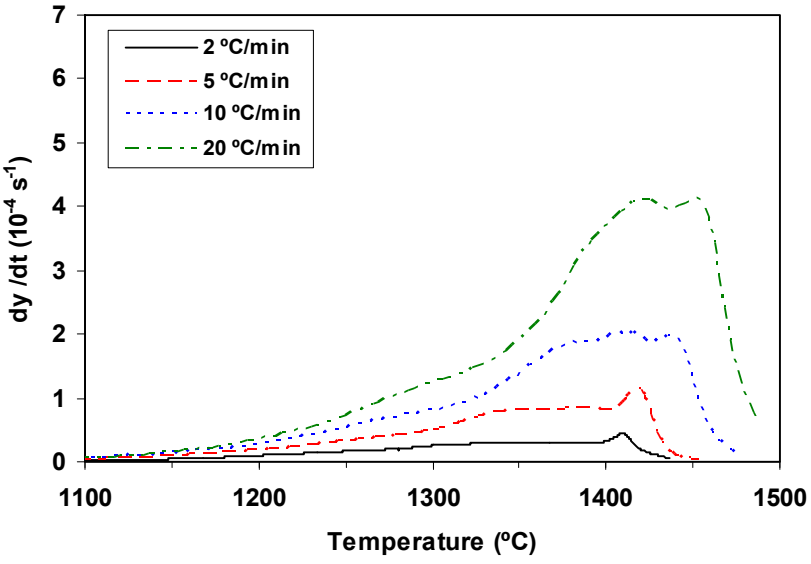

Figure 3-9: Shrinkage rate versus temperature, at several heating rates, for ST 0.999 composition.

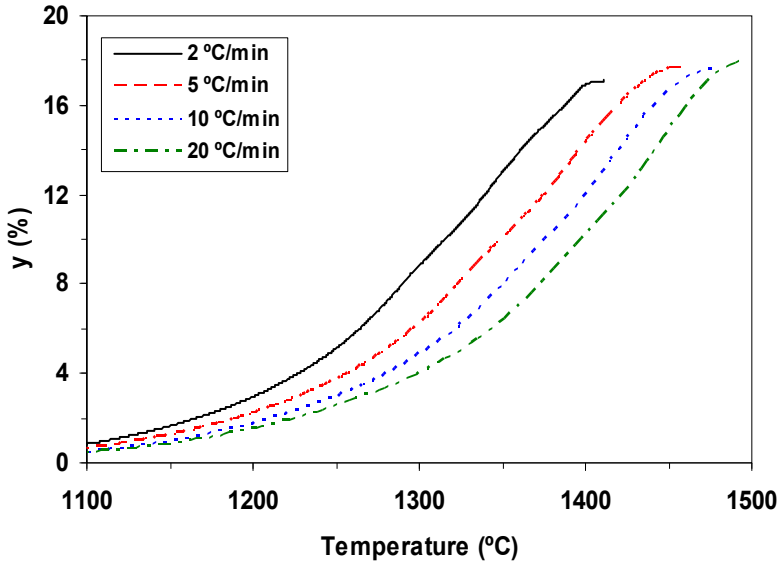

Figure 3-10: Linear shrinkage versus temperature, at several heating rates, for ST composition.

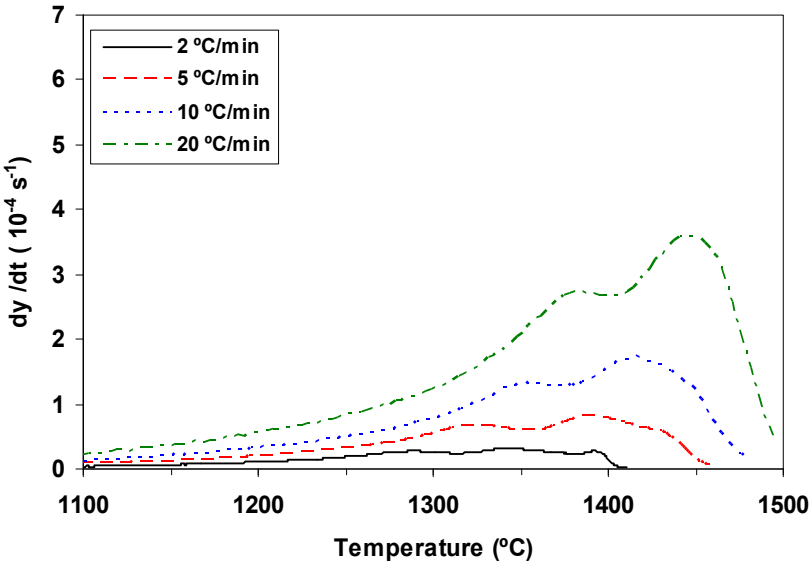

Figure 3-11: Shrinkage rate versus temperature, at several heating rates, for ST composition.

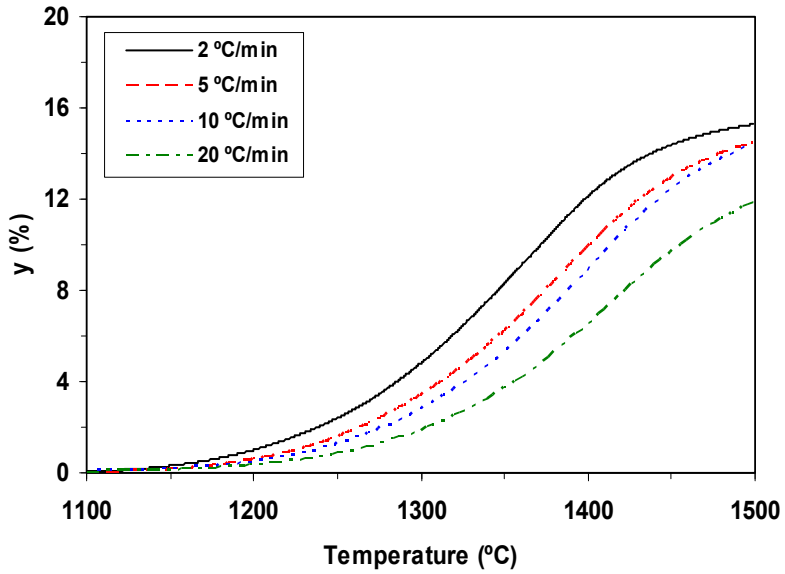

Figure 3-12: Linear shrinkage versus temperature, at several heating rates, for ST 1.02 composition.

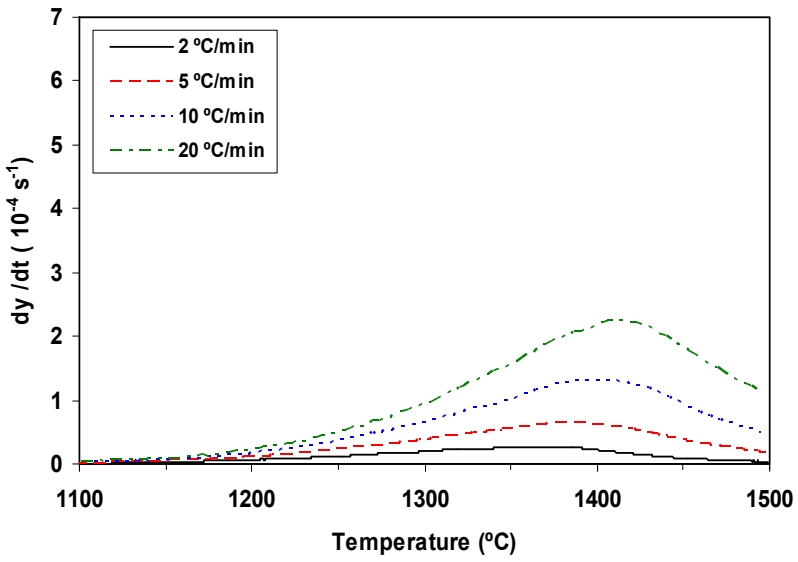

Figure 3-13: Shrinkage rate versus temperature, at several heating rates, for ST 1.02 composition.

In the following text, a comparative analysis of shrinkage and shrinkage rate for all the compositions under study is presented to highlight the effect of the Sr/Ti ratio on the sintering behavior. Linear shrinkage (Figure 3-14) and shrinkage rate (Figure 3-15), as functions of the temperature, for samples heated at a constant rate of 5 ºC/min are presented with the four compositions in the same figure.

No significant changes of the onset of sintering, around 1100 ºC, are observed with the variation of the Sr/Ti ratio, although the shrinkage of the stoichiometric composition initiates at slightly lower temperatures. The shrinkage curves in Figure 3-14 become more differentiated with the temperature increase showing a net reduction of the attained shrinkage at a constant temperature for increasing values of Sr/Ti.

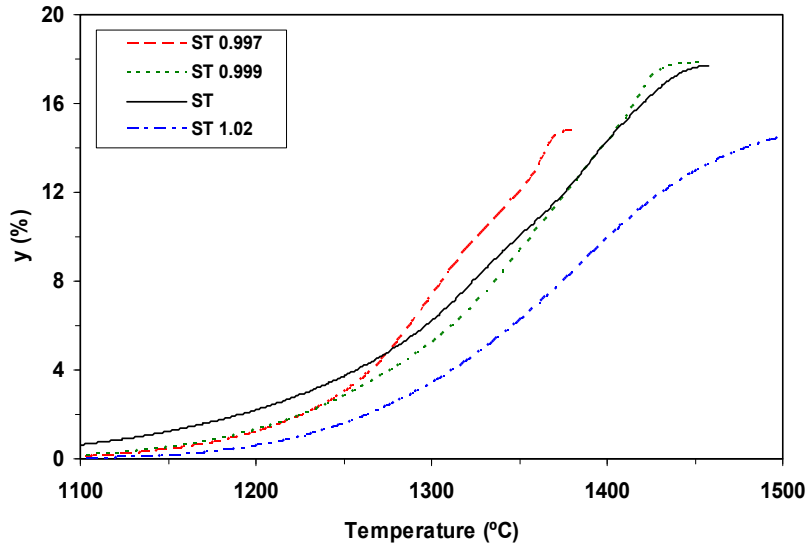

Figure 3-14: Linear shrinkage versus temperature, at a CHR of 5 ºC/min, for all the compositions under study.

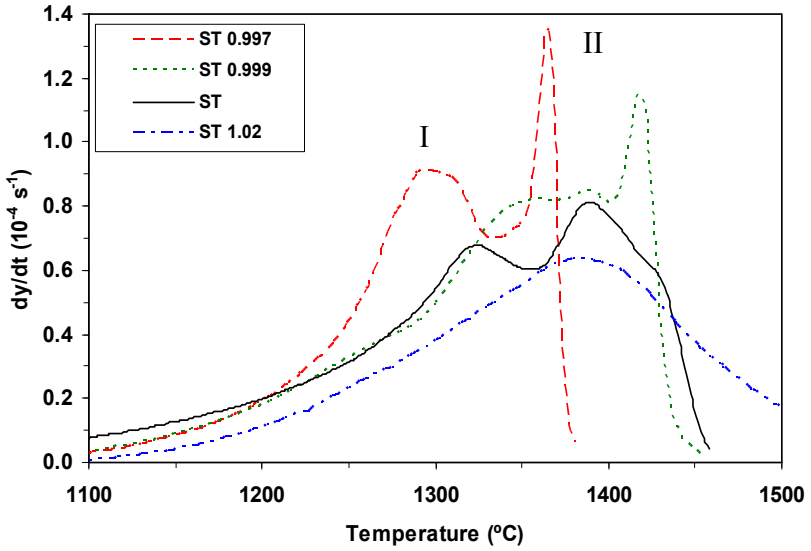

Figure 3-15: Shrinkage rate versus temperature, at a CHR of 5 ºC/min, for all the compositions under study.

The derivative curves in Figure 3-15 evidences the differences in the kinetics of densification for the various compositions. Two peaks of shrinkage rate identified as regime I and II (signalized in Figure 3-15 for ST 0.997, as an example) are observed for the stoichiometric and the Ti rich compositions, whereas a monomodal curve characterizes the dependence of the shrinkage rate on the temperature for the Sr rich sample. Moreover, the position of the peaks varies with the composition and a systematic decrease of the maximum value of the shrinkage rate with increasing the Sr/Ti ratio can be observed.

3.2.2 Kinetic analysis

3.2.2.1 Activation energy values

Using the data from the dilatometric experiments, it is possible to calculate the apparent activation energy and the kinetic exponent, characteristics of the densification mechanism involved in the sintering of the ceramics. The equations used for the calculation of the apparent activation energies and sintering exponents are presented in Table 3-2. Data from repetitions of dilatometric experiments for selected heating rates were included in the calculations.

The relative density, ρ, (equation (3-1)) was calculated from the shrinkage curves assuming isotropic shrinkage, that the mass of the powder compacts remains constant during sintering [124] and considering the green relative density, $\rho_0 = 0.53$, for all the compositions. The densification rate, $d\rho/dt$, expressed by equation (3-2), was obtained by the derivation of equation (3-1).

With the data resulting from these calculations, the apparent activation energy values, Q_d, were calculated considering the classical equation (3-3) for all compositions under study. It was assumed for the calculation of Q_d that G and Σ are unique functions of the density [124-126]. Considering equation (3-3), the representation of $ln\ (T\ d\rho/dt)$ versus $1/T$, at constant ρ values, leads to a linear dependence and the slope is equal to $(-\ (Q_d/R))$ from which the apparent activation energy can be easily obtained. Figures 3-16 to 3-19 represent the Arrhenius type dependence for the densification rate, $d\rho/dt$, at constant ρ values, for all the compositions. The calculated apparent activation energies at several relative densities are summarized in Table 3-3.

Table 3-2: Equations used in the calculation of the apparent activation energies and sintering exponents.

Equation	Nº	Reference
$\rho = \frac{\rho_0}{(1-y)^3}$	(3-1)	--
$\frac{d\rho}{dt} = \frac{3\rho_0}{(1-y)^4}\frac{dy}{dt}$	(3-2)	--
$\frac{d\rho}{dt} = \frac{C}{TG^m}\exp(-\frac{Q_d}{RT})\Sigma f(\rho)$	(3-3)	[124-126]
$yT^{\frac{-1}{s}} = (\frac{B}{c})^{\frac{1}{s}}\exp(-\frac{Q_d}{sRT})$	(3-4)	[127]
$y^{s-1}\frac{dy}{dt} = \frac{B'}{T}\exp(-\frac{Q_d}{RT})$	(3-5)	[127]

ρ - relative density; y - linear shrinkage; B, B', C - constants depending on the material and the mechanism; Σ - sintering stress; $f(\rho)$ - function of the density depending on the model used; G - average grain size; m - grain size exponent; R - gas constant; T - absolute temperature; c - heating rate; Q_d - activation energy for densification; s - sintering exponent.

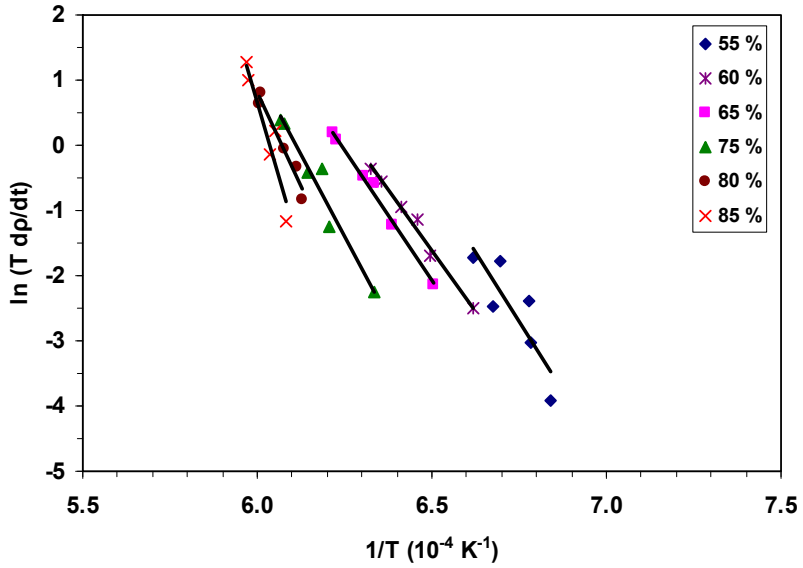

Figure 3-16: Arrhenius type plots for the densification rate, dρ/dt, at constant ρ values, for ST 0.997 composition.

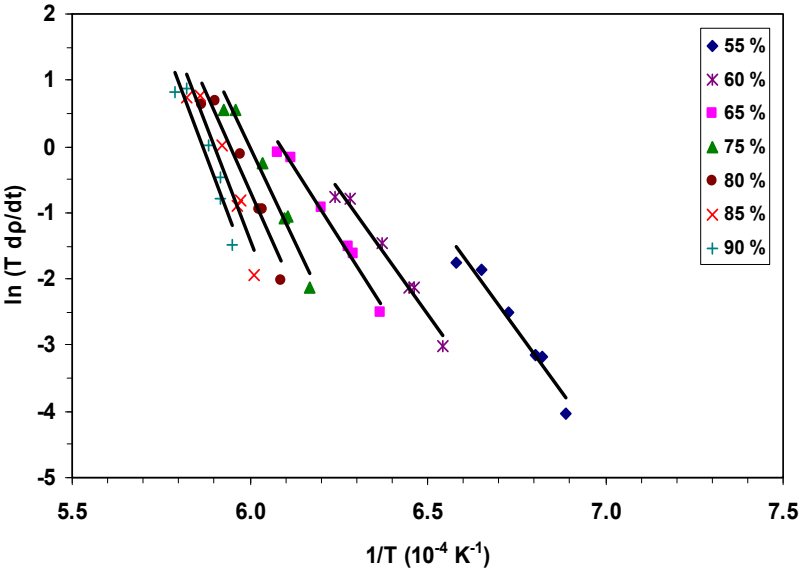

Figure 3-17: Arrhenius type plots for the densification rate, dρ/dt, at constant ρ values, for ST 0.999 composition.

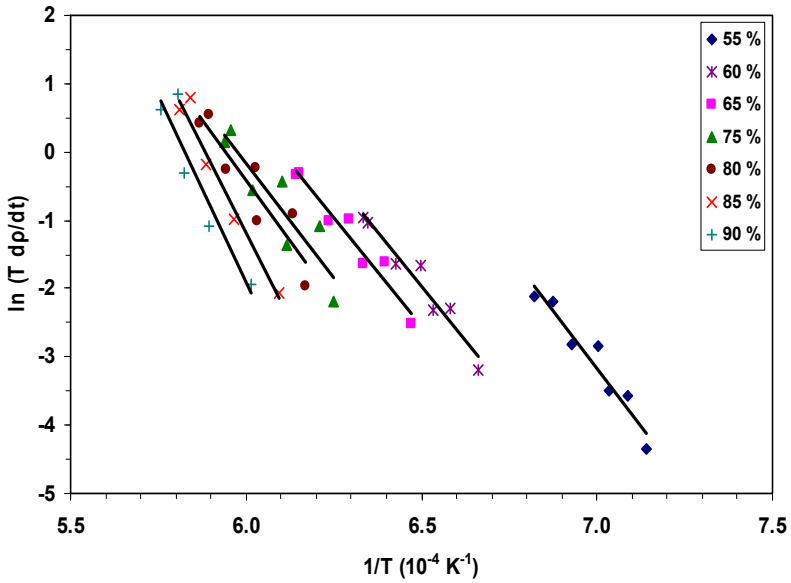

Figure 3-18: Arrhenius type plots for the densification rate, dρ/dt, at constant ρ values, for ST composition.

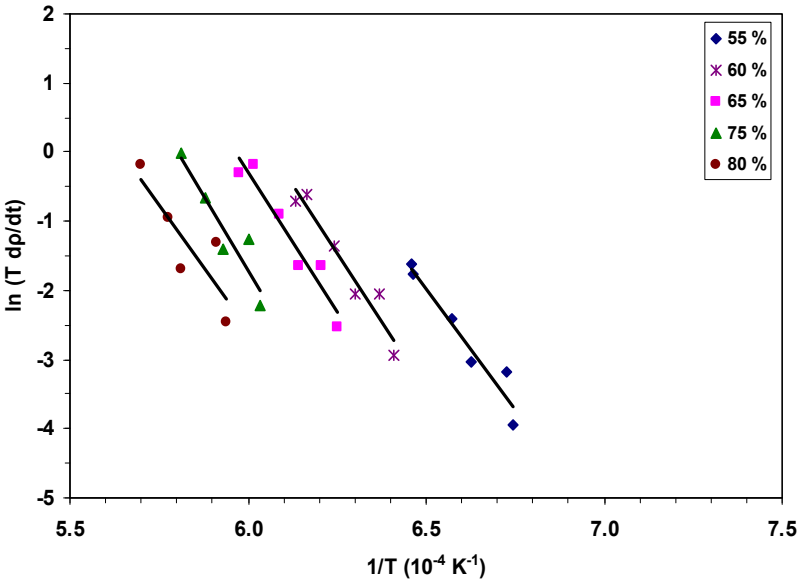

Figure 3-19: Arrhenius type plots for the densification rate, dρ/dt, at constant ρ values, for ST 1.02 composition.

Table 3-3: Activation energies for all the compositions at several relative densities.

Sr / Ti	Q_d (kJ/mol)						
	$\rho = 0.55$	$\rho = 0.60$	$\rho = 0.65$	$\rho = 0.75$	$\rho = 0.80$	$\rho = 0.85$	$\rho = 0.90$
0.997	705	617	666	842	980	1531	-
0.999	620	614	693	924	1007	1145	1167
1	555	526	521	558	584	848	915
1.02	584	657	681	709	608	-	-

The average values of Q_d in Table 3-3 up to ρ = 0.65, within the regimen I (see Figure 3-15), for the Ti rich compositions do not present very significant differences, taking into account the associated experimental error: Q_d = 663 ± 46 kJ/mol for ST 0.997, Q_d = 642 ± 57 kJ/mol for ST 0.999, which are very close to the Q_d value for the Sr rich one, Q_d = 641 ± 57 kJ/mol. A slightly lower value was determined for the stoichiometric composition, Q_d = 534 ± 21 kJ/mol. In regime II, higher apparent activation energy values are observed, up to 1531 kJ/mol for ST 0.997, 1167 kJ/mol for ST 0.999 and 915 kJ/mol for ST. The ST 1.02 composition present only one regimen and accordingly the obtained apparent activation energy values do not show significant variations.

3.2.2.2 Sintering exponents

The representation of *ln y* vs. *ln c* at constant *T* in Figures 3-20 to 3-23 leads to the calculation of the sintering exponent, *s*, according to equation (3-4), valid for the initial stage [127]. The sintering exponent, *s*, is equal to 2 for lattice diffusion and to 3 for grain boundary diffusion. Considering equation (3-4) the plots of *ln y* versus *ln c* at constant temperatures (Figures 3-20 to 3-23) lead to a slope equal to *(- 1/s)*. The resulting sintering exponents for two temperatures for each composition are presented in Table 3-4.

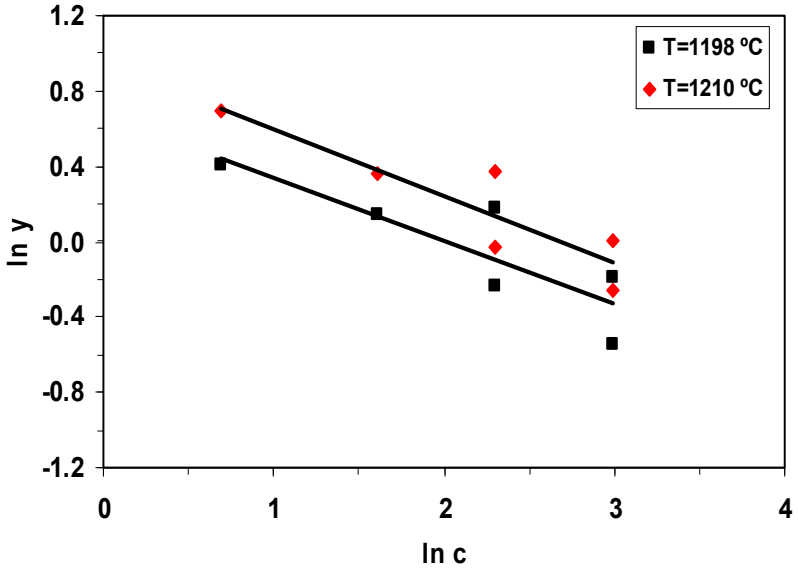

Figure 3-20: Linear shrinkage at constant temperature as a function of heating rate for ST 0.997 composition.

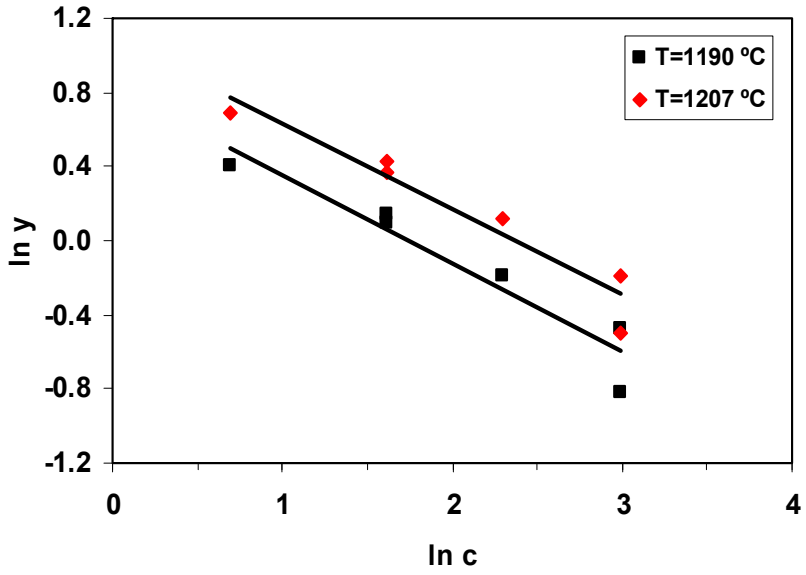

Figure 3-21: Linear shrinkage at constant temperature as a function of heating rate for ST 0.999 composition.

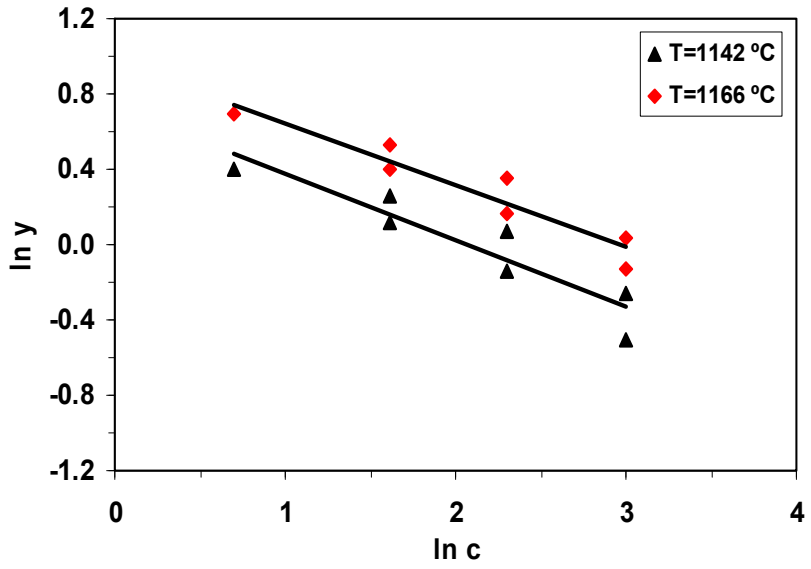

Figure 3-22: Linear shrinkage at constant temperature as a function of heating rate for ST composition.

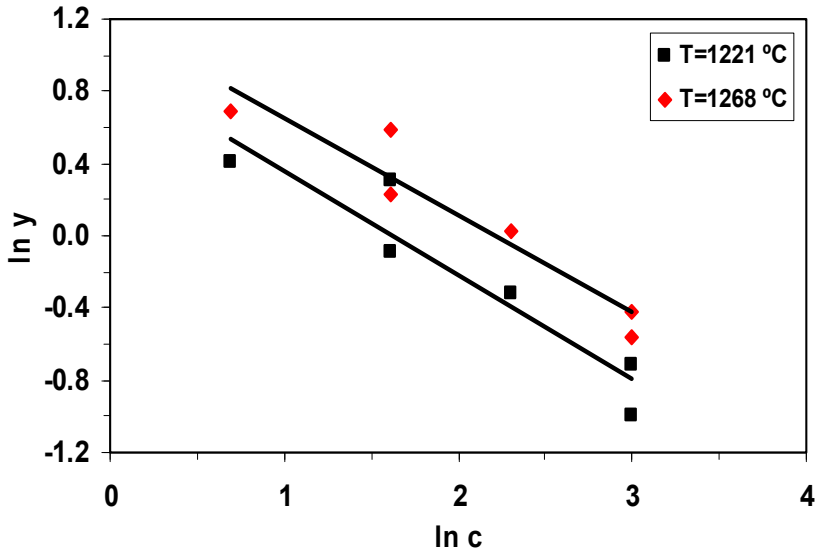

Figure 3-23: Linear shrinkage at constant temperature as a function of heating rate for ST 1.02 composition.

The limited range of application of equation (3-4) into the initial stage values ($y \leq 2\%$) together with the frequently observed initial instability of the shrinkage curves (chemical and physical surface phenomena interference and the multiplicity of mass transport mechanisms that could be more active) [128] may lead to low linear correlation coefficients in the representations of the experimental values. This is the case of ST 0.997 (Figure 3-20) or even ST (Figure 3-22). As a consequence, the uncertainty in the *s* values is high and, therefore, another relation (equation (3-5) [127]) was also used to calculate the sintering exponents. In accordance with equation (3-5), the representation of *ln (dy/dt)* versus *ln y* (Figures 3-24 to 3-27) at constant temperatures is linear and the slope is equal to *(1 - s)*. The *s* exponent can then be easily obtained. The results are presented in Table 3-4.

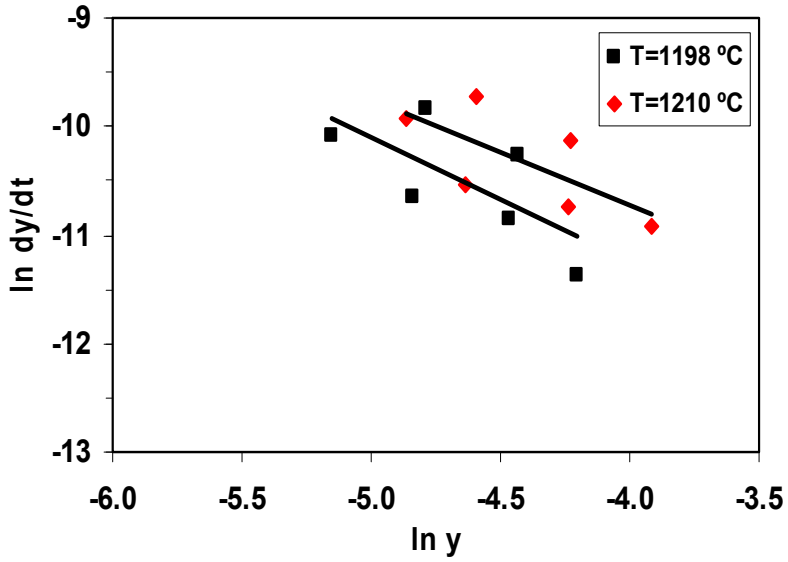

Figure 3-24: Linear shrinkage rate, dy/dt, as a function of linear shrinkage, y, at constant temperature, for ST 0.997 composition.

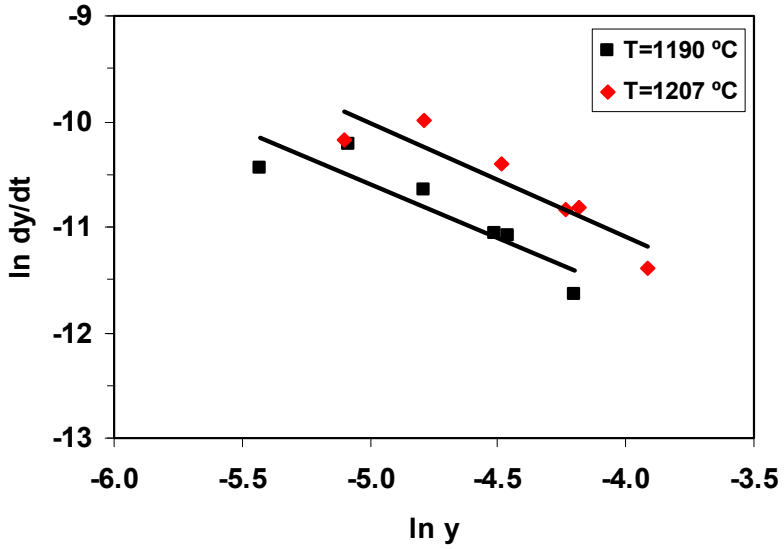

Figure 3-25: Linear shrinkage rate, dy/dt, as a function of linear shrinkage, y, at constant temperature, for ST 0.999 composition.

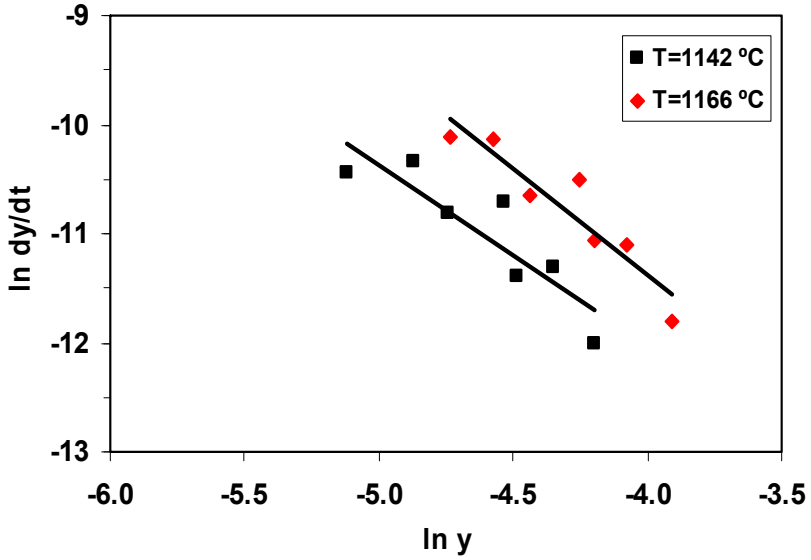

Figure 3-26: Linear shrinkage rate, dy/dt, as a function of linear shrinkage, y, at constant temperature, for ST composition.

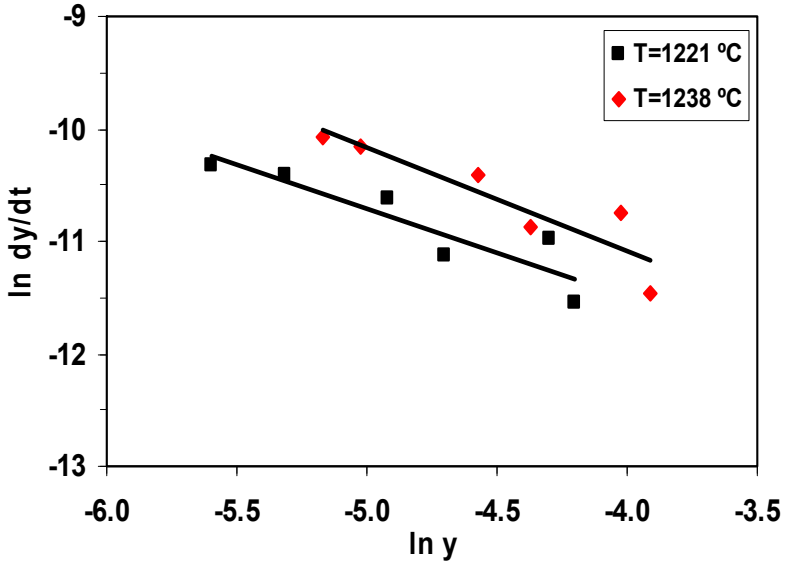

Figure 3-27: Linear shrinkage rate, dy/dt, as a function of linear shrinkage, y, at constant temperature, for ST 1.02 composition.

Table 3-4: Calculated sintering kinetic exponents.

	Equation (3-4)		**Equation** (3-5)	
Sr / Ti	T_1	T_2	T_1	T_2
	Sintering exponent, ***s***			
0.997	3	3	2	2
0.999	2	2	2	2
1	3	3	3	3
1.02	2	2	2	2

The exponent s is characteristic of the densification mechanism and the values presented in Table 3-4 were calculated for two different temperatures (T_1 and T_2) corresponding to microstructure evolutions in the compacts essentially limited to the initial stage ($y \leq 2\%$). The calculated values for the different compositions are inside the range of the

values predicted by the model and may be identified with a densification process governed by the mass transport either by volume (s = 2) or by grain boundary diffusion (s = 3). A volume diffusion mechanism seems to effectively control the shrinkage in the initial sintering stage of the ST 1.02 and ST 0.999 compacts. Moreover, the grain boundary transport is also suggested to contribute to the shrinkage, being more relevant in the stoichiometric ST composition and, accordingly, the apparent activation energy for densification, Q_d, in Table 3-3, was depressed.

3.3 Structural and elemental characterization of sintered compacts

The XRD profiles of samples after sintering up to 1500 ºC at 5 ºC/min in the dilatometer are depicted in Figure 3-28. Identical spectra were obtained for the sintered samples when compared with the powders spectra (Figure 3-1), showing the cubic symmetry for all the compositions and that samples are still monophasic after sintering.

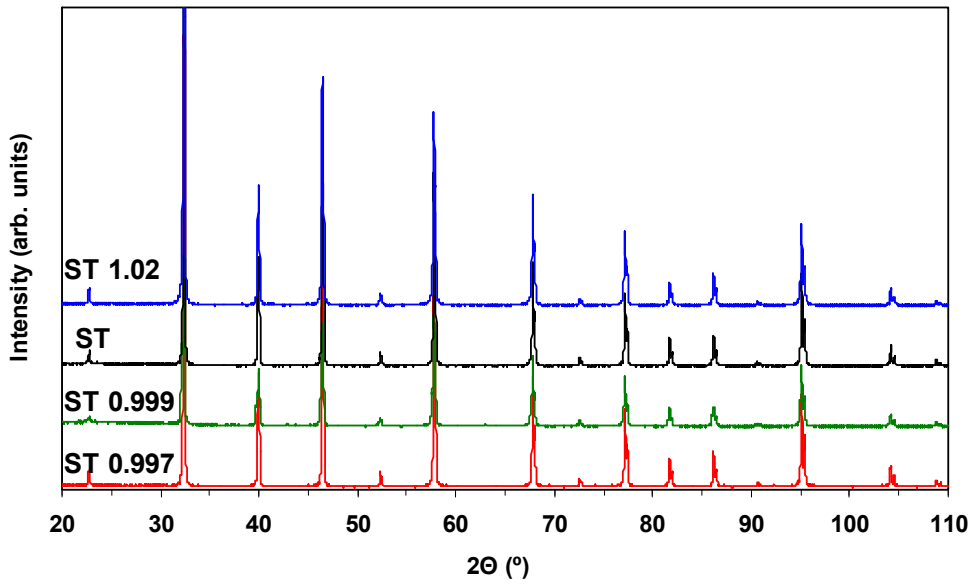

Figure 3-28: XRD spectra for all the compositions under study for samples heated at 5 ºC/min up to 1500 ºC.

From these curves the cell parameter, *a*, was calculated and is presented in Table 3-5 for three compositions. No result is presented for the cell parameter of ST 0.999 because a high error was found in the fitting regarding this composition. A slight decrease of the calculated cell parameter with the increase of the Sr/Ti ratio is noticeable. The obtained values are consistent with the reported lattice constant for ST of 3.905 Å [2, 34] and its variation with the Sr/Ti ratio is indicative of solid solution effects.

Table 3-5: Cell parameter, a, and the associated errors on fitting for ST 0.997, ST and ST1.02 compositions.

Sr / Ti	*a* (Å)	Error (Å)
0.997	3.90603	0.00004
1	3.90568	0.00008
1.02	3.90547	0.00007

X-ray mapping over several grains and grain boundaries have been performed for all the compositions by SEM/EDS. The results for Sr and Ti are presented in Figures 3-29 to 3-32 for all the compositions.

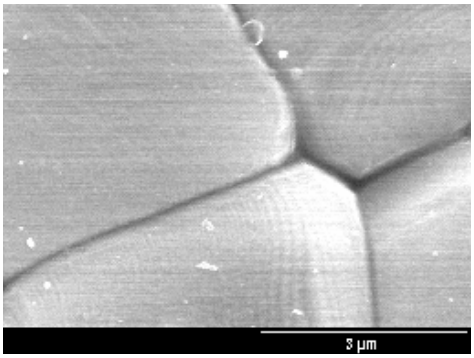

a) ST 0.997 (SEM)

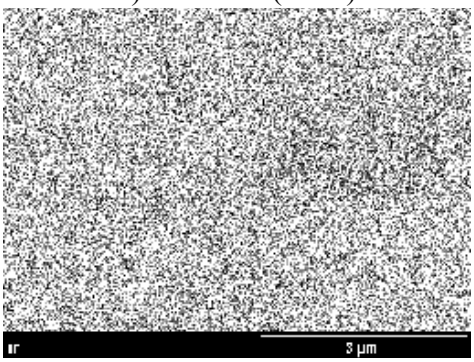

b) ST 0.997 – Sr map

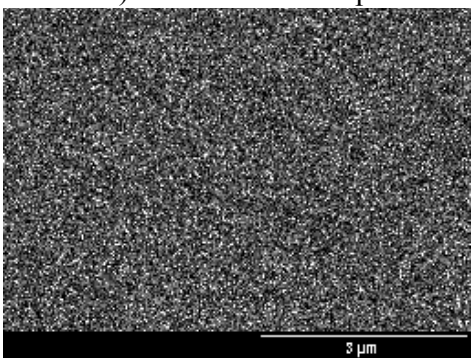

c) ST 0.997 – Ti map

Figure 3-29: X-ray maps for ST 0.997 composition.

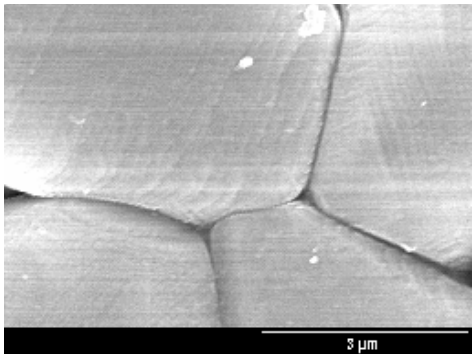

a) ST 0.999 (SEM)

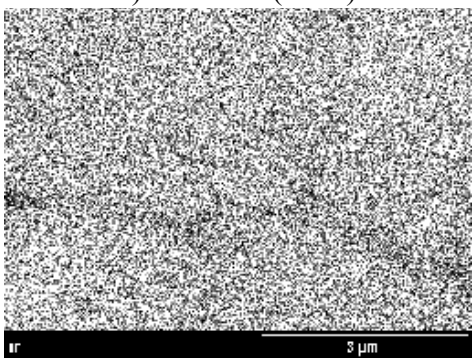

b) ST 0.999 – Sr map

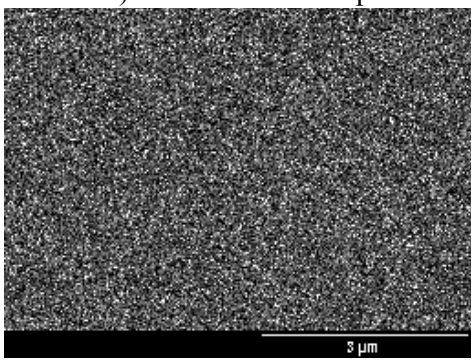

c) ST 0.999 – Ti map

Figure 3-30: X-ray maps for ST 0.999 composition.

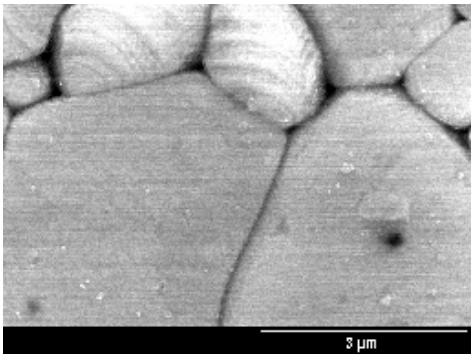

a) ST (SEM)

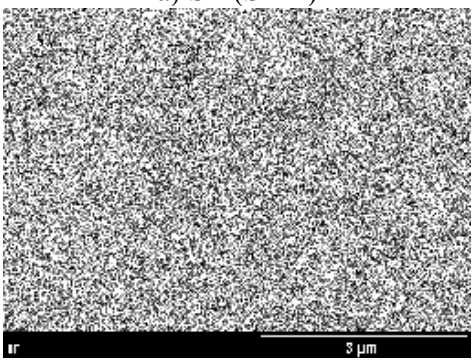

b) ST – Sr map

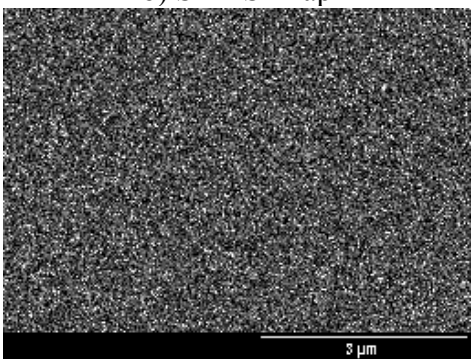

c) ST – Ti map

Figure 3-31: X-ray maps for ST composition.

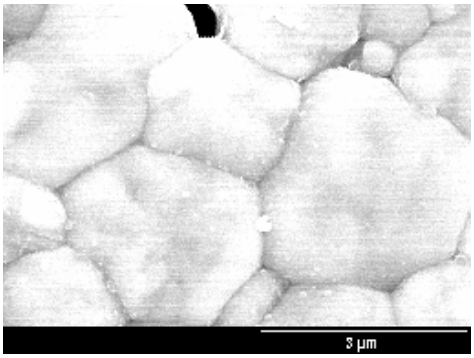

a) ST 1.02 (SEM)

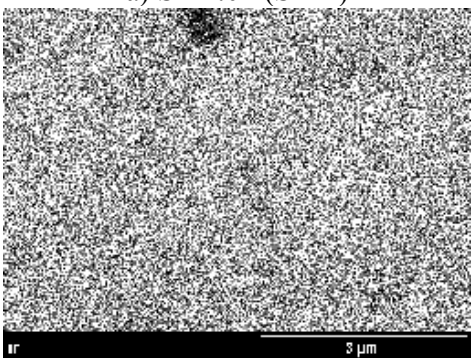

b) ST 1.02 – Sr map

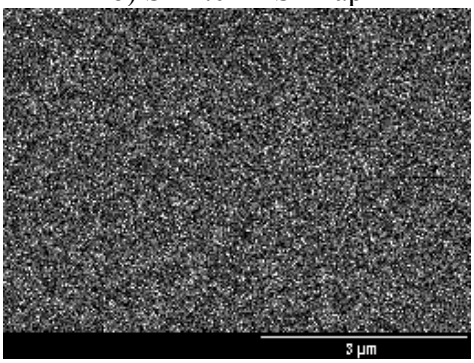

c) ST 1.02 – Ti map

Figure 3-32: X-ray maps for ST 1.02 composition.

The X-ray maps show that both elements are homogenously distributed over the grains for all compositions and no elemental segregation was detected. Topographic effects

associated with grain boundary regions may have caused some small variations within the X-ray maps.

3.4 Microstructural characterization of sintered compacts

The SEM microstructures of polished and thermally etched samples heated up to 1500ºC at 5ºC min^{-1} are depicted in Figure 3-33. The average grain sizes determined by SEM for all the compositions are presented in Figure 3-34.

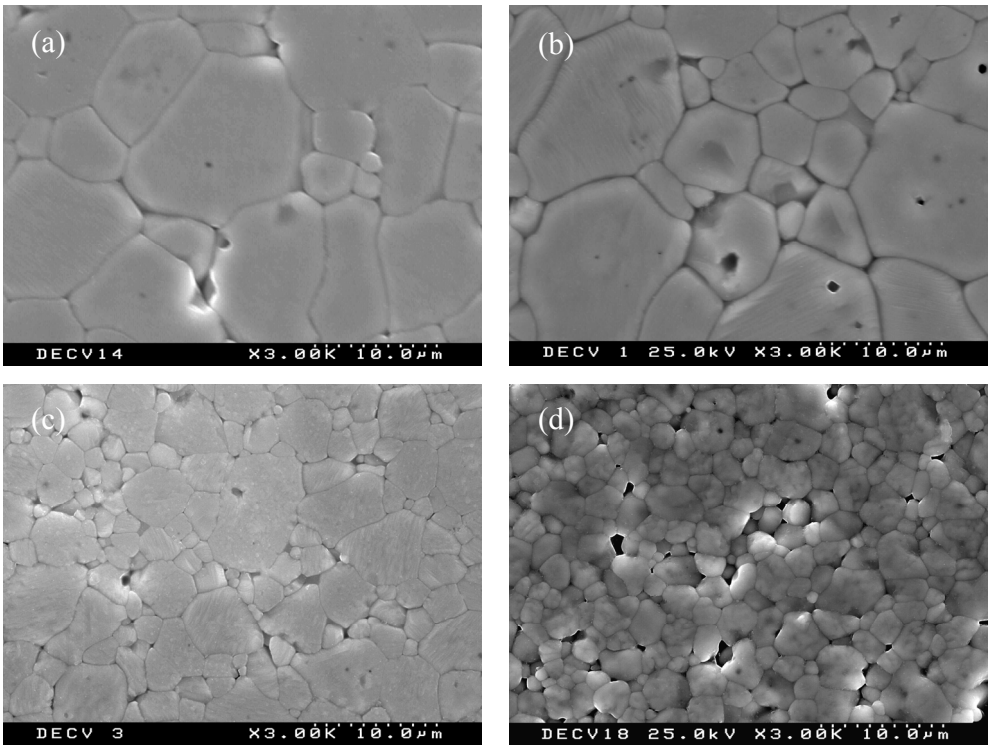

Figure 3-33: SEM microstructures of samples: (a) ST 0.997, (b) ST 0.999, (c) ST and (d) ST 1.02, heated at 5 ºC/min up to 1500 ºC.

The measured relative densities for those sintering conditions were 90, 95, 96 and 89% for ST 0.997, ST 0.999, ST and ST 1.02, respectively. Due to the small size of the samples used in the dilatometric analysis, the density measurement was not very precise and an experimental error not less than 2% must be considered. All the compositions show near equiaxied grains and no second phases were detected by XRD or SEM.

The GG is reduced with the increasing of Sr/Ti ratio in this composition range. The Ti rich samples, ST 0.997 and ST 0.999 (Figure 3-33 (a) and (b), respectively) clearly show coarse microstructures with abnormal grown grains, some intragranular porosity and average grain sizes of 6.1 μm for ST 0.997 and 6.3 μm for 0.999, as seen in Figure 3-34. The micrograph of ST (Figure 3-33 (c)) presents a finer microstructure than the previous ones with an average grain size of 4.1 μm, although large grains and some intragranular pores are still observed. For the Sr rich sample, ST 1.02 (Figure 3-33 (d)) the GG was effectively suppressed and a fine microstructure, G = 2.3 μm, is observed, without abnormal grains.

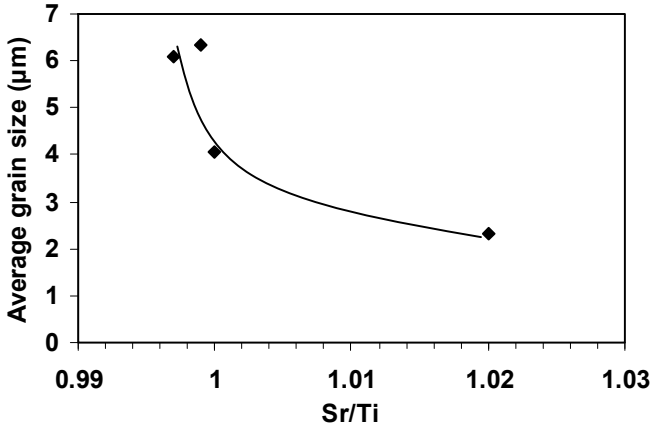

Figure 3-34: Average grain size as a function of the Sr/Ti ratio, for samples heated at 5 ºC/min up to 1500 ºC.

The characteristics of the microstructures described above are evidenced in Figure 3-35, in which the grain size distributions of the studied compositions are presented. It can be seen that Ti rich and stoichiometric compositions show enlarged grain size distributions and AGG whereas the Sr rich composition, ST 1.02, is characterized by a narrow grain size distribution and NGG. Although the relatively high porosity fraction of this sample, $P = 11 \pm 2\%$, could be pointed as responsible for the grain boundary pinning, equivalent amounts of porosity were determined in the sample ST 0.997, $P = 10 \pm 2\%$, without the observation of the correspondent pinning effect.

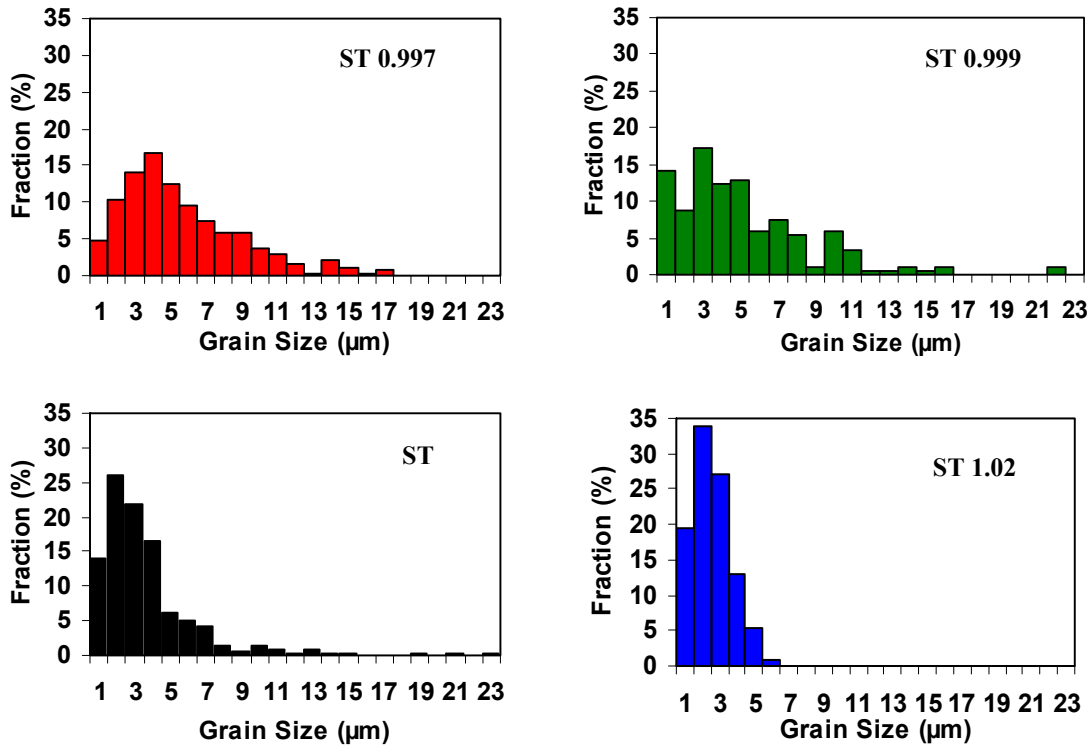

Figure 3-35: Grain size distribution for all the compositions under study, for samples heated at 5 ºC/min up to 1500 ºC.

TEM observations of fine sections of the samples ST 0.997, ST and ST 1.02 are shown in Figure 3-36. All samples present rough grain boundaries. Dark spots, probably precipitates, are often observed in and near the grain boundary region of ST 0.997, as seen in Figure 3-36

(a). In the stoichiometric sample, ST, no dislocations were observed (Figure 3-36 (c)). The Sr rich sample shows planar defects inside the grains (Figure 3-36 (d)), characteristic of the so-called RP structure [41].

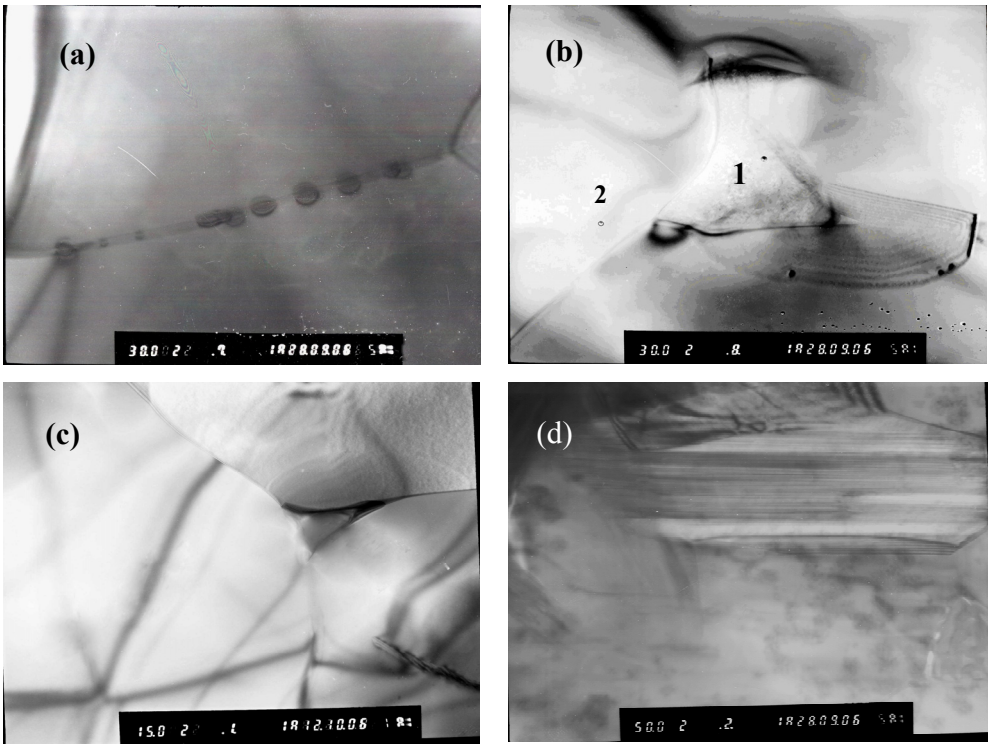

Figure 3-36: TEM microstructures of the samples: (a) and (b) ST 0.997, (c) ST and (d) ST 1.02. Image courtesy of Professor I. M. Reaney.

A few inclusions were observed in some triple points of the ST 0.997 and ST samples, as shown in Figure 3-36 (b) and (c). The EDS analysis performed in these inclusions revealed a Sr rich phase that occasionally contains Zr in its composition. EDS spectra of the ST 0.997 sample depicted in Figure 3-36 (b) are shown in Figure 3-37 and Figure 3-38. The EDS spectrum of Figure 3-37 corresponds to the inclusion in the triple point (location (1)) and the one of Figure 3-38 was performed in the neighbor grain (location (2)). The formation of Sr rich phases in the Ti rich and stoichiometric samples is not in agreement with the phase

equilibrium reported in the phase diagrams for the SrO – TiO_2 system presented in Figure 1-21. However, observations of SrO enriched phases on ST surfaces originated by surface restructuring at elevated temperatures and under oxidizing conditions have been reported [49, 72, 74]. Similar phenomena may be related with the formation of the observed Sr rich second phases. It is important to remark here that these inclusions were observed in just a few triple points, and so, their impact on the sintering behavior is considered to be of minor importance. In fact, the presence of a significant volume fraction of inclusions in the initial stage of sintering, where GG is not yet important, causes a reduction of the densification rate [124] and in this case, the inclusions were observed exactly in the compositions that showed enhanced sintering behavior.

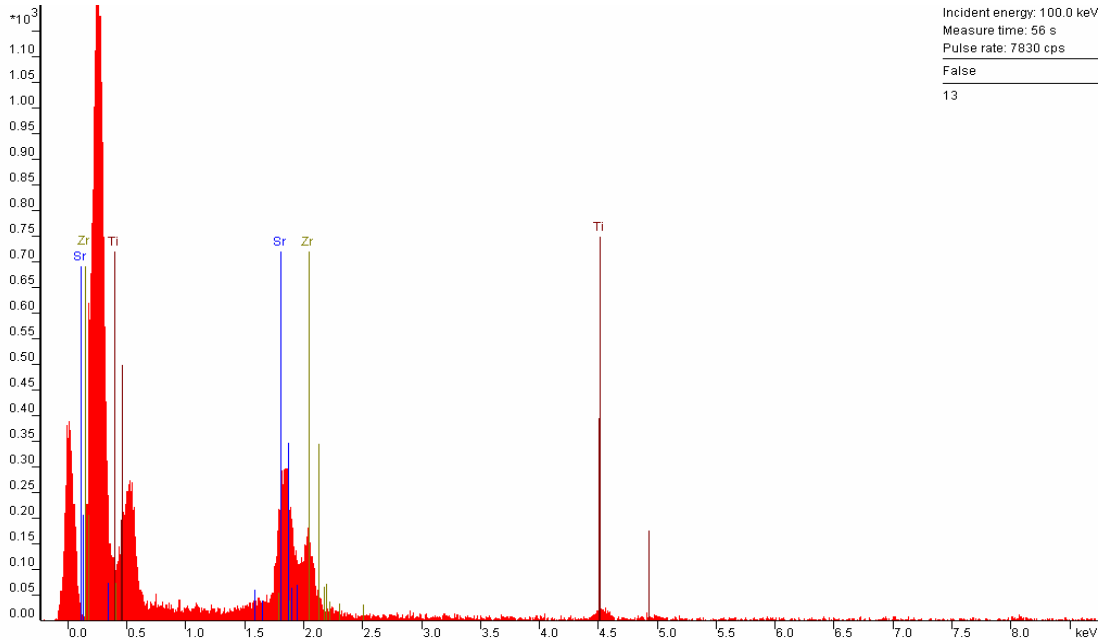

Figure 3-37: EDS spectrum of the triple point inclusion of ST 0.997 sample.

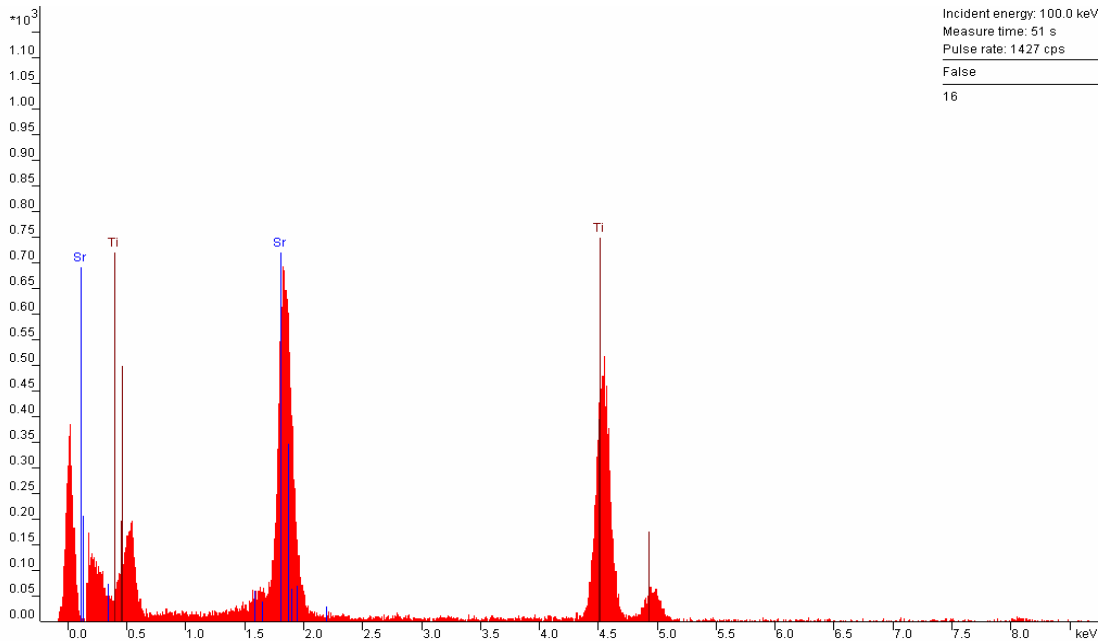

Figure 3-38: EDS spectrum of the grain of ST 0.997 sample, near the inclusion.

3.5 Grain growth studies

Considering the microstructures shown in Figure 3-33 and the grain size distributions presented in Figure 3-35, it is observed that the Ti rich and stoichiometric compositions present coarse microstructures with abnormal grown grains (AGG) giving rise to enlarged grain size distributions. On the other hand, Sr rich ST 1.02 composition presents a fine microstructure with a narrow grain size distribution and NGG. Bearing these observations in mind, the grain growth kinetics of strontium titanate were studied to confirm this effect in samples with longer sintering cycles, resulting in well developed microstructures. For this study, two compositions were selected: i) the stoichiometric, ST, showing AGG and ii) the Sr rich ST 1.02 that shows NGG.

The average grain size and relative density as a function of the sintering temperature for a sintering time of 2h, for ST and ST 1.02, are presented in Figure 3-39. Figure 3-40 shows

the average grain size and relative density for a sintering temperature of 1450 ºC as a function of the sintering time for the same compositions.

The samples presented close relative densities, around 94 ± 1%, with the exception of ST 1.02 sintered at 1400 ºC and 1450 ºC for 2 h, that attained lower densification, ρ = 91 and 92%, respectively. The fact that the porosity fraction is near equivalent in the samples under study discards the effect of significant differences in the driving force for GG coming from pore dragging. It is shown that the average grain size of ST is larger than that of ST 1.02 at every temperature, in the studied range (1400 – 1500 ºC).

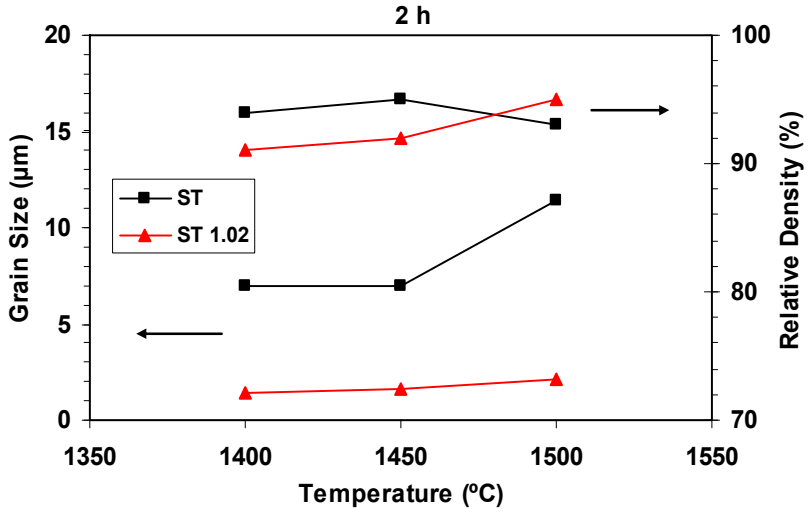

Figure 3-39: Average grain size and relative density as a function of sintering temperature for ST and ST 1.02 compositions.

However, the most important observation in this study is that the increase of the Sr content has a pronounced effect on the GG transport, decreasing it, evidenced by the average grain sizes for the two compositions, as was already observed in the microstructures in Figure 3-33.

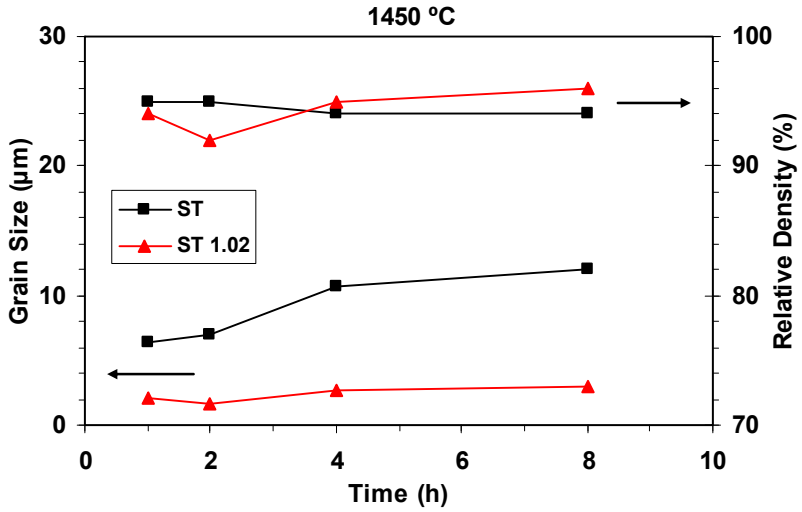

Figure 3-40: Average grain size and relative density as a function of sintering time for ST and ST 1.02 compositions.

SEM microstructures of ST and ST 1.02 samples sintered at 1450 ºC for 8h and at 1500 ºC for 2h are shown in Figure 3-41. The differences between the two compositions are again evident. For ST, coarse microstructures are observed as well as near equaxial grains with internal porosity, while ST 1.02 presents a fine microstructure with some elongated grains, probably due to grain boundary energy anisotropy related with the nonstoichiometry.

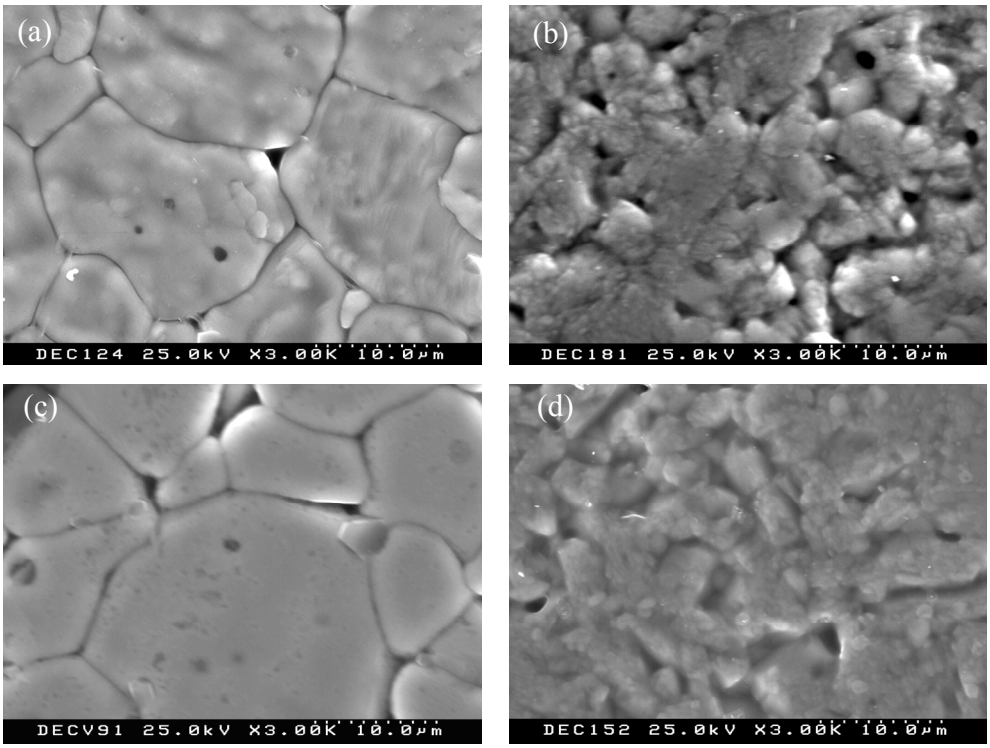

Figure 3-41: SEM microstructures for (a) ST and (b) ST 1.02 samples, sintered at 1450 ºC for 8h; (c) ST and (d) ST 1.02 samples, sintered at 1500 ºC for 2h.

GG kinetics can be described using the phenomenological kinetic GG equation [129-131] :

$$G^m - G_0^m = K_0 t \exp(-\frac{Q_g}{RT}) \qquad (3\text{-}6)$$

where G is the average grain size at the time t, G_0 is the initial grain size which is usually negligibly small, m is the kinetic GG exponent, K_0 is a pre-exponential constant, Q_g is the apparent activation energy for the GG process, R is the gas constant and T is the absolute temperature. According to equation (3-6), under isothermal conditions and neglecting G_0, the

m value can be determined from the slope of the *log (G)* versus *log (t)* plot (the slope is equal to *(1/m)*), presented in Figure 3-42.

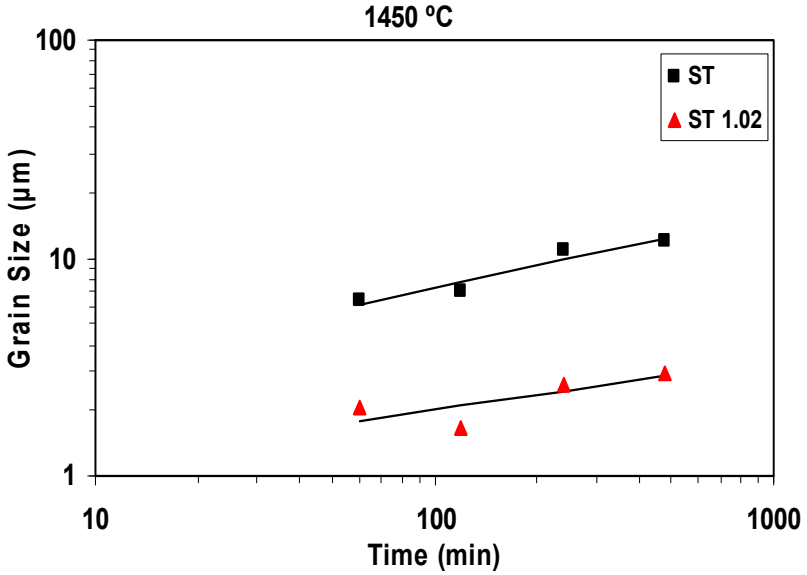

Figure 3-42: Average grain size as a function of the sintering time in log-log scale, for ST and ST 1.02.

Neglecting G_0, equation (3-6) can be expressed in the form [129-131]:

$$\log\left(\frac{G^m}{t}\right) = \log(K_0) - 0.434\left(\frac{Q_g}{RT}\right) \qquad (3\text{-}7)$$

and from equation (3-7), the slope of the plot of *log* (G^m/t) versus *1/T* yields the apparent activation energy for the GG process, Q_g. These plots are presented in Figure 3-43 for ST and ST 1.02 compositions. The kinetic GG exponents obtained from Figure 3-42 and the apparent activation energies obtained from Figure 3-43 are presented in Table 3-6.

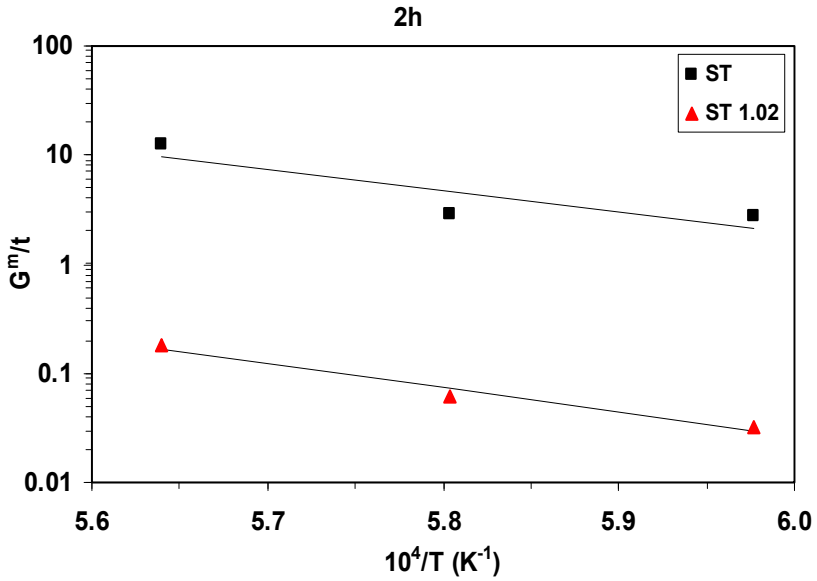

Figure 3-43: Arrhenius plots of log (G^m/t) versus 1/T for ST and ST 1.02.

Table 3-6: GG kinetic exponents and apparent activation energies for ST and ST 1.02 compositions.

Sr / Ti	GG exponent *m*	Activation energy Q_g (kJ/mol)
1	3	365
1.02	4	431

A higher *m* exponent and a small increase of the activation energy were determined for ST 1.02, comparatively to ST, as shown in Table 3-6. No second phases were detected in SEM observation of all the samples, which indicates as previously stated after XRD, SEM and TEM analysis of CHR sintered samples that solubilization of the excess Sr must be prevalent within the composition range used in this work. Therefore, the kinetic of GG show that, as observed

in the densification process, the excess Sr reduces the mass transport for the growth of grains due to solid solution effects. Both grain boundary or pore mobilities could be affected, resulting in the different kinetic laws determined in Table 3-6.

The effects of the stoichiometric deviations on the grain boundary structure and composition needs further investigation in forthcoming studies in order to better understand the relation between the Sr/Ti accommodation and the grain boundary movement.

4 Discussion

Several techniques were used for the powder characterization. In spite of the chemical composition variations, the powders of all the compositions used in this work revealed similar morphological characteristics: equivalent particle shape, particle size distribution and agglomeration degree. From these observations, the influence of the powder morphological characteristics was assumed to be equivalent in all the compositions under study and, hence, do not play a critical role in the densification and GG studies undertaken.

Contamination with Zr, from the used milling media, was present in all the powders in levels under 270 ppm. In addition, no second phases were observed by XRD for all compositions, either on the powders (Figure 3-1) or after the sintering step (Figure 3-28), although TEM observations (Figure 3-36) showed a Sr rich phase could be found in Ti rich and stoichiometric sintered samples. However, these precipitates are so scarce that they are hard to find.

The small excess of both TiO_2 and SrO used in the several compositions processed in this work seems to have been mostly incorporated into the perovskite lattice. In view of the point defect model, the incorporation of Sr excess requires the formation of interstitial strontium and oxygen ($Sr_i^{\bullet\bullet}$ and $O_i^{''}$) or titanium and oxygen vacancies ($V_{Ti}^{''''}$ and $V_O^{\bullet\bullet}$) [41]. Considering the difficulty in introducing large ions, such as Sr, into the interstitials of the close packed perovskite lattice [32] and the high charge of titanium vacancies [52], the incorporation of Sr excess would not be very favorable. However, the excess of Sr in the ST lattice fully accommodates as a three-dimensional mosaic of single-layered rock-salt blocks, forming the so-called RP structure [41, 56, 132], allowing the excess of SrO in the ST lattice. The presence of such interlayers, supposedly less polarizable than the perovskite lattice, seems to contribute to the decrease of the dielectric losses of Sr excess samples as observed in a previous work [1]. For the small excess of Sr used in this work, Sr/Ti ≤ 1.02, the structure is still cubic, as determined by XRD. However, planar defects probably related with the RP structure could be clearly observed by TEM (Figure 3-36 (d)). No second phases were

detected by SEM and TEM observations, suggesting the complete incorporation of the excess Sr.

On the other hand, neglecting interstitial occupation, the incorporation of Ti excess into the lattice requires the formation of Sr and oxygen vacancies [41, 114, 132]. Oxygen vacancies are known to be easily formed in perovskite compounds [41, 71] and strontium vacancies are often assumed to be the most important compensation mechanism in ST [45, 49, 50, 59, 87, 119]. This is even corroborated by theoretical calculations within the ST defect model [50] that indicate that vacancy disorder is predominant in this material, with a small tendency for development of Sr deficiency at higher temperatures.

Therefore, some solubility is expected, despite the fact that the phase diagrams (Figure 1-21) for this system do not show any solid solution region for Ti excess. In addition, Ti rich second phases were reported for compositions with Sr/Ti ratios lower than 0.995 [114]. In the present work, the TiO_2 excess used was lower ($Sr/Ti \geq 0.997$) and, accordingly, no Ti rich second phases were found in the Ti excess compositions. Moreover, if the excess of Ti was not largely accommodated in the perovskite structure, forming disperse second phase particles, a retardation effect should be expected for the densification and GG caused by the pinning of free surfaces and grain boundaries [129, 131]. Therefore, the fact that the densification is enhanced with the increasing of Ti content, from the early beginning of sintering and at temperatures where a liquid phase is not expected (the eutectic point for Ti rich compositions is at 1440ºC) strongly suggests that some solubility really occurred. Another indication of solid solubility effect is the variation of the lattice parameter with the variation of the Sr/Ti ratio showing an increase for Ti excess and a decrease for Sr excess.

The Sr rich phases observed by TEM in the stoichiometric and Ti rich compositions, although scarce, may argue in favor of the formation of Sr vacancies as compensating defects for the accommodation of Ti excess in the perovskite lattice. In fact, observations of SrO enriched phases on ST surfaces were reported [49, 72, 74]. The formation of Sr vacancies, as compensating point defects upon donor doping under oxidizing conditions, was reported to be accompanied by a release of strontium from its regular site and its accumulation at the surface as precipitates of SrO_x composition [49]. Sr rich second phases were also reported by You et

al. [119] attributed to the migration of Sr ions from the lattice to the grain boundaries leaving compensating vacancies in the ST lattice, upon doping with WO_3.

However, the hypothesis of a partial solubilization of Ti leaving yet a fraction of the excess Ti on the surfaces or segregation of Ti in the grain boundaries forming a Ti rich layer, as observed in TiO_2-excess BT [85, 95] and ST [92], cannot be ignored. Ti segregation to the grain boundaries in BT and ST is known [61, 71] and a space charge layer model was suggested [61, 62, 65, 67]. The presented X-ray maps and the EDS analysis in TEM micrographs showed no segregation to the grain boundaries in the sintered samples but further investigation is needed, with careful observation of the grain boundaries and surfaces in sintered and partially sintered samples using more powerful characterization techniques such as Electron Energy Loss Spectroscopy (EELS) and Atomic Force Microscopy (AFM).

The diffusion of cation vacancies is known to be much slower than that of oxygen vacancies in titanate materials [88] and, so, the matter transport for sintering of these materials is assumed to be rate controlled by the diffusion of the first species [50, 112]. Although some controversy exists about the relative diffusivity of the cations occupying A and B sites, sintering studies identify the A site ions as the rate limiting species [83, 133].

It is pointed from the presented results, regarding densification (Figures 3-14 and 3-15) and GG (Figures 3-39 and 3-40), that Ti excess enhanced the matter transport whereas Sr excess decreased it. The close values of the activation energy determined for the initial densification, $534 \leq Q_d \leq 663$ kJmol^{-1}, in Table 3-3, and the onset of densification at a near constant temperature, T ≈ 1100ºC for all the compositions under study strongly suggest that the same mechanism of transport controls the densification of all the compositions. Assuming that the diffusion of Sr via a vacancy mechanism, either through the bulk or through the grain boundaries paths, is controlling the matter transport for sintering, the increase of Ti concentration will increase the concentration of these species leading to the increase of the respective diffusion coefficient. Consequently, increased densification rates and grain sizes were obtained for Ti rich compositions. On the other hand, Sr excess will reduce the Sr vacancy concentration and, thus, decrease the matter transport for sintering, resulting in lower densification rates and smaller grain sizes for Sr rich composition than for stoichiometric and Ti rich compositions.

However, the obtained values for the activation energies (Table 3-3) are higher than those reported in the literature for the diffusion activation energy of Sr in strontium titanate, presented in Table 4-1, matching apparently better to the values for Ti diffusion. Besides the scattering of the values in Table 4-1, generally observed for the diffusion data and difficulting the comparison between different experiments [134], higher values for the apparent activation energy from sintering experiments than those related with the respective diffusion species are commonly found. This fact is due to the interference of other processes such as solubilization of impurities, multiple diffusion paths or even the insufficiency of the sintering models to account for the complexity of real systems [83, 128, 135, 136]. Therefore, the scenario of a sintering kinetics controlled by the diffusion of the Sr vacancies is a very probable one, for the compositions under study. Concerning the main diffusion path for sintering transport, the kinetic analysis of the initial stage (Table 3-4) pointed to volume diffusion mechanism with a contribution of grain boundary transport depending on the stoichiometry.

The second regimen of shrinkage rate found in the Ti rich and stoichiometric samples (Figure 3-15) appears at temperatures between 1330ºC - 1440ºC, depending on the composition, and shows high values of the activation energies, as shown in Table 3-3. This change of the activation energy could be associated with a change of the diffusion path or diffusion species or even with chemical effects, like solubilization. It must be also pointed here that although the appearance of a liquid phase at temperatures lower than 1440ºC is not expected, based on the phase diagrams in Figure 1-21, this effect cannot be completely ruled out. The presence of some impurities may decrease the eutectic temperature [83, 93, 96]. In addition, the presence of a liquid phase in the surface of ST during annealing at 1100 ºC, related with restructure in the near surface region, has been reported [74]. Similar phenomena may be somehow associated with the origin of the peaks (Figure 3-15) in the Ti excess compositions. However, the abrupt increase of the densification rate and the subsequent enlargement of the apparent activation energies are not enough to identify the causes of such effects. Further investigation, with special focus on the microstructure development during sintering with local chemical and structural analysis, using SEM and TEM microscopy techniques, are required.

Table 4-1: Activation energy values of diffusion coefficients reported for strontium titanate.

Diffusion element	Q (kJ/mol)	Temperature range (K)	Method	Reference
O	65 - 123	1098-1798	Gas-solid isotope exchange (S)	[137]
	95	1333-1673	Isotope exchange(S)	[138]
	67	1333-1573	Isotope exchange (P)	
Sr	292	1273-1573	Radiotracer experiments (P)	[139]
	243	--	Theoretical calculation (vacancy diffusion)	[50]
	475	2148	Not specified	[140]
Ti	1118	--	Theoretical calculation (vacancy diffusion)	[50]
	475	2148	Not specified	[140]

S-single crystal; P-polycrystalline material

The activation energy values determined for GG (Table 3-6) are comparable to the values reported for Sr diffusion. However, in the case of GG process the variety of mass transport mechanisms controlling GG and the large sensitivity of the grain boundary chemistry and structure to compositional variations make difficult the direct correlation of the apparent activation energy values presented in Table 3-6 with specific diffusion paths.

Although at a first glance the observed effect of the nonstoichiometry on the sintering kinetics of ST could be explained by the related change of the equilibrium defects, affecting the diffusion transport, other aspects need to be investigated. Special attention is required to the structural and chemical characterization of surfaces and interfaces, looking for segregation

effects, eventual solid or liquid second phases, preferential grain boundary orientation and structure of normal and abnormal grains, among other aspects. As have been said, these aspects were recently found to be determinant on the densification and GG of BT. In addition, electrical characterization of samples of all the compositions under study is ongoing, namely, impedance spectroscopy studies. These studies, although very preliminary and therefore not presented in this thesis, suggest that the nonstoichiometry has a significant influence on the characteristics of the grain boundaries of ST. Further attention will also be devoted to the influence of nonstoichiometry on the dielectric response of the material.

5 Conclusions and future work

A systematic study on the effect of the nonstoichiometry on the mass transport during sintering of ST ceramics, both on densification and GG processes was undertaken. Compositions with Sr/Ti ratios from 0.997 to 1.02 were prepared by the mixed oxide method.

In spite of the stoichiometry variations, the powders of all the compositions revealed similar morphological characteristics: equivalent particle shape, particle size distribution and agglomeration degree. The small excess of both TiO_2 and SrO used in the several compositions during this investigation seems to have been mostly incorporated into the perovskite lattice. XRD revealed no second phases for all compositions. The analysis of sintered samples by SEM observation also revealed no second phases and a systematic variation of the lattice parameter with Sr/Ti ratio was detected, showing that solid solution effects must be considered.

Ti excess enhanced the matter transport during sintering whereas Sr excess decreased it. An increase on the shrinkage rate and average grain size originating coarse microstructures was observed with the decrease of the Sr/Ti ratio. The close values of the activation energy determined for the initial densification, $534 \leq Q_d \leq 663$ kJmol^{-1}, and the onset of densification at a near constant temperature, strongly suggest that the same mechanism of transport controls the densification of all the compositions. Concerning the main diffusion path for sintering transport, the calculated sintering exponents in the kinetic analysis of the initial stage suggest a volume diffusion mechanism with a contribution of grain boundary transport depending on the stoichiometry.

Regarding GG studies in well-developed microstructures, the average grain size of ST samples was again observed to be higher than the one of samples of Sr rich composition. A higher GG exponent (m = 3 and 4, for ST and ST 1.02, respectively) and a small increase of the activation energy were determined for ST 1.02, comparatively to ST. The activation energy values determined for GG were 365 and 431 kJ/mol for ST and ST 1.02, respectively.

The obtained results are coherent with a mass transport during sintering controlled by Sr vacancies and altered by the accommodation of Ti or Sr excess in the perovskite structure, inducing alterations in the defect chemistry of the material.

In summary, it can be concluded that very small stoichiometric variations affect markedly the microstructure evolution of ST ceramics. Decreasing the Sr content significantly increases the matter transport for both densification and GG leading to coarser microstructures with AGG. The results suggest that nonstoichiometry induces alterations of the defect equilibrium of the material and that Sr vacancies are the rate limiting species in the matter transport during sintering. Very small stoichiometric variations may be used to engineer the microstructure of the ceramic and, therefore, to tailor its properties, namely, the dielectric response.

As said in the last section of this text, several aspects of this work need further investigation and development. Detailed microstructure studies using SEM and TEM microscopy techniques are required, with special attention paid to the chemical and structural characterization of grain boundaries and surfaces in sintered and partially sintered samples. The hypothesis of segregation to the grain boundaries and its relation with nonstoichiometry need to be further investigated. The presence of Sr rich second phases also requires clarification. Powerful characterization techniques, such as EELS and AFM, are necessary in order to obtain detailed information about these issues.

The kinetic studies regarding densification presented in this text are restricted to the initial sintering stage. Kinetic analysis will also be performed regarding the intermediate and final sintering stages. These studies may help to explain the appearance of the two peaks in the shrinkage rate on the stoichiometric and Ti rich compositions.

Impedance spectroscopy studies, now ongoing, may contribute to clarify the influence of nonstoichiometry on the grain boundaries and the consequent differences in the dielectric response. Dielectric tunability studies will also be undertaken and a correlation of the influence of nonstoichiometry on the dielectric response of the material with its defect chemistry will be attempted. The effect of nonstoichiometry on the sintering behavior and on the dielectric properties of ST will also be studied on thick films.

References

1. Tkach, A., Vilarinho, P.M., Senos, A.M.R. and Kholkin, A.L., *Effect of nonstoichiometry on the microstructure and dielectric properties of strontium titanate ceramics.* Journal of the European Ceramic Society, 2005. **25**(12): p. 2769.
2. Bhalla, A.S., Guo, R.Y. and Roy, R., *The perovskite structure - a review of its role in ceramic science and technology.* Materials Research Innovations, 2000. **4**(1): p. 3.
3. Haertling, G.H., *Ferroelectric ceramics: history and technology.* Journal of the American Ceramic Society, 1999. **82**(4): p. 797.
4. Setter, N., *Electroceramics: Looking ahead.* Journal of the European Ceramic Society, 2001. **21**(10-11): p. 1279.
5. Muller, K.A. and Burkard, H., *$SrTiO_3$ - an intrinsic quantum paraelectric below 4K.* Physical Review B, 1979. **19**(7): p. 3593.
6. Lytle, F.W., *X-Ray diffractometry of low-temperature phase transformations in strontium titanate.* Journal of Applied Physics, 1964. **35**(7): p. 2212.
7. Frederikse, H.P.R., Thurber, W.R. and Hosler W.R., *Electronic transport in strontium titanate.* Physical Review A-General Physics, 1964. **134**(2A): p. A442.
8. Schooley, J.F., Hosler, W.R. and Cohen, M.L., *Superconductivity in semiconducting $SrTiO_3$.* Physical Review Letters, 1964. **12**(17): p. 474.
9. Kotecki, D.E., Baniecki, J.D., Shen, H., Laibowitz, R.B., Saenger, K.L., Lian, J.J., Shaw, T.M., Athavale, S.D., Cabral, C., Duncombe, P.R., Gutsche, M., Kunkel, G., Park, Y.J., Wang, Y.Y., and Wise, R., *$(Ba,Sr)TiO_3$ dielectrics for future stacked-capacitor DRAM.* Ibm Journal of Research and Development, 1999. **43**(3): p. 367.
10. Zhou, C. and Newns, D.M., *Intrinsic dead layer effect and the performance of ferroelectric thin film capacitors.* Journal of Applied Physics, 1997. **82**(6): p. 3081.
11. Eisenbeiser, K., Finder, J.M., Yu, Z., Ramdani, J., Curless, J.A., Hallmark, J.A., Droopad, R., Ooms, W.J., Salem, L., Bradshaw, S., and Overgaard, C.D., *Field effect*

transistors with $SrTiO_3$ gate dielectric on Si. Applied Physics Letters, 2000. **76**(10): p. 1324.

12. Grossmann, M., Slowak, R., Hoffmann, S., John, H., and Waser, R., *A novel integrated thin film capacitor realized by a multilayer ceramic-electrode sandwich structure.* Journal of the European Ceramic Society, 1999. **19**(6-7): p. 1413.
13. Li, J.Y., Luo, S.H., and Alim, M.A., *The role of TiO_2 powder on the $SrTiO_3$-based synthesized varistor materials.* Materials Letters, 2006. **60**(6): p. 720.
14. Li, J.Y., S.T. Li, and Alim, M.A., *The effect of reducing atmosphere on the SrTiO3 based varistor-capacitor materials.* Journal of Materials Science-Materials in Electronics, 2006. **17**(7): p. 503.
15. Meyer, R. and Waser, R., *Resistive donor-doped $SrTiO_3$ sensors: I, basic model for a fast sensor response.* Sensors and Actuators B-Chemical, 2004. **101**(3): p. 335.
16. Kolodiazhnyi, T. and Petric, A., *The applicability of Sr-deficient n-type $SrTiO_3$ for SOFC anodes.* Journal of Electroceramics, 2005. **15**(1): p. 5.
17. Bouzehouane, K., Woodall, P., Marcilhac, B., Khodan, A.N., Crete, D., Jacquet, E., Mage, J.C., and Contour, J.P., *Enhanced dielectric properties of $SrTiO_3$ epitaxial thin film for tunable microwave devices.* Applied Physics Letters, 2002. **80**(1): p. 109.
18. Li, H.C., Si, W.D., West, A.D., and Xi, X.X., *Thickness dependence of dielectric loss in $SrTiO_3$ thin films.* Applied Physics Letters, 1998. **73**(4): p. 464.
19. Vendik, O.G., Hollmann, E.K., Kozyrev, A.B., and Prudan, A.M., *Ferroelectric tuning of planar and bulk microwave devices.* Journal of Superconductivity, 1999. **12**(2): p. 325.
20. Tagantsev, A.K., Sherman, V.O., Astafiev, K.F., Venkatesh, J., and Setter, N., *Ferroelectric materials for microwave tunable applications.* Journal of Electroceramics, 2003. **11**(1-2): p. 5.
21. Tkach, A., Vilarinho, P.M., and Kholkin, A.L., *Structure-microstructure-dielectric tunability relationship in Mn-doped strontium titanate ceramics.* Acta Materialia, 2005. **53**(19): p. 5061.
22. Tkach, A., *Strontium titanate based ceramics for tunable device applications*. 2005, Ph. D. Thesis, University of Aveiro, Aveiro.

23. Lines, M.E. and Glass, A.M., *Principles and applications of ferroelectric and related materials*. 1977, Oxford: Clarendon Press.
24. Saifi, M.A. and Cross, L.E., *Dielectric properties of strontium titanate at low temperature.* Physical Review B, 1970. **2**(3): p. 677.
25. Lemanov, V.V., Smirnova, E.P., Syrnikov, P.P., and Tarakanov, E.A., *Phase transitions and glasslike behavior in $Sr_{1-x}Ba_xTiO_3$.* Physical Review B, 1996. **54**(5): p. 3151.
26. Kan, D., Terashima, T., Kanda, R., Masuno, A., Tanaka, K., Chu, S., Kan, H., Ishizumi, A., Kanemitsu, Y., Shimakawa, Y., and Takano, M., *Blue-light emission at room temperature from Ar^+-irradiated $SrTiO_3$.* Nature Materials, 2005. **4**: p. 816.
27. Szot, K., Speier, W., Bihlmayer, G., and Waser, R., *Switching the electrical resistance of individual dislocations in single-crystalline $SrTiO_3$.* Nature Materials, 2006. **5**(4): p. 312.
28. Kingon, A., *Perovskites: Is the ultimate memory in sight?* Nature Materials, 2006. **5**(4): p. 251.
29. Lee, S.B., Lee, J.H., Cho, P.S., Kim, D.Y., Sigle, W., and Phillipp, F., *High-temperature resistance anomaly at a strontium titanate grain boundary and its correlation with the grain-boundary faceting-defaceting transition.* Advanced Materials, 2007. **19**(3): p. 391.
30. Last, J.T., *Infrared-absorption studies on barium titanate and related materials.* Physical Review, 1957. **105**(6): p. 1740.
31. Choi, G.M., Tuller, H.L., and Goldschmidt, D., *Electronic transport behavior in single-crystalline $Ba_{0.03}Sr_{0.97}TiO_3$.* Physical Review B, 1986. **34**(10): p. 6972.
32. Itoh, M., Wang, R., Inaguma, Y., Yamaguchi, T., Shan, Y.J., and Nakamura, T., *Ferroelectricity induced by oxygen isotope exchange in strontium titanate perovskite.* Physical Review Letters, 1999. **82**(17): p. 3540.
33. Mishra, S.K., Ranjan, R., Pandey, D., and Kennedy, B.J., *Powder neutron diffraction study of the antiferroelectric phase transition in $Sr_{0.75}Ca_{0.25}TiO_3$.* Journal of Applied Physics, 2002. **91**(7): p. 4447.

34. Mitsui, T., and Westphal, W.B., *Dielectric and X-ray studies of $Ca_xBa_{1-x}TiO_3$ and $Ca_xSr_{1-x}TiO_3$.* Physical Review, 1961. **1**(5): p. 1354.
35. Rimai, L., and Demars, G.A., *Electron paramagnetic resonance of trivalent gadolinium ions in strontium and barium titanates.* Physical Review, 1962. **127**(3): p. 702.
36. Unoki, H., and Sakudo, T., *Electron spin resonance of Fe^{3+} in $SrTiO_3$ with special reference to 110 K phase transition.* Journal of the Physical Society of Japan, 1967. **23**(3): p. 546.
37. Seuter, A.M.J., *Defect chemistry and electrical transport properties of barium titanate.* Philips Research Reports, 1974: p. 1.
38. Aggarwal, S., and Ramesh, R., *Point defect chemistry of metal oxide heterostructures.* Annual Review of Materials Science, 1998. **28**: p. 463.
39. Smyth, D.M., *The defect chemistry of metal oxides*. 2000, New York: Oxford University Press, Inc.
40. Ohly, C., *Nanocrystalline alkaline earth titanates and their electrical conductivity characteristics under changing oxygen ambients*, 2003, Ph. D. Thesis, Research Centre Jülich, Jül-4070, Aachen.
41. Han, Y.H., Harmer, M.P., Hu, Y.H., and Smyth, D.M., *A^{2+}/Ti nonstoichiometry in alkaline earth titanates, $ATiO_3$*, in *Transport in Nonstoichiometric Compounds*, G. Simkovich and V.S. Stubican, Editors. 1985, Plenun Press: New York. p. 73.
42. Long, S.A. and Blumenthal, R.N., *Ti-rich nonstoichiometric $BaTiO_3$: II, Analysis of defect structure.* Journal of the American Ceramic Society, 1971a. **54**(11): p. 577.
43. Chan, N.H., Sharma, R.K., and Smyth, D.M., *Nonstoichiometry in undoped $BaTiO_3$.* Journal of the American Ceramic Society, 1981. **64**(9): p. 556.
44. Chan, N.H., Sharma, R.K., and Smyth, D.M., *Nonstoichiometry in acceptor-doped $BaTiO_3$.* Journal of the American Ceramic Society, 1982. **65**(3): p. 167.
45. Moos, R. and Hardtl, K.H., *Defect chemistry of donor-doped and undoped strontium titanate ceramics between 1000° and 1400°C.* Journal of the American Ceramic Society, 1997. **80**(10): p. 2549.

46. Sasaki, K. and Maier, J., *Low-temperature defect chemistry of oxides. I, General aspects and numerical calculations.* Journal of Applied Physics, 1999. **86**(10): p. 5422.

47. Long, S.A. and Blumenthal, R.N., *Ti-rich nonstoichiometric $BaTiO_3$: I, High-temperature electrical conductivity measurements.* Journal of the American Ceramic Society, 1971. **54**(10): p. 515.

48. Smyth, D.M., *Defect structure in perovskite titanates.* Current Opinion in Solid State & Materials Science, 1996. **1**(5): p. 692.

49. Meyer, R., Waser, R., Helmbold, J., and Borchardt, G., *Cationic surface segregation in donor-doped $SrTiO_3$ under oxidizing conditions.* Journal of Electroceramics, 2002. **9**(2): p. 103.

50. Akhtar, M.J., Akhtar, Z.U.N., Jackson, R.A., and Catlow, C.R.A., *Computer-simulation studies of strontium titanate.* Journal of the American Ceramic Society, 1995. **78**(2): p. 421.

51. Waser, R., *Bulk conductivity and defect chemistry of acceptor-doped strontium-titanate in the quenched state.* Journal of the American Ceramic Society, 1991. **74**(8): p. 1934.

52. Chan, N.H. and Smyth, D.M., *Defect chemistry of donor-doped $BaTiO_3$.* Journal of the American Ceramic Society, 1984. **67**(4): p. 285.

53. Chan, H.M., Harmer, M.P., and Smyth, D.M., *Compensating defects in highly donor-doped $BaTiO_3$.* Journal of the American Ceramic Society, 1986. **69**(6): p. 507.

54. Gomann, K., Borchardt, G., Gunhold, A., Maus-Friedrichs, W., and Baumann, H., *Ti diffusion in La-doped $SrTiO_3$ single crystals.* Physical Chemistry Chemical Physics, 2004. **6**(13): p. 3639.

55. Gomann, K., Bochardt, G., Schulz, M., Gomann, A., Maus-Friedrichs, W., Lesage, B., Kaitasov, O., Hoffman-Eifert, S., and Schneller, T., *Sr diffusion in undoped and La-doped $SrTiO_3$ single crystals under oxidizing conditions.* Physical Chemistry Chemical Physics, 2005. **7**(9): p. 2053.

56. Balachandran, U. and Eror, N.G., *Oxygen nonstoichiometry of tantalum-doped $SrTiO_3$.* Journal of the Less-Common Metals, 1982. **85**(1): p. 11.

57. Jeong, J.H., Park, M.G., and Han, Y.H., *Defect chemistry of Y doped $BaTiO_3$.* Journal of Electroceramics, 2004. **13**(1-3): p. 805.

58. Wang, D.Y. and Umeya, K., *Depletion-layer dielectric-properties of positive temperature-coefficient of resistance barium titanate.* Journal of the American Ceramic Society, 1990. **73**(6): p. 1574.

59. Chung, S.Y., Yoon, D.Y., and Kang, S.J.L., *Effects of donor concentration and oxygen partial pressure on interface morphology and grain growth behavior in $SrTiO_3$.* Acta Materialia, 2002. **50**(13): p. 3361.

60. Wilcox, N., Ravikumar, V., Rodrigues, R.P., Dravid, V.P., Vollmann, M., Waser, R., Soni, K.K., and Adriaens, A.G., *Investigation of grain boundary segregation in acceptor and donor-doped strontium titanate.* Solid State Ionics, 1995. **75**: p. 127.

61. Chiang, Y.M. and Takagi, T., *Grain boundary chemistry of barium titanate and strontium titanate: I, High-temperature equilibrium space-charge.* Journal of the American Ceramic Society, 1990. **73**(11): p. 3278.

62. Waser, R. and Hagenbeck, R., *Grain boundaries in dielectric and mixed conducting ceramics.* Acta Materialia, 2000. **48**(4): p. 797.

63. Johnson, K.D. and Dravid, V.P., *Grain boundary barrier breakdown in niobium donor doped strontium titanate using in situ electron holography.* Applied Physics Letters, 1999. **74**(4): p. 621.

64. Maier, J., *Defect chemistry in heterogeneous systems.* Solid State Ionics, 1995. **75**: p. 139.

65. Waser, R., *Electronic properties of grain boundaries in $SrTiO_3$ and $BaTiO_3$ ceramics.* Solid State Ionics, 1995. **75**: p. 89.

66. Pike, G.E., *Diffusion-limited quasi Fermi level near a semiconductor grain boundary.* Physical Review B, 1984. **30**(6): p. 3274.

67. Chiang, Y.M. and Takagi, T., *Grain boundary chemistry of barium titanate and strontium titanate: II, Origin of electrical barriers in positive-temperature-coefficient thermistors.* Journal of the American Ceramic Society, 1990. **73**(11): p. 3286.

68. Maier, J., *Ionic conduction in space charge regions.* Progress in Solid State Chemistry, 1995. **23**(3): p. 171.

69. Browning, N.D., Buban, J.P., Moltaji, H.O., Pennycook, S.J., Duscher, G., Johnson, K.D., Rodrigues, R.P. and Dravid, V.P., *The influence of atomic structure on the*

formation of electrical barriers at grain boundaries in $SrTiO_3$. Applied Physics Letters, 1999. **74**(18): p. 2638.

70. Klie, R.F. and Browning, N.D., *Atomic scale characterization of oxygen vacancy segregation at $SrTiO_3$ grain boundaries.* Applied Physics Letters, 2000. **77**(23): p. 3737.
71. Kim, M., Duscher, G., Browning, N.D., Sohlberg, K., Pantelides, S.T. and Pennycook, S.J., *Nonstoichiometry and the electrical activity of grain boundaries in $SrTiO_3$.* Physical Review Letters, 2001. **86**(18): p. 4056.
72. Szot, K. and Speier, W., *Surfaces of reduced and oxidized $SrTiO_3$ from atomic force microscopy.* Physical Review B, 1999. **60**(8): p. 5909.
73. Szot, K., Pawelczyk, M., Herion, J., Freiburg, C., Albers, J., Waser, R., Hulliger, J., Kwapulinski, J. and Dec, J., *Nature of the surface layer in ABO_3-type Perovskites at elevated temperatures.* Applied Physics a-Materials Science & Processing, 1996. **62**(4): p. 335.
74. Szot, K., Speier, W., Breuer, U., Meyer, R., Szade, J. and Waser, R., *Formation of micro-crystals on the (100) surface of $SrTiO_3$ at elevated temperatures.* Surface Science, 2000. **460**(1-3): p. 112.
75. Kazimirov, A., Goodner, D.M., Bedzyk, M.J., Bai, J. and Hubbard, C.R., *X-ray surface diffraction analysis of structural transformations on the (001) surface of oxidized $SrTiO_3$.* Surface Science, 2001. **492**(1-2): p. L711.
76. Szot, K., Speier, W., Herion, J. and Freiburg, C., *Restructuring of the surface region in $SrTiO_3$.* Applied Physics A-Materials Science & Processing, 1997. **64**(1): p. 55.
77. Sorensen, O.T., *Nonstoichiometric oxides*. 1981, Academic Press: New York. p. 198.
78. Kang, S.J.L., *Sintering*. 2005, Oxford: Elsevier Butterworth-Heinemann.
79. Shaw, N.J., *Densification and coarsening during solid-state sintering of ceramics: A review of the models. I Densification.* Powder Metallurgy International, 1989. **21**(3): p. 16.
80. Shaw, N.J., *Densification and coarsening during solid-state sintering of ceramics: A review of the models. II Grain-Growth.* Powder Metallurgy International, 1989. **21**(5): p. 31.

81. Shaw, N.J., *Densification and coarsening during solid-state sintering of ceramics: A review of the models. III Coarsening.* Powder Metallurgy International, 1989. **21**(6): p. 25.

82. Bae, C., Park, J.G., Kim, Y.H. and Jeon, H., *Abnormal grain growth of niobium-doped strontium titanate ceramics.* Journal of the American Ceramic Society, 1998. **81**(11): p. 3005.

83. Lin, M.H., Chou, J.F. and Lu, H.Y., *The rate-determining mechanism in the sintering of undoped nonstoichiometric barium titanate.* Journal of the European Ceramic Society, 2000. **20**(4): p. 517.

84. Hennings, D.F.K., Janssen, R. and Reynen, P.J.L., *Control of liquid-phase-enhanced discontinuous grain growth in barium titanate.* Journal of the American Ceramic Society, 1987. **70**(1): p. 23.

85. Choi, S.Y., Yoon, D.Y. and Kang, S.J.L., *Kinetic formation and thickening of intergranular amorphous films at grain boundaries in barium titanate.* Acta Materialia, 2004. **52**(12): p. 3721.

86. Lin, M.H. and Lu, H.Y., *Densification retardation in the sintering of La_2O_3-doped barium titanate ceramics.* Materials Science and Engineering A-Structural Materials Properties Microstructure and Processing, 2002. **323**(1-2): p. 167.

87. Ianculescu, A., Brăileanu, A. and Voicu, G., *Synthesis, microstructure and dielectric properties of antimony-doped strontium titanate ceramics.* Journal of the European Ceramic Society, 2007. **27**(2-3): p. 1123.

88. Chung, S.Y., Kang, S.J.L. and Dravid, V.P., *Effect of sintering atmosphere on grain boundary segregation and grain growth in niobium-doped $SrTiO_3$.* Journal of the American Ceramic Society, 2002. **85**(11): p. 2805.

89. Lee, B.K., Chung, S.Y. and Kang, S.J.L., *Grain boundary faceting and abnormal grain growth in $BaTiO_3$.* Acta Materialia, 2000. **48**(7): p. 1575.

90. Lee, B.K. and Kang, S.J.L., *Second-phase assisted formation of {111} twins in barium titanate.* Acta Materialia, 2001. **49**(8): p. 1373.

91. Chung, S.Y. and Kang, S.J.L., *Effect of dislocations on grain growth in strontium titanate.* Journal of the American Ceramic Society, 2000. **83**(11): p. 2828.

92. Chung, S.Y. and Kang, S.J.L., *Intergranular amorphous films and dislocations-promoted grain growth in $SrTiO_3$.* Acta Materialia, 2003. **51**(8): p. 2345.

93. Lin, T.F., Hu, C.T. and Lin, I.N., *Influence of stoichiometry on the microstructure and positive temperature-coefficient of resistivity of semiconducting barium titanate ceramics.* Journal of the American Ceramic Society, 1990. **73**(3): p. 531.

94. Rios, P.R., Yamamoto, T., Kondo, T. and Sakuma, T., *Abnormal grain growth kinetics $BaTiO_3$ with an excess TiO_2.* Acta Materialia, 1998. **46**(5): p. 1617.

95. Lee, S.B., Sigle, W. and Ruhle, M., *Investigation of grain boundaries in abnormal grain growth structure of TiO_2-excess $BaTiO_3$ by TEM and EELS analysis.* Acta Materialia, 2002. **50**(8): p. 2151.

96. Erkalfa, H., Yuksel, B. and Ozkan, T.O., *The effect of stoichiometry and the $TiCl_3$ addition on the microstructure of $BaTiO_3$.* Ceramics International, 2003. **29**(3): p. 317.

97. Hu, Y.H., Harmer, M.P. and Smyth, D.M., *Solubility of BaO in $BaTiO_3$.* Journal of the American Ceramic Society, 1985. **68**(7): p. 372.

98. Sharma, R.K., Chan, N.H. and Smyth, D.M., *Solubility of TiO_2 in $BaTiO_3$.* Journal of the American Ceramic Society, 1981. **64**(8): p. 448.

99. Rase, D.E. and Roy, R., *Phase equilibria in the system BaO-TiO_2.* Journal of the American Ceramic Society, 1955. **38**(3): p. 102.

100. Roth, R.S., Negas, T. and Cook, L.P., *Phase diagrams for ceramists - Vol. IV*. 1981. Columbus: The American Ceramic Society.

101. Demartin, M., Herard, C., Carry, C. and Lemaitre, J., *Dedensification and anomalous grain growth during sintering of undoped barium titanate.* Journal of the American Ceramic Society, 1997. **80**(5): p. 1079.

102. Jung, Y.I., Choi, S.Y. and Kang, S.J.L., *Effect of oxygen partial pressure on grain boundary structure and grain growth behavior in $BaTiO_3$.* Acta Materialia, 2006. **54**(10): p. 2849.

103. Lee, S.B., Yoon, D.Y. and Henry, M.F., *Abnormal grain growth and grain boundary faceting in a model Ni-base superalloy.* Acta Materialia, 2000. **48**(12): p. 3071.

104. Lee, S.B., Sigle, W., Kurtz, W. and Ruhle, M., *Temperature dependence of faceting in $\Sigma 5(310)[001]$ grain boundary of $SrTiO_3$.* Acta Materialia, 2003. **51**(4): p. 975.

105. Jung, Y.I., Choi, S.Y. and Kang, S.J.L., *Grain growth behavior during stepwise sintering of barium titanate in hydrogen gas and air.* Journal of the American Ceramic Society, 2003. **86**(12): p. 2228.

106. Choi, S.Y. and Kang, S.J.L., *Sintering kinetics by structural transition at grain boundaries in barium titanate.* Acta Materialia, 2004. **52**(10): p. 2937.

107. Lu, H.Y. and Lin, M.H., *Charge compensation mechanism in yttria-doped barium titanate.* Ceramics International, 2005. **31**(7): p. 989.

108. Lin, M.H. and Lu, H.Y., *Site-occupancy of yttrium as a dopant in BaO-excess $BaTiO_3$.* Materials Science and Engineering A, 2002. **335**(1-2): p. 101.

109. Drofenik, M., *Initial specific surface-area and grain growth in donor-doped barium titanate.* Journal of the American Ceramic Society, 1990. **73**(6): p. 1587.

110. Peng, C.J. and Lu, H.Y., *Compensation effect in semiconducting barium titanate.* Journal of the American Ceramic Society, 1988. **71**(1): p. C44.

111. Desu, S.B. and Payne, D.A., *Interfacial segregation in perovskites. 3 Microstructure and electrical properties.* Journal of the American Ceramic Society, 1990. **73**(11): p. 3407.

112. Chiang, Y.M. and Takagi, T., *Grain boundary chemistry of barium titanate and strontium titanate. 1 High temperature equilibrium space-charge.* Journal of the American Ceramic Society, 1990. **73**(11): p. 3278.

113. Hwang, J.H. and Han, Y.H., *Defect chemistry of Er-doped $BaTiO_3$.* Solid State Ionics, 2001. **140**(1-2): p. 181.

114. Witek, S., Smyth, D.M. and Pickup, H., *Variability of the Sr/Ti ratio in $SrTiO_3$.* Journal of the American Ceramic Society, 1984. **67**(5): p. 372.

115. Levin, E.M., Robbins, C.R. and McMurdie, H.F., *Phase diagrams for ceramists*. 1964. Columbus: The American Ceramic Society.

116. Levin, E.M., Robbins, C.R. and McMurdie, H.F., *Phase diagrams for ceramists - 1969 Suplement*. 1969. Columbus: The American Ceramic Society.

117. Bae, C., Park, J.G. and Kim, Y.H., *Effect of sintering condition on the morphology of abnormally grown grains in Nb-doped $SrTiO_3$ ceramics.* Journal of the Korean Physical Society, 1998. **32**: p. S361.

118. Chen, J.S., Young, R.J. and Wu, T.B., *Densification and microstructural development of $SrTiO_3$ sintered with V_2O_5.* Journal of the American Ceramic Society, 1987. **70**(10): p. C260.

119. You, I.K.,. Byun, J.D and Kim, Y.H., *The microstructure and electrical conductivity of WO_3-doped $SrTiO_3$ ceramics.* Solid State Ionics, 1996. **83**(1-2): p. 159.

120. Ianculescu, A., Braileanu, A., Zaharescu, M., Guillemet, S., Pasuk, I., Madarasz, J. and Pokol, G., *Formation and properties of some Nb-doped $SrTiO_3$-based solid solutions.* Journal of Thermal Analysis and Calorimetry, 2003. **72**(1): p. 173.

121. Todor, D.N., *Thermal analysis of minerals*. 1976. Kent: Abacus Press.

122. Pratten, N.A., *The precise measurement of the density of small samples.* Journal of Materials Science, 1981. **16**(7): p. 1737.

123. Li, Y.P., Liu, R.J., Chu, W.K. and Tate, T.J., *Observation of dynamic annealing effects in oxide single crystals after high-dose $^{18}O^+$ implantation at 500 ºC.* Physical Review B, 1998. **57**(10): p. 5668.

124. Han, H.P., Mantas, P.Q. and Senos, A.M.R., *Sintering kinetics of undoped and Mn-doped zinc oxide in the intermediate stage.* Journal of the American Ceramic Society, 2005. **88**(7): p. 1773.

125. Wang, J.D. and Raj, R., *Estimate of the activation energies for boundary diffusion from rate-controlled sintering of pure alumina and alumina doped with zirconia or titania.* Journal of the American Ceramic Society, 1990. **73**(5): p. 1172.

126. Raj, R. and Morgan, P.E.D., *Activation energies for densification, creep, and grain boundary sliding in nitrogen ceramics.* Journal of the American Ceramic Society, 1981. **64**(10): p. C143.

127. Young, W.S. and Cutler, I.B., *Initial sintering with constant rates of heating.* Journal of the American Ceramic Society, 1970. **53**(12): p. 659.

128. Senos, A.M.R., *Cinética de sinterização nos estágios de porosidade aberta do óxido de zinco*. 1993, Ph. D. Thesis, University of Aveiro, Aveiro.

129. Brook, R.J., *Controlled grain growth*, in *Treatise on materials science and technology*, F.F.Y. Wang, Editor. 1976, Academic Press, New York. p. 331.

130. Yang, C.F. and Lo, S.H., *Grain growth for CuO-BaO mixtures added $BaTi_{1-x}O_{3+2x}$ ceramics.* Materials Research Bulletin, 1997. **32**(12): p. 1713.

131. Han, J.P., Mantas, P.Q. and Senos, A.M.R., *Densification and grain growth of Al-doped ZnO.* Journal of Materials Research, 2001. **16**(2): p. 459.

132. Suzuki, T., Nishi, Y. and Fujimoto, M., *Defect structure in homoepitaxial non-stoichiometric strontium titanate thin films.* Philosophical Magazine A-Physics of Condensed Matter Structure Defects and Mechanical Properties, 2000. **80**(3): p. 621.

133. Genuist, C. and Haussonne, F.J.M., *Sintering of $BaTiO_3$ - dilatometric analysis of diffusion models and microstructure control.* Ceramics International, 1988. **14**(3): p. 169.

134. Freer, R., *Self-diffusion and impurity diffusion in oxides.* Journal of Materials Science, 1980. **15**(4): p. 803.

135. Dosdale, T. and Brook, R.J., *Comparison of diffusion data and of activation energies.* Journal of the American Ceramic Society, 1983. **66**(6): p. 392.

136. Dosdale, T. and Brook, R.J., *Cationic conduction and diffusion and compensation law.* Journal of Materials Science, 1978. **13**(1): p. 167.

137. Paladino, A.E., Rubin, L.G. and Waugh, J.S., *Oxygen ion diffusion in single crystal $SrTiO_3$.* Journal of Physics and Chemistry of Solids, 1965. **26**(2): p. 391.

138. Yamaji, A., *Oxygen-ion diffusion in single-crystal and polycrystalline $SrTiO_3$.* Journal of the American Ceramic Society, 1975. **58**(3-4): p. 152.

139. Turlier, P., Bussiere, P. and Prettre, M., *Application de la methode de Kryukov Et Zhukhovitskii a la mesure du coefficient dautodiffusion du strontium dans le metatitanate $SrTiO_3$.* Comptes Rendus Hebdomadaires Des Seances De L Academie Des Sciences, 1960. **250**(9): p. 1649.

140. Rhodes, W.H. and Kingery, W.D., *Dislocation dependence of cationic diffusion in $SrTiO_3$.* Journal of the American Ceramic Society, 1966. **49**(10): p. 521.